# CLOUD AND AEROSOL PROPERTIES MEASURED WITH A LIDAR IN THE HIGH ARCTIC AT EUREKA

by

Christopher Perro

Submitted in partial fulfillment of the requirements
for the degree of Master of Science

at

Dalhousie University
Halifax, Nova Scotia
November 2010

DALHOUSIE UNIVERSITY


DEPARTMENT OF PHYSICS AND ATMOSPHERIC SCIENCE


The undersigned hereby certify that they have read and recommend to the Faculty of Graduate Studies for acceptance a thesis entitled "CLOUD AND AEROSOL PROPERTIES MEASURED WITH A LIDAR IN THE HIGH ARCTIC AT EUREKA" by Christopher Perro in partial fulfillment of the requirements for the degree of Master of Science.


Dated: November 29, 2010


Supervisor: _____

Dr. Thomas Duck


Readers: _____

Dr. Glen Lesins


_____

Dr. Jeffrey Pierce

# DALHOUSIE UNIVERSITY

_____
Signature of Author

*For Danielle!*

# TABLE OF CONTENTS

# LIST OF TABLES

# LIST OF FIGURES

# ABSTRACT

The recently commissioned CANDAC Rayleigh−Mie−Raman Lidar (CRL) in Eureka, Nunavut, finished its first winter measurement campaign in 2010, during which over 900 hours of data was collected. A comparison of several inversion techniques are shown to determine which one is most appropriate for the CRL aerosol and cloud analyses. Results of a newly implemented automatic beam steering program are shown and discussed. Measurements of water vapour and aerosols showed a distinct layering effect in the troposphere. Back trajectories of these layers are compared to the CRL measurements to determine origins of these layers. Measurements of significant aerosol concentrations in the lower stratosphere were seen during the campaign, which were from the Sarychev eruption in June of 2009. The aerosol evolution over Eureka is shown by using different ground-based and satellite-based instruments. Calculations using multi-wavelength aerosol and cloud measurements are used to give insight on aerosol and cloud particle properties.

# LIST OF ABBREVIATIONS AND SYMBOLS USED

| | |
|---|---|
| $A$ | area of telescope |
| $C_{ratio}$ | colour ratio |
| $H_2O$ | water |
| $I$ | Intensity |
| $Mm$ | mega metre |
| $N$ | signal count |
| $N_2$ | nitrogen |
| $O$ | overlap function |
| $Q_{sc}$ | scattering efficiency |
| $R$ | backscatter ratio |
| $S$ | lidar ratio |
| $S_{aer}$ | lidar ratio |
| $S_{mol}$ | lidar ratio |
| $\textbf{ØPAL}$ | zero altitude PEARL auxilary laboratory |
| $\alpha$ | extinction coefficient |
| $\alpha_{\textbf{aer}}(z, \lambda_0)$ | extinction coefficient due to aerosols elastically scattered |
| $\alpha_{\textbf{aer}}(z, \lambda_R)$ | extinction coefficient due to aerosols Raman scattered |
| $\alpha_{\textbf{mol}}(z, \lambda_0)$ | extinction coefficient due to molecules elastically scattered |
| $\alpha_{tot}$ | total extinction coefficient |
| $\beta$ | volume backscatter cross section |
| $\beta_{\textbf{aer}}(z, \lambda_0)$ | volume backscatter cross section due to aerosols elastically scattered |
| $\beta_{\textbf{mol}}(z, \lambda_0)$ | volume backscatter cross section due to molecules elastically scattered |
| $\eta$ | lidar efficiency |
| $\lambda$ | wavelength |

| | |
|---|---|
| $\lambda_0$ | elastic wavelength |
| $\lambda_R$ | Raman wavelength |
| $\sigma_{abs}$ | absorption cross section |
| $\sigma_{sca}$ | scattering cross section |
| $\tau$ | optical depth |
| $c$ | speed of light |
| $k$ | Ångstrom exponent |
| $m$ | metre |
| $n$ | number density |
| $r$ | radius |
| $sr$ | steradian |
| $t$ | temporal pulse length |
| $w$ | water vapour mixing ratio |
| $y$ | normalized total extinction coefficient |
| $z$ | altitude |
| $z_c$ | calibration altitude |

| | |
|---|---|
| **CANDAC** | canadian network for the detection of atmospheric change |
| **IF** | interference filter |
| **LWP** | long wave pass |
| **ND** | neutral density filter |
| **PEARL** | polar environment atmospheric research laboratory |

# CHAPTER 1

# INTRODUCTION

There are many gaps in our understanding of Arctic atmospheric processes when compared to the rest of the planet since its harsh environment limits researchers accessibility. The radiative transfer processes in the Arctic are much different than at mid-latitudes due to several factors, one being the annual change from total daylight to total darkness. The very cold environment causes a shift in the wavelength band at which radiative cooling to space occurs from 10 $\mu$m to 20 $\mu$m. During the summer there is an unusually high albedo due to sea ice, and during the winter season there is a boundary layer temperature inversion. These processes have a large impact on the atmospheric conditions in this region which are still not fully understood, thus contributing greater uncertainties in the radiative transfer processes.

Climate has changed rapidly in the Arctic compared to the rest of the Earth. The temperatures in the Arctic have risen significantly over the past few decades and due to this increase there has been a decrease in ice cover during the Arctic summers (*Johannessen et al.*, 2004 and *Comiso et al.*, 2008 and *IPCC*, 2007). Anthropogenic pollution has been associated with the change in the radiative balance in the Arctic. These pollutants come from a wide variety of locations in the lower latitudes across the Northern Hemisphere. There is still a large uncertainty concerning the direct and indirect effects that aerosols have on radiative transfer process anywhere on the Earth (*IPCC*, 2007), therefore it is important to study the aerosols atmospheric effects to discover their impacts on the climate.

Besides anthropogenic pollution, there are natural sources for aerosols such as volcanic eruptions. Eruptions can send ash and gas to altitudes in the upper troposphere and lower stratosphere which can then spread across the globe. Volcanic plumes contain gases such as

$SO_2$, $CO_2$, $H_2O$ and HCl as their primary emissions (*Coffey*, 1996). Besides ash from volcanic plumes, aerosols can be created from conversion of $SO_2$ to sulphate aerosols ($SO_4^{2-}$) (*Coffey*, 1996). It is important to understand how all types of aerosol can affect the Arctic radiative balance.

The radiative balance in the Arctic is also largely affected by clouds. During the Winter months when there is no short wave radiation, clouds warm the Arctic by absorbing and emitting longwave radiation back to the surface (*Curry et al.*, 1996). Aerosols can affect cloud formation by changing the size of the cloud nuclei through the indirect effect which causes an increase in cloud albedo (*Twomey*, 1977) during the summer months. Another indirect effect of aerosols known as the second indirect effect causes cloud lifetimes to increases because of a decrease in the amount of precipitation (*Albrecht* (1989) and *Avey et al.* (2008)).

Due to the limited accessibility of the Arctic there is a historical lack of data to help in understanding the radiative processes that occur in Arctic locations. The Canadian Network for the Detection of Atmospheric Change (CANDAC) is an organization of different universities, Environment Canada, and international collaborators for the purpose of measuring Arctic atmospheric phenomena using a suite of instruments at Eureka, Nunavut(80°N, 85°W). One of the newly built instruments by the Atmospheric-Optics Laborartory (AO-LAB) is the CANDAC RMR Lidar at the Zero Altitude PEARL Auxilary Laboratory (ØPAL). This lidar is able to measure temperature, water vapour, aerosol, and depolarization at a range of altitudes continuously in time.

I was not personally involved in the construction of the CANDAC RMR Lidar but contributed to several other aspects of the system. Initial system characterization such as aperture stop, field stop, and focus stage positions were estimated by lidar measurements provided by retrievals using an automatic beam steering program which I designed. I was involved in the preparation of the lidar for its first measurement campaign which involved a trip to Eureka with Dr. Graeme Nott. I was one of the four operators during the winter 2010 measurement campaign for the CRL that was collecting 24 hours a day, five days a week. I also was in charge of particle analysis for clouds and aerosols by calculating multiple quantities such as the volume backscatter cross section, integrated backscatter cross section, lidar ratio, and colour ratio. These values were compared with other lidar results for the purpose of validating the CRL results. These analyses were used to track

stratospheric aerosols from the Sarychev eruption and to determine possible trajectories aerosol and water vapour underwent before arriving in Eureka. These will be discussed in this thesis.

Chapter 2 will give a background on scattering and transmission along with an introduction on what a lidar system is and how it works. There will then be a discussion of the different methods used to calculate measures of aerosols with lidar systems.

Chapter 3 will describe the instruments used in the analyses and how they operate. Results from a newly implemented automatic beam steering program will be shown along with data from the operations web site that keeps track of changes in the instruments used by the CANDAC Raman Lidar. There will also be a comparison of different lidar techniques to calculate the concentration of aerosols in the atmosphere to determine which technique is most advantageous to use.

Chapter 4 will describe the CANDAC Raman Lidar's first Winter measurement campaign. There will be an in depth description of several water vapour and aerosol measurements and a large focus on measurements of stratospheric aerosols which originate from the Sarychev eruption that occurred on June 12, 2009 (*Levin et al.*, 2010).

Chapter 5 will discuss aerosol and cloud properties in particular the colour ratio and lidar ratios. In this chapter several measurements of the lidar ratio and colour ratio are shown for clouds and aerosols along with comparisons of calculations done by different lidar systems at varying locations. Colour ratio measurements will also be converted to effective radii measurements giving insight to the size of cloud and aerosol particles in the Arctic. The last chapter will give a brief summary of the overall results of the winter campaign.

# CHAPTER 2

# BACKGROUND

A lidar (LIght Direction and Ranging), is an integration of different technologies to do remote sensing of particles in the atmosphere by combining radar and optical scattering principals (*Collis*, 1970). In this section, the theory on how a lidar operates is discussed along with some techniques on how to interpret the measurement retrievals for the detection of aerosols,clouds, and water vapour which will be discussed in later chapters. There are several different types of lidars that measure different quantities in a range of altitude regions. The focus for this thesis is tropospheric lidar measurements, particularly the Raman lidar.

## 2.1 Lidar Fundamentals

### 2.1.1 Scattering in the Atmosphere

There are three processes that affect the attenuation of radiation or photons in the atmosphere and they are scattering, absorption, and emission. Two of the most important processes for attenuation of photons, scattering and absorption, will be discussed in the following section.

Scattering of photons may be classified as elastic and inelastic. Elastic scattering occurs when there is no loss or gain of energy by the scatterer and the scattered photon preserves its original frequency and wavelength. Inelastic scattering refers to when the photon can lose or gain energy instead of conserving it during the scattering process. The photon scattered would have a wavelength and frequency shift due to the change in energy of the photon scattered. For the case of a lidar, the specific type of inelastic scattering that occurs is Raman scattering (*Wandinger*, 2005a).

Elastic scattering theory can categorized into three regimes, Rayleigh, Mie, and geometric optics scattering. The intensity and distribution of the scattered radiation by the three regimes of elastic scattering are dependent the wavelength of the incident radiation, size, refractive index, shape, and polarization of the scattering particle (*Liou*, 2002). To differentiate between the types of elastic scattering that can occur the size parameter, $x$ is evaluated (Equation 2.1),

$$x = \frac{2\pi r}{\lambda} \tag{2.1}$$

where $r$ is the radius of the particle, and $\lambda$ is the wavelength of the incident radiation. For Rayleigh scattering $x \ll 1$, Mie scattering occurs when $x \geq 1$ and geometric optics scattering occurs when $x \gg 1$ (*Liou*, 2002).
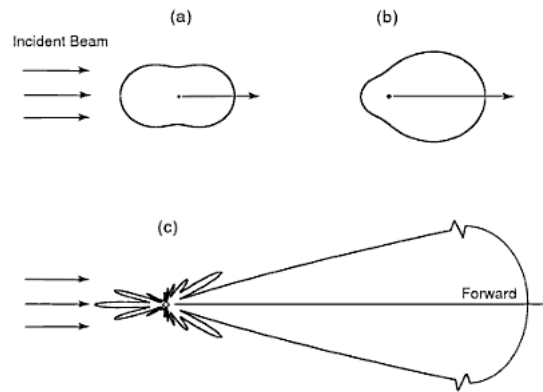


Figure 2.1: Phase Function diagram for three different size parameters where the solid line represents the intensity of scattering in that direction with respect to the particle which is represented by the dot in each diagram. a) Rayleigh regime b) Mie regime c) Mie and geometric optic regime (*Liou*, 2002)

The angular distribution of radiation from a scattering event is different for various values of the $x$, and is described by the phase function, $P(\cos\theta)$. For Rayleigh scattering, the intensity of scattered radiation is maximized at $0°$ and $180°$ from the angle of incidence and is minimized at $90°$ and $270°$ degrees from the angle of incidence. For Mie and geometric optics scattering, there is dominant scattering in the forward direction. The maximum and minimum intensity of scattered radiation with respect to the angle of incidence varies greatly due to changes in the properties of the particle. Figure 2.1 shows variations of phase function intensities for different size parameters. As the size parameter increases, the phase function becomes more complex (*Kovalev and Eichinger*, 2004).
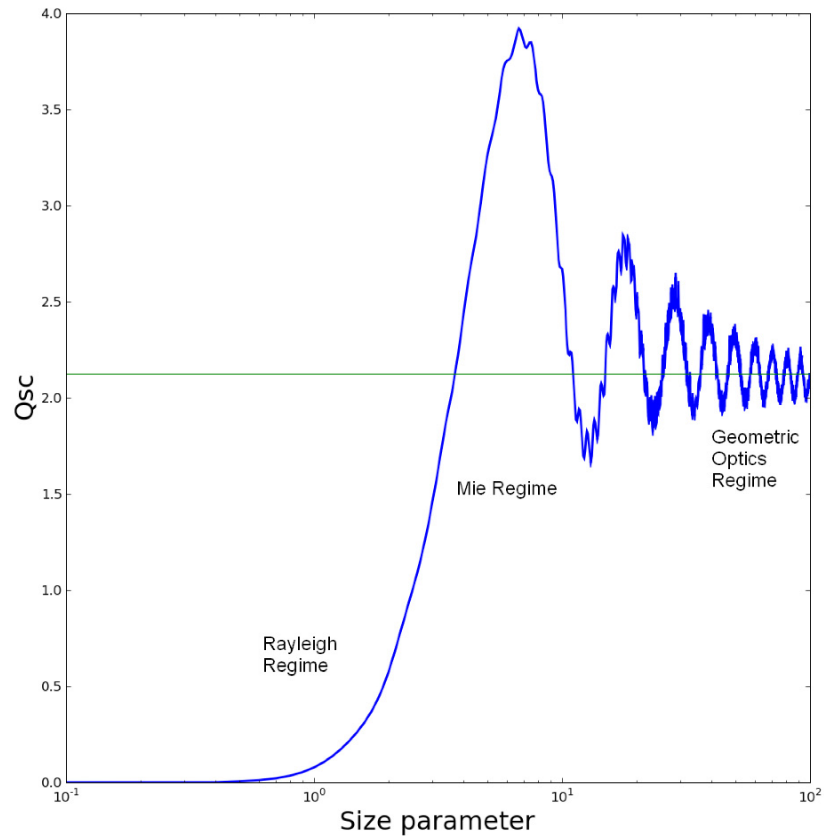
Figure 2.2: Scattering efficiency plot using Mie scattering code with varying size parameter (*Bohren and Huffman*, 1983). The green line represents the value the scattering efficiency converges for large size parameters.

The total scattering intensity of radiation is proportional to the scattering cross section, $\sigma_{sc}$, which is the amount of radiation removed by a single particle due to scattering, in units of area. Scattering efficiency is the scattering cross section divided by the geometric cross section of the particle or the efficiency of scattering for a single particle,

$$Q_{sc} = \frac{\sigma_{sc}}{\pi r^2}. \tag{2.2}$$

Figure 2.2 shows the changes in scattering efficiency, $Q_{sc}$ with variations in $x$ along with general areas on the scattering efficiency curve for the three elastic scattering regimes. At values of $x$ close to infinity, the scattering efficiency is approximately 2 for non-absorbing particles. The reason why the scattering cross section is double the physical area of the

particle is due to diffraction of light around the particle (*Liou*, 2002). The intensity of the scattering cross section is also dependent on which regime is being considered. The scattering cross section of scattered radiation for the Rayleigh regime is proportional to $\lambda^{-4}$. For Mie and geometric optics, the scattering cross section becomes more dependent on the size of the scatterer (*Liou*, 2002). For scattering in the atmosphere, molecules and nano-sized particles fit under the Rayleigh regime, aerosols and small cloud particles are in the Mie regime, and larger cloud particles are in the geometric optics regime for wavelengths in the visible to ultraviolet range.

There are two types of Raman scattering, stokes and anti-stokes. Stokes is when there is a decrease in the frequency of the scattered radiation and anti-stokes is when there is an increase in the frequency of the scattered radiation. Compared to the incident radiation, the frequency of the radiation scattered changes due to changes in the rotational and/or vibrational energy levels of the molecule the photon is scattering against (*Wandinger*, 2005b). The shift in the frequency of the radiation scattered is characteristic for the type of molecule that the photon is scattering with due to particular vibrational and rotational modes of each molecule. Figure 2.3 is a diagram of the scattering cross sections for various molecules undergoing Raman and elastic scattering which shows that the Raman scattering cross sections are orders of magnitude less than elastic scattering cross sections.
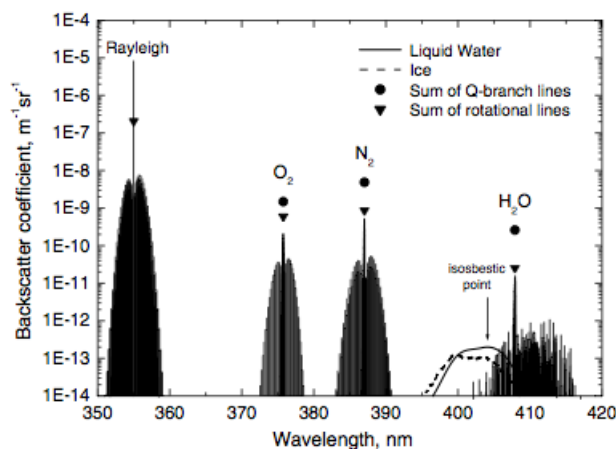


Figure 2.3: Elastic and Raman backscatter coefficient for the vibrational Stokes branch for nitrogen, oxygen, and different forms of water vapour for a laser wavelength of 355 nm. Backscatter coefficients also show rotational Raman scattering bands for each of the Elastic and vibrational Raman bands. This diagram compares the backscattering intensities for the different types of molecular scatterers (*Wandinger*, 2005a).

## 2.1.2   Transmission in the Atmosphere

To determine the intensity of radiation lost during an interaction with particles, the amount of transmitted radiation is determined. Transmission of radiation through a medium is due to a combination of scattering and absorption. Emission by the atmosphere can be neglected for the purposes of this thesis due to it being very small at lidar wavelengths. The intensity of radiation decreases as it goes through a medium, the intensity afterwards can be determined using the Beer-Bougher-Lambert law (*Liou*, 2002),

$$I_1 = I_0 e^{-\tau} = I_0 e^{-\int \alpha_{tot} dr}, \tag{2.3}$$

where $I_0$ and $I_1$ are the intensities before and after the radiation passes through the medium and $\alpha_{tot}$ is the extinction coefficient which has units of inverse length. The extinction coefficient is the fractional amount of radiation lost per unit length travelled through the medium and $r$ is the length of the medium. $\tau$ is the optical depth which is the integrated extinction in the length of the medium considered. $\alpha_{tot}$ is the sum of two processes, scattering and absorption of radiation, described by,

$$\alpha_{tot} = \sum_j n_j(z)[\sigma_{j,abs}(\lambda) + \sigma_{j,sca}(\lambda)], \tag{2.4}$$

where $\sigma_{j,abs}$ and $\sigma_{j,sca}$ are the absorption and scattering cross sections for each particle, *j*. $n_j(z)$ is the number density for particles at an altitude, *z*. The summation over j represents the sum of the different types of particles in the medium. The absorption cross section is the amount of radiation removed by a single particle due to absorption by said particle. These processes are directly related to how a lidar operates, as discussed later this chapter.

## 2.1.3   Lidar Technique

A lidar is an instrument that emits pulsed monochromatic radiation into the atmosphere and measures the backscattered radiation from different types of particles. The back scattered radiation from the particles is collected and counted using a receiving system. Figure 2.4 is a basic diagram of a lidar system which can be described as two general components, the transmitter and the receiver. The transmitter contains a pulsed monochromatic laser and a beam expander. The laser radiation is pulsed to achieve time of flight measurements. The

time of flight of the radiation allows the altitude at which the scattering process occurs to be determined. The beam expander in the transmitter section of a lidar reduces the divergence of the emitted radiation. For narrow field of view measurements the beam expansion needs to be small to compete with the telescope's field of view (*Wandinger*, 2005a).

The receiver is composed of a telescope and detector system. The telescope's primary mirror collects the backscattered radiation. The backscattered radiation is redirected towards the detector system where it will be distributed to different channels that are wavelength dependent. The different wavelengths of radiation are redirected by use of interference and band pass filters. At the end of each channel there is a photomultiplier followed by counting electronics.
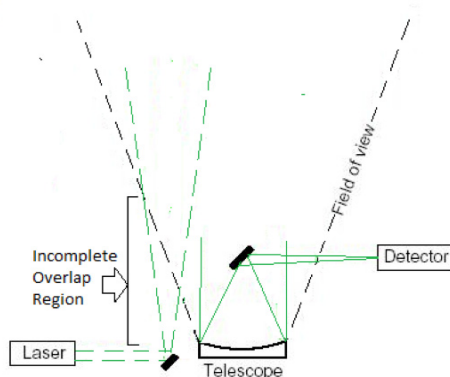
Figure 2.4: Bi-axial (laser and reciever parallel axes) lidar system with a diverging beam of radiation and field of view of the telescopes primary mirror. The radiation captured by the telescope is then redirected to the detector system

A common tropospheric lidar detects elastic and Raman scattering. A Raman lidar devotes channels to detecting the shifted wavelength/frequency for the particle. The most abundant particles that are measured by a Raman lidar in the atmosphere are nitrogen ($N_2$), oxygen ($O_2$), and water vapour ($H_2O$) (*Sakai et al.*, 2001). The scattering cross sections for other molecules are much smaller which makes it difficult for them to be measured by a lidar (*Wandinger*, 2005a).

## 2.1.4   Elastic and Raman Lidar Equations

The photon count rate measured at a particular altitude can be represented by a product of several variables in an equation known as the lidar equation, Equation 2.5,

$$N(z,\lambda) = N_0 \frac{ct}{2} A \eta \frac{O(z)}{z^2} \beta(z,\lambda) e^{-(\tau_u + \tau_b)} + N_{BG} \tag{2.5}$$

$N(z,\lambda)$ is the photon count rate at a particular altitude, $N_0$ is the average rate of photons emitted by the laser and $N_{BG}$ is the background photon count rate. The background photon count rate is due to photons collected by the telescope that originate as direct solar radiation or scattered solar radiation. The $\frac{ct}{2}$ represents the effective pulse length of the laser which can also be referred to as the vertical resolution of the system, where $c$ is the speed of light and $t$ is the temporal pulse length of the laser. The effective pulse length is half the actual pulse length ($ct$) because the radiation has to travel two ways when it is scattered into the telescope. $A$ and $\eta$ both are system constants where $A$ is the area of the telescope's primary mirror and $\eta$ is the efficiency of the lidar system. $O(z)$ is the overlap function of the lidar which is described in Section 2.1.4, $z$ is the altitude of the scattering event, and $\frac{A}{z^2}$ is proportional to the number of the photons collected by the telescope during the scattering event compared to the total scattering of photons during that event or the solid angle for the back scattered light (*Wandinger*, 2005b).

The volume backscatter cross section for the particle that is scattering the radiation is represented by $\beta(z,\lambda)$. Equation 2.6 represents the intensity of the backscattered light for all scatterers in the volume of the laser beam at a particular altitude range,

$$\beta(z,\lambda) = \sum_j n_j(z) \frac{d\sigma_{j,\text{sca}}}{d\Omega}(\lambda,\pi) \tag{2.6}$$

where $n_j(z)$ is the particle number density of the scatterer and $\frac{d\sigma_{j,\text{sca}}}{d\Omega}(\lambda,\pi)$ is the differential scattering cross section of a particular particle. The differential scattering cross section represents the amount of radiation scattered by a particular particle within the solid angle $d\Omega$ in a particular direction. The volume backscatter cross section is the sum of all the backscattered light from different particles at an altitude, $z$ for wavelength, $\lambda$. The last term in Equation 2.5, $e^{-(\tau_u + \tau_b)}$ is similar to the transmission term which is described in Section 2.1.2. In the case for a lidar, $\tau$ is expanded to $\tau_u$ and $\tau_b$ which represents the optical depth

up to the scattering event and the optical depth back of the source of the laser radiation. This term refers to the fraction of laser radiation that is attenuated by the atmosphere.

The form of the lidar equation shown above is a basic form. Depending on the type of scattering that occurs, the basic lidar equation can be expanded to account for a particular type of scattering. The two forms that will be discussed here are the elastic and Raman lidar scattering equations. The differences between the two equations are in the volume backscatter cross section and the transmission terms.

For elastic scattering the volume backscatter cross section is expanded into two terms,

$$\beta(z, \lambda) = \beta_{\text{mol}}(z, \lambda_0) + \beta_{\text{aer}}(z, \lambda_0) \tag{2.7}$$

where $\beta_{\text{mol}}(z, \lambda_0)$ is the volume backscatter cross section due to molecular scattering and $\beta_{\text{aer}}(z, \lambda_0)$ is the volume backscatter cross section due to aerosol scattering at the laser's wavelength, $\lambda_0$. The Raman lidar equation's volume backscatter cross section term is simpler because there is only scattering due to one type of molecule (*Wandinger*, 2005b),

$$\beta(z, \lambda) = \beta_{\text{mol}}(z, \lambda_0, \lambda_R) \tag{2.8}$$

where $\beta_{\text{mol}}(z, \lambda_0, \lambda_R)$ is the volume backscatter cross section due to molecular scattering at the Raman shifted wavelength, $\lambda_R$.

The other difference between the two sets of lidar equations is the transmission term. For the transmission of radiation through the atmosphere, the optical depth terms for elastic transmission takes the form:

$$\tau_u + \tau_b = 2 \int_0^z [\alpha_{\text{mol}}(r, \lambda_0) + \alpha_{\text{aer}}(r, \lambda_0)] dr \tag{2.9}$$

where $\alpha_{\text{mol}}(r, \lambda_0)$ is the extinction coefficient due to molecular absorption and scattering. $\alpha_{\text{aer}}(r, \lambda_0)$ is the extinction coefficient due to aerosol absorption and scattering. This integral is evaluated from the surface to altitude, $z$. The 2 represents the fact that the radiation is attenuated during the travel up to and back from the scattering event to the telescope so the extinction coefficients are doubled. The optical depth terms for Raman transmission is,

$$\tau_u + \tau_b = \int_0^z [\alpha_{\text{mol}}(r, \lambda_0) + \alpha_{\text{mol}}(r, \lambda_R) + \alpha_{\text{aer}}(r, \lambda_0) + \alpha_{\text{aer}}(r, \lambda_R)] dr \tag{2.10}$$

For Raman scattering there is extinction due to both molecules and aerosols but due to the wavelength shift there is also extinction at the two sets of wavelengths. The extinction coefficients at $\lambda_0$ are for travelling to the scattering event as represented by $\alpha_{\mathrm{mol}}(r,\lambda_0)$ and $\alpha_{\mathrm{aer}}(r,\lambda_0)$ and the extinction at $\lambda_{\mathrm{R}}$ is after the scattering event as represented by $\alpha_{\mathrm{mol}}(r,\lambda_{\mathrm{R}})$ and $\alpha_{\mathrm{aer}}(r,\lambda_{\mathrm{R}})$. Accounting for these differences in Equation 2.5, the lidar equations become, Equation 2.11 for elastic scattering and Equation 2.12 for Raman scattering (*Wandinger*, 2005b),

$$N_{\mathrm{elastic}}(z,\lambda_0) = N_0 \frac{ct}{2} A \eta \frac{O(z)}{z^2} [\beta_{\mathrm{mol}}(z,\lambda_0) + \beta_{\mathrm{aer}}(z,\lambda_0)] e^{-2\int_0^z [\alpha_{\mathrm{mol}}(r,\lambda_0) + \alpha_{\mathrm{aer}}(r,\lambda_0)]dr} \quad (2.11)$$

$$N_{\mathrm{Raman}}(z,\lambda_0,\lambda_{\mathrm{R}}) = N_0 \frac{ct}{2} A \eta \frac{O(z)}{z^2} \beta_{\mathrm{mol}}(z,\lambda_0,\lambda_{\mathrm{R}}) e^{-\int_0^z [\alpha_{\mathrm{mol}}(r,\lambda_0) + \alpha_{\mathrm{mol}}(r,\lambda_{\mathrm{R}}) + \alpha_{\mathrm{aer}}(r,\lambda_0) + \alpha_{\mathrm{aer}}(r,\lambda_{\mathrm{R}})]dr}$$
$$(2.12)$$

where $N_{\mathrm{elastic}}(z,\lambda_0)$ and $N_{\mathrm{Raman}}(z,\lambda_0,\lambda_{\mathrm{R}})$ are the photon count rates for elastic scattering and Raman scattering. Determination of $\alpha_{\mathrm{aer}}(z,\lambda_0)$ and $\beta_{\mathrm{aer}}(z,\lambda_0)$ are calculated by inverting the lidar equations as shown in Section 2.2.

## 2.1.5  *Incomplete Overlap and Differential Overlap Regions*

Most lidars have a range of altitudes near the surface known as the incomplete overlap region. It is where the laser's radiation is not completely within the field of view of the telescope as shown in Figure 2.3. The incomplete overlap region can extend up to a several kilometres above the lidar. The region exhibits a decrease in the number of photon counts received by a lidar's detector. If the incomplete overlap region did not exist, the lidar signal would follow a $\beta_{\mathrm{mol}}/z^2$ dependence assuming pure molecular scattering. Figure 2.5 shows that inside the incomplete overlap region, the number of photon counts decreases and the lidar signal deviates from the $\beta_{\mathrm{mol}}/z^2$ dependence (*Wandinger*, 2005b).

The overlap function, $O(z)$, is used to describe the incomplete overlap region of a lidar, and is defined to represent the fraction of the beam that is within the field of view of the telescope. When the beam is totally within the field of view, the overlap function would be equal to 1. If the beam was partially within the field of view it would be a value between 0 and 1. If the beam was not in the field of view the value is 0. Figure 2.5 has an example of an overlap function for a simulated lidar system.

The height of the incomplete overlap region is dependent on several factors of the lidar
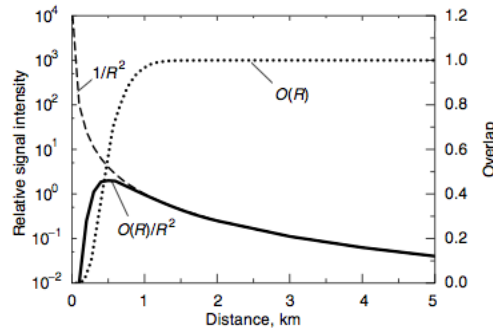
Figure 2.5: Comparison of a lidar signal profile with and without an incomplete overlap region. The solid line is the profile for the overlap function and the dashed line is a simulated profile for a lidar with no incomplete overlap region. The dotted profile is the calculated overlap function.

system, one is how the laser beam axis and telescope axis are aligned. There are two different types of arrangements between the laser beam axis and telescope axis, one is biaxial and the other is coaxial. Biaxial is when there are two separate axes for the laser beam and telescope field of view and coaxial is where the laser beam and telescope share the same axis (*McGill*, 2003).

Depending on the type of lidar, the incomplete overlap region can be caused by different variables of the system. Figure 2.4 shows how the height of the region for a biaxial lidar is caused by a combination of the field of view for the telescope, the divergence of the laser's radiation and the separation of the telescope and laser axes. For a coaxial lidar as in Figure 2.6, the height of the region depends on the size of the secondary mirror compared to the primary mirror and their locations with respect to each other.

The incomplete overlap region can encompass a large vertical extent of a tropospheric lidar's reach into the atmosphere. It is useful to create a correction to counteract the problem with this region. There have been theoretical calculations done trying to solve the overlap function, but it has not been successful due to the large number of uncertainties in any lidar (*Sasano et al.*, 1979). Instead, there are techniques to solve for the overlap function experimentally. One technique for determining the overlap function is to use a set of measurements in clear conditions as a baseline. Assuming there are no aerosols the ratio of the photon counts with a simulated molecular set of photon counts normalized between 0 and 1 can be used as an overlap function (*Sasano et al.*, 1979). Another technique is to have another telescope installed that has a wide field of view. Assuming the incomplete
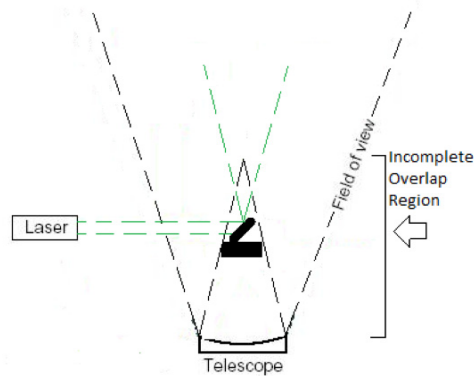
Figure 2.6: Coaxial lidar system with diverging laser beam (dashed green line) and field of view (diverging dashed black lines) of telescopes primary mirror. The black dashed conical lines represent the field of view of the telescope that is blocked by the secondary and output transmitter mirrors.

overlap region is much lower than the original telescopes overlap region, this could be used to evaluate the overlap function for the original telescopes field of view (*Bitar et al.*, 2010).

A technique that can be used for a Raman lidar system is one that takes the ratio of two signals, an elastic and Raman (*Wandinger and Ansmann*, 2002). Theoretically, the two signals overlap functions should be the same. Analysis of the photon counts could be analysed down to areas where the overlap function, $O(z) < 1$. The issue with this is that the overlap functions are not the same for the two different signals creating a differential overlap which is caused by different path lengths in the receiver. This occurs for backscattered light in the overlap region because it is incident on the telescope at larger angles compared to backscattered radiation at higher altitudes. The divergence of the light at the larger angles is much larger and if the detector is far than the collected light could miss the detector while a closer detector would still collect the light. Similar techniques can be done to correct the differential overlap as done for the incomplete overlap region.

## 2.1.6   Lidar Ratio

An important relation pertaining to the analysis of lidar measurements is the lidar ratio. The lidar ratio is the ratio of the extinction coefficient and the volume backscatter cross section for a type of particle,

$$S(z,\lambda) = \frac{\alpha(z,\lambda)}{\beta(z,\lambda)} \tag{2.13}$$

where $S(z,\lambda)$ is the lidar ratio. The lidar ratio is different for different types of particles. Pertaining to this thesis, the lidar ratio can is used for three types of particles; molecules, aerosols, and clouds.

For molecules, the lidar ratio ($S_{mol}$) is $\frac{8\pi}{3}$ sr assuming no absorption (*Cattrall et al.*, 2005). The molecular lidar ratio can be derived to a single value using Rayleigh scattering theory for molecules.

The aerosol lidar ratio ($S_{aer}$) depends on the size and shape of the particle, the wavelength scattered, chemical composition, and the refractive index of the aerosol being scattered. These quantities can change significantly for different types of aerosols varying the aerosol lidar ratio from 20 sr to 100 sr for visible wavelengths (*Ansmann and Muller*, 2005). Some representative aerosol lidar ratios are in Table 2.1.

| Particle Type | Lidar Ratio(sr) |
|---|---|
| Marine | $28 \pm 5$ |
| Desert Dust | $42 \pm 8$ |
| Biomass Burning | $60 \pm 8$ |
| Urban Pollution | $71 \pm 10$ |
| SE Asia | $58 \pm 10$ |

Table 2.1: Lidar ratios at 550 nm for different types of aerosols (*Cattrall et al.*, 2005)

For clouds, the lidar ratio varies for the same reasons as aerosols. The lidar ratio is usually smaller for clouds than aerosols and can vary between 6 sr and 60 sr for varying types and altitudes of clouds (*Giannakaki et al.*, 2007,*Reichardt*, 1998, and *Chen et al.*, 2002). One of the reasons why clouds have smaller lidar ratios than aerosols is because they are larger than aerosol particles. The lidar ratio can be helpful in solving the extinction coefficient and volume backscatter cross section in the elastic and Raman lidar equations. To get accurate values for the two variables it is important to have accurate lidar ratios. Due to the large variability of the lidar ratio in a measurement it can be difficult to choose a single value for the inversion techniques.

## 2.2  Inversion Techniques

The difficulty in calculating $\alpha_{\mathrm{aer}}(z, \lambda_0)$ and $\beta_{\mathrm{aer}}(z, \lambda_0)$ is that the lidar equation contains two unknowns. There are four techniques used for the inversion of the lidar equation to solve for the aerosol extinction coefficient and volume backscatter cross section($\alpha_{\mathrm{aer}}(z, \lambda_0)$ and $\beta_{\mathrm{aer}}(z, \lambda_0)$). The techniques are the Klett inversion, Raman Inversion, Coffin inversion, and ratio inversion. These variables are important in calculating values of optical depth and aerosol concentrations which have applications in pollution and climate research (*Ansmann et al.*, 1990). They can also be used for determination of particle physical quantities which is discussed in Chapter 5. Each inversion has its own advantages and disadvantages compared to the other inversions as discussed in the following section. Further testing of the techniques will be done in Chapter 3, particularly for the Coffin inversion which is a newly developed technique. The analyses will use measurements from the winter 2010 campaign (See Section 3.6).

### 2.2.1  Klett Inversion

One technique used to invert the elastic lidar equation is the Klett inversion. Using Equation 2.11 there are two unknowns, $\alpha_{\mathrm{aer}}(z, \lambda_0)$ and $\beta_{\mathrm{aer}}(z, \lambda_0)$, assuming the system constants and overlap functions are one. The molecular extinction coefficient, $\alpha_{\mathrm{mol}}(z, \lambda_0)$, and molecular volume backscatter cross section, $\beta_{\mathrm{mol}}(z, \lambda_0)$ terms are calculated from radiosonde data.

To make equation 2.11 solvable, the Klett inversion introduces another equation that also contains the two unknowns, this is the lidar ratio from Section 2.1.6. The lidar ratio is introduced to the elastic lidar equation in the form of the normalized total extinction coefficient (*Sasano et al.*, 1985),

$$y(z, \lambda_0) = \alpha_{\mathrm{aer}}(z, \lambda_0) + \frac{S_{\mathrm{aer}}}{S_{\mathrm{mol}}} \alpha_{\mathrm{mol}}(z, \lambda_0), \tag{2.14}$$

in the Klett inversion, the normalized total extinction coefficient is the variable solved from which $\alpha_{\mathrm{aer}}(z, \lambda_0)$ can be calculated. $S_{\mathrm{aer}}$ is assumed a constant in the Klett inversion and is estimated for the calculation of $y(z, \lambda_0)$. The normalized extinction coefficient is substituted in the elastic lidar equation giving a Bernoulli differential equation which can be solved to

give (*Sasano et al.*, 1985),

$$y(z,\lambda_0) = \frac{S_{\mathrm{aer}}(z,\lambda_0)N(z,\lambda_0)z^2 e^{-2\int_{z_c}^{z}[\frac{S_{\mathrm{aer}}(r,\lambda_0)}{S_{\mathrm{mol}}}-1]\alpha_{\mathrm{mol}}dr}}{\frac{S_{\mathrm{aer}}N_c(z_c,\lambda_0)z_c^2}{y_c(z_c,\lambda_0)} - 2\int_{z_c}^{z} S_{\mathrm{aer}}(r,\lambda_0)N(r,\lambda_0)r^2 e^{-2\int_{z_c}^{r}(\frac{S_{\mathrm{aer}}(r',\lambda_0)}{S_{\mathrm{mol}}}-1)\alpha_{\mathrm{mol}}dr'}\,dr}, \quad (2.15)$$

where $y_c(z_c,\lambda_0)$ is the normalized extinction coefficient in the calibration region, $z_c$. The calibration region is a range of altitudes that is considered clear air, or in other words, a range of altitudes with no aerosols or clouds present. This can usually be assumed for high tropospheric and low stratospheric altitude ranges. The calibration region acts as a boundary condition for the Klett inversion where $\alpha_{\mathrm{aer}}(z,\lambda_0)$ is set to zero. Starting at the calibration region a recursive process continues to calculate $y(z,\lambda_0)$ for the next range bin using the previously calculated normalized total extinction coefficient ($y(z_c,\lambda_0)$) as the calibrated region. The Klett inversion can operate in the forward direction ($z > z_c$) or the backward direction ($z < z_c$). The backward inversion is more stable than the forward inversion, therefore in most cases it is best to have the calibration region at high altitudes to operate the inversion in the backwards direction (*Klett*, 1981).



Figure 2.7: Comparison of $\alpha_{\mathrm{aer}}(z,\lambda_0)$ and $\beta_{\mathrm{aer}}(z,\lambda_0)$ calculations for a simulated aerosol layer from 2-4 km with a 532 nm laser for three different aerosol lidar ratios using the Klett inversion. The modelled atmosphere has an aerosol lidar ratio of 70 sr with comparisons of assumed lidar ratios for 40, 70, and 100 sr. The comparison shows how an incorrect lidar ratio assumed for the Klett inversion can change the values of both $\alpha_{\mathrm{aer}}(z,\lambda_0)$ and $\beta_{\mathrm{aer}}(z,\lambda_0)$.

The advantage to using the Klett inversion over the other techniques is that there is less noise attributed to the signal used. The other inversions use a Raman signal or both

an elastic and Raman signal which will increase the signal noise significantly because the Raman signals have a lower scattering cross section than the elastic signals. There are also a few disadvantages to using this technique. One issue is with the stability of the recursive relationship when operating in the forward direction. Another issue is if an incorrect aerosol lidar ratio is assumed $\alpha_{aer}(z, \lambda_0)$ will be either underestimated or overestimated. Another related problem is that the technique assumes a constant aerosol lidar ratio. The lidar ratio can vary significantly throughout a measurement due to the changes in the particle properties as mentioned in Section 2.1.5. This cannot be corrected for with the use of a constant lidar ratio. A method used in the following analyses is to have a threshold value for the purpose of switching lidar ratios depending on the particle measured, such as aerosols or clouds. This partially corrects the measurement, but having a constant lidar ratio for all aerosols or all clouds is still not optimal. The error due to an incorrect lidar ratio can be partially corrected by calculating $\beta_{aer}(z, \lambda_0)$ instead as shown in Figure 2.7. The estimate for the aerosol layer is improved in the figure but there are still errors in $\beta_{aer}(z, \lambda_0)$ in the layer and below the simulated layer. The reason for why $\beta_{aer}(z, \lambda_0)$ produces a more accurate value than $\alpha_{aer}(z, \lambda_0)$ is because the lidar is measuring the backscatter, not the extinction.

## 2.2.2 Raman Inversion

A method for inversion of the Raman lidar equation is the Raman inversion. The difference in this technique compared to the Klett inversion is that this method uses a Raman signal instead of an elastic signal. The reason to use the Raman signal instead is due to the fact that there is no $\beta_{aer}(z, \lambda_0)$ term in the Raman lidar equation so the lidar ratio will not have to be introduced to this method. There is still one issue with the Raman inversion and that is because there are two different aerosol extinction terms, $\alpha_{aer}(z, \lambda_0)$ and $\alpha_{aer}(z, \lambda_R)$, due to the frequency shift during the scattering process. $\alpha_{aer}(z, \lambda_R)$ is removed using a relation for the aerosol extinction coefficients and wavelengths of the aerosol extinction coefficients (*Ansmann et al.*, 1990) as in Equation 2.16,

$$\frac{\alpha_{aer}(z, \lambda_0)}{\alpha_{aer}(z, \lambda_R)} = \left[ \frac{\lambda_R}{\lambda_0} \right]^k \tag{2.16}$$

where $k$ is the Ångstrom exponent. The Ångstrom exponent is a variable that describes the wavelength dependence of extinction and it varies depending on the type of particle that is causing the extinction. For aerosols an Ångstrom exponent between 1 and 2 is suitable (*Ansmann and Muller*, 2005) and clouds are approximately 0 due to the large size of the particles. Rearranging the Raman lidar equation for $\alpha_{\text{aer}}(z, \lambda_0)$ and substituting equation 2.16 to replace the $\alpha_{\text{aer}}(z, \lambda_R)$ term gives,

$$\alpha_{\text{aer}}(z, \lambda_0) = \frac{\frac{d}{dz}\left[\ln\frac{n_{\text{R,mol}}(z)}{z^2 N(z, \lambda_0, \lambda_R)}\right] - \alpha_{\text{mol}}(z, \lambda_0) - \alpha_{\text{mol}}(z, \lambda_R)}{1 + \left[\frac{\lambda_0}{\lambda_R}\right]^k}. \tag{2.17}$$

An advantage to using this inversion method is that there is no calibration region or integrated calculations as in the Klett inversion. Also, unlike the Klett inversion, there are no substantial assumptions in the technique. The only assumption is the Ångstrom, $k$. Similar to the Klett inversion though, constant $k$ for clouds and aerosols is chosen. Large variations in $k$ affect $\alpha_{\text{aer}}(z, \lambda_0)$ insignificantly, if $k$ is 0.5 away from the real value of the Ångstrom exponent, errors of approximately 5% (*Wandinger*, 2005a) are produced.

The disadvantage to the Raman inversion is that the scattering cross section for Raman scattering is much smaller than it is for elastic scattering which produces lower photon count rates for the Raman channels. The Klett inversion does not suffer from this because the elastic scattering cross section is several orders of magnitude higher than the Raman scattering cross section for molecules as shown in Figure 2.4. Another disadvantage is that the Raman inversion usually needs to operate with larger vertical integrations as compared to the Klett inversion to evaluate proper values of $\alpha_{\text{aer}}(z, \lambda_0)$. The reason for this is due to the derivative in the inversion. If the Raman signal is noisy or has low signal, the derivative will not be accurate creating variability in the Raman inversion calculation. The problem with averaging is that smaller details in the data set will be averaged together which will therefore not be seen.

### 2.2.3 Coffin Inversion

Another method to calculate the aerosol extinction coefficient is the Coffin inversion (*Coffin*, 2006). This inversion employs both the Raman and elastic signals. The elastic and

Raman scattering count rates are divided for the purpose of getting rid of the overlap function terms in the lidar equations. The two signals originate from the same laser and detector so the overlap functions should be the same theoretically but not in practice as discussed in Section 2.1.4. The solution derived for the Coffin inversion is similar to the Klett inversion except for the inclusion of a Raman signal with the elastic signal.

The Coffin inversion also suffers from the same fault as the Klett inversion which is the fact that there are more unknowns than equations. The lidar ratios are introduced into the ratio as it was introduced into the Klett inversion using the normalized total extinction coefficient, Equation 2.14. Also, Equation 2.16 is introduced to reduce the number of aerosol extinction coefficient terms due to the extra terms introduced from the Raman lidar equation. This introduces $k$ as another constant value for the input to the Coffin inversion.

After the introduction of Equation 2.14 and Equation 2.16 into the ratio of the two lidar equations, the resulting equation takes the form of a Bernoulli differential equation as in the Klett inversion which can then be solved to give (*Coffin*, 2006),

$$
\begin{aligned}
y(z,\lambda_0,\lambda_R) &= \frac{B(z,\lambda_0,\lambda_R)}{\frac{\beta_{\text{mol}}(z_c,\lambda_R)S_{\text{aer}}(z,\lambda_0)N_{\text{ratio}}}{y(z_c,\lambda_0,\lambda_R)} - \left[1 - \left(\frac{\lambda_0}{\lambda_R}\right)^k\right]\int_{z_c}^z B(r,\lambda_0,\lambda_R)\mathrm{d}r} \\
B(z,\lambda_0,\lambda_R) &= \beta_{\text{mol}}(z,\lambda_R)S_{\text{aer}}(z,\lambda_0)N_{\text{ratio}}e^{A(z,\lambda_0,\lambda_R)} \\
A(z,\lambda_0,\lambda_R) &= -\int_{z_c}^z \alpha_{\text{mol}}(r,\lambda_0)\left[\frac{S_{\text{aer}}(r,\lambda_0)}{S_{\text{mol}}}\left(1 - \left(\frac{\lambda_0}{\lambda_R}\right)^k\right) - \left(1 - \left(\frac{\lambda_0}{\lambda_R}\right)^k\right)\right]\mathrm{d}r
\end{aligned}
$$

$$(2.18)$$

where $N_{\text{ratio}}$ is the ratio of $N_{\text{elastic}}(z,\lambda_0)$ and $N_{\text{Raman}}(z,\lambda_0,\lambda_R)$. As with the Klett inversion, the values are evaluated recursively using the calibration region, $z_c$.

An advantage of using the Coffin inversion is that the lidar ratio has a smaller effect on the inaccuracy of the calculated profiles of $\alpha_{\text{aer}}(z,\lambda_0)$ or $\beta_{\text{aer}}(z,\lambda_0)$. In the Klett inversion, the extinction of the beam had to be taken into account during the calculations of the aerosol and molecular extinction coefficients but if the aerosol lidar ratio was inaccurate, the extinction below the aerosol region would be incorrect as in Figure 2.7. For the Coffin inversion this is not a problem because it is absolutely referenced against the molecular signal. Figure 2.8 shows how large variations in the aerosol lidar ratio mildly affect the extinction below and in the aerosol layer for $\beta_{\text{aer}}(z,\lambda_0)$ calculations. Figure 2.9 shows how $k$ also has a small effect on $\alpha_{\text{aer}}(z,\lambda_0)$ or $\beta_{\text{aer}}(z,\lambda_0)$ calculations as it did in the Raman
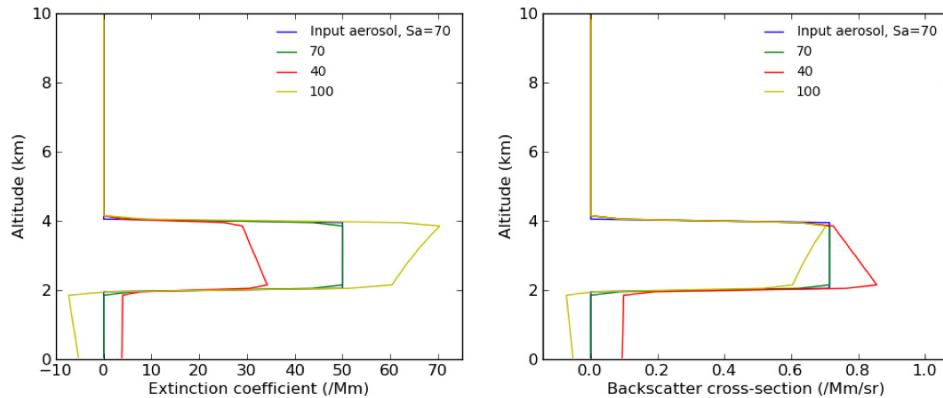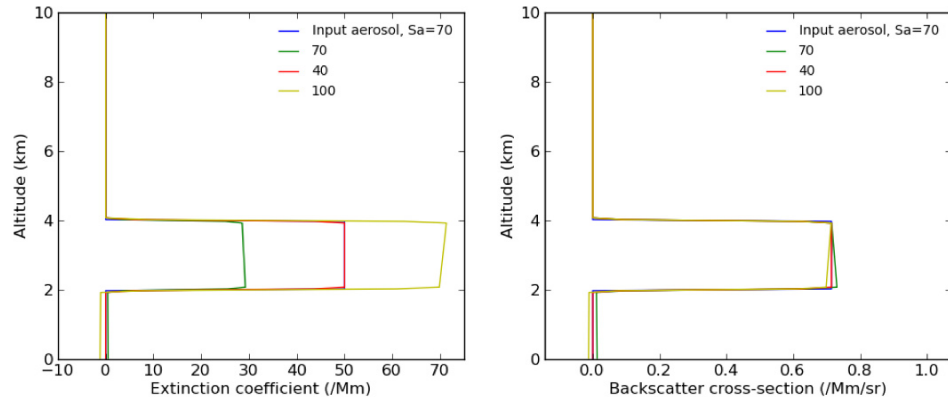
Figure 2.8: Comparison of $\alpha_{\text{aer}}(z, \lambda_0)$ and $\beta_{\text{aer}}(z, \lambda_0)$ calculations for a simulated aerosol layer from 2-4 km with a 532 nm laser and 607 nm Raman scattering for three different aerosol lidar ratios using the Coffin inversion

inversion. The disadvantage to the Coffin inversion is that there is a significant amount of noise introduced when the Raman signal is combined with elastic signal.
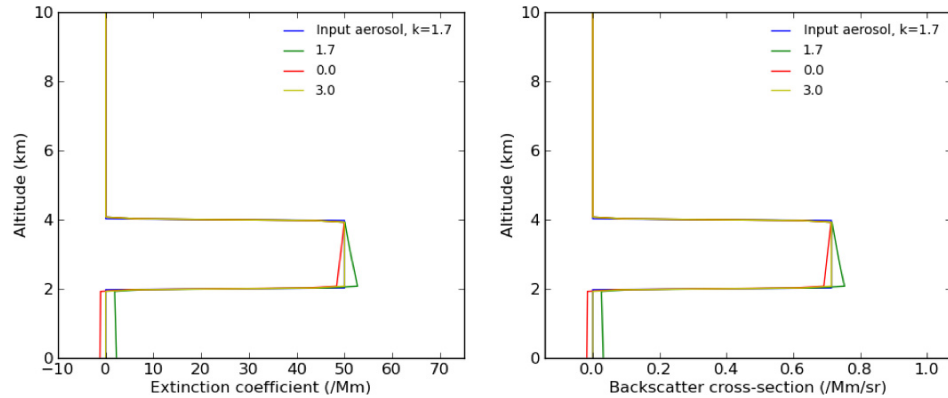


Figure 2.9: Comparison of $\alpha_{\text{aer}}(z, \lambda_0)$ and $\beta_{\text{aer}}(z, \lambda_0)$ for a simulated aerosol layer from 2-4 km with a 532 nm laser and 607 nm Raman scattering for three different values of $k$ in the Coffin inversion.

### 2.2.4   Ratio Inversion

One more technique used that is similar to the Coffin inversion is the ratio inversion. This technique produces a similar result as the Coffin inversion except it does not account for differential extinction due to the different wavelengths of the elastic and Raman signals. Similar to the Coffin inversion, the ratio inversion employs the use of the elastic and Raman

scattering wavelengths by using the ratio of the two signals. The ratio inversion calculates the $\beta_{\text{aer}}(z, \lambda_0)$ by first determining the backscatter ratio of the two signals. The backscatter ratio is defined as total volume backscatter cross section divided by the molecular volume backscatter cross section as in *Whiteman*, 2003 ,

$$R(z, \lambda_0) = \frac{\beta_{\text{tot}}(z, \lambda_0)}{\beta_{\text{mol}}(z, \lambda_0)} = \frac{\beta_{\text{aer}}(z, \lambda_0) + \beta_{\text{mol}}(z, \lambda_0)}{\beta_{\text{mol}}(z, \lambda_0)} \tag{2.19}$$

where $R(z, \lambda_0)$ is the backscatter ratio at altitude $z$ and at $\lambda_0$. To calculate the backscatter ratio from the set of lidar signals, the ratio of the elastic signal and Raman signal at a particular height are taken along with the inverse ratio of the elastic and Raman signals at a calibration region where $\beta_{\text{aer}}(z_c, \lambda)$ is assumed to be zero. The calibration region accounts for different scattering efficiencies of the elastic and Raman signals retrieved. Each elastic and Raman signal is corrected for differential molecular scattering by producing molecular signals from density profiles provided by radiosonde measurements. The molecular terms are used to divide the two sets of lidar signals which will correct for the differential molecular extinction. Equation 2.20 is the form of the backscatter ratio used with the ratio inversion.

$$R(z, \lambda_0) = \left( \frac{N(z, \lambda_0)N(z_0, \lambda_R)}{N(z_0, \lambda_0)N(z, \lambda_R)} \right) \left( \frac{N_{\text{mol}}(z_0, \lambda_0)N_{\text{mol}}(z, \lambda_R)}{N_{\text{mol}}(z, \lambda_0)N_{\text{mol}}(z_0, \lambda_R)} \right) \tag{2.20}$$

The $N_{\text{mol}}$ terms are the expected molecular signals produced from radiosonde measurements for elastic and Raman scattering wavelengths. Equation 2.20 is only possible for when there is an assumption of no differential aerosol or cloud extinction since only the molecular differential correction is corrected. In most cases it can be assumed that the differential aerosol or cloud extinction is negligible for low optical depths (*Whiteman*, 2003). Using the calculated backscatter ratio from Equation 2.20, the backscatter cross section can be calculated using Equation 2.19. Rearranging Equation 2.19 for $\beta_{\text{aer}}(z, \lambda_0)$ gives,

$$\beta_{\text{aer}}(z, \lambda_0) = (R(z, \lambda_0) - 1)\beta_{\text{mol}}(z, \lambda_0). \tag{2.21}$$

The advantage to using the Raman inversion over the other techniques is that there are no estimated parameters. Also, similarly to the Coffin inversion, the technique is absolutely referenced to a molecular signal. The disadvantage of this techniques is the error introduced by not accounting for differential aerosol or cloud extinction but it is assumed to be negligible for most measurements. For the measurements where differential aerosol or

cloud extinction is not negligible the Coffin inversion may be superior to the ratio inversion in the sense that it can correct for it by varying $k$. Also, another disadvantage would be the inclusion of noise from the inclusion of two signals.

## 2.3   Water Vapour Technique

Raman lidars can also measure the vertical structure of water vapour by calculating the water vapour mixing ratio,

$$w = \frac{M_{H_2O}}{M_{dry}} \frac{n_{H_2O}}{n_{dry}} \tag{2.22}$$

where $M_{H_2O}$ and $M_{dry}$ are the molecular weights of water vapour and dry air. $n_{H_2O}$ and $n_{dry}$ are the number densities of water vapour and nitrogen in the atmosphere, and $w$ is the water vapour mixing ratio in units of g/kg. To retrieve the water vapour mixing ratio, the ratio of a Raman-shifted water vapour signal and a Raman-shifted nitrogen signal are taken (See Section 2.1.1). The nitrogen signal acts as a proxy for dry air since the atmosphere is comprised mostly of nitrogen. Using the ratio of two Raman lidar equations with the wavelengths both being Raman-shifted gives (*Whiteman*, 2003),

$$\frac{N_{H_2O}(z, \lambda_0, \lambda_{H_2O})}{N_{N_2}(z, \lambda_0, \lambda_{N_2})} = \frac{n_{H_2O}(z)}{n_{N_2}(z)} \frac{\frac{d\sigma_{sca}}{d\Omega}(\lambda_{H_2O}, \pi)}{\frac{d\sigma_{sca}}{d\Omega}(\lambda_{N_2}, \pi)} \frac{\eta_{H_2O}}{\eta_{N_2}} T(z, \lambda_{N_2}, \lambda_{H_2O})$$

$$T(z, \lambda_{N_2}, \lambda_{H_2O}) = e^{-\int_0^z [\alpha_{mol}(r, \lambda_{H_2O}) - \alpha_{mol}(r, \lambda_{N_2}) + \alpha_{aer}(r, \lambda_{H_2O}) - \alpha_{aer}(r, \lambda_{N_2})] dr} \tag{2.23}$$

where $\frac{d\sigma_{sca}}{d\Omega}(\lambda_{N_2}, \pi)$ and $\frac{d\sigma_{sca}}{d\Omega}(\lambda_{H_2O}, \pi)$ are differential scattering cross sections for due to water vapour and nitrogen. $\eta_{H_2O}$ and $\eta_{N_2}$ are the lidar efficiencies for each channel and $\alpha_{mol/aer}(r, \lambda_{N_2/H_2O})$ are extinction terms due to aerosols or molecules after the Raman scattering event. Other terms from the Raman lidar equation cancelled out while the ratio of the two equations were taken.

Combining the previous two equations will give a relation for the water vapour mixing ratio, $w$, and the Raman lidar signals, $N_{H_2O/N_2}(z, \lambda_0, \lambda_{H_2O/N_2})$. $n_{dry}$ has to be converted to $n_{N_2}$ before the two equations can be combined and this is done by assuming $n_{N_2}$ is 78% of

$n_{\text{dry}}$. Equation 2.23 is rearranged for $\frac{n_{H_2O}(z)}{n_{N_2}(z)}$ and inserted into Equation 2.22,

$$w = k\frac{N_{H_2O}(z,\lambda_0,\lambda_{H_2O})}{N_{N_2}(z,\lambda_0,\lambda_{N_2})}e^{-\int_0^z[\alpha_{\text{mol}}(r,\lambda_{H_2O})-\alpha_{\text{mol}}(r,\lambda_{N_2})+\alpha_{\text{aer}}(r,\lambda_{H_2O})-\alpha_{\text{aer}}(r,\lambda_{N_2})]dr}$$

$$k = 0.78\frac{M_{H_2O}}{M_{\text{dry}}}\frac{\frac{d\sigma_{\text{sca}}}{d\Omega}(\lambda_{H_2O},\pi)}{\frac{d\sigma_{\text{sca}}}{d\Omega}(\lambda_{N_2},\pi)}\frac{\eta_{H_2O}}{\eta_{N_2}} \qquad (2.24)$$

where k is the calibration constant that relates $w$ to the lidar signals and is a combination of all terms that are constant with altitude and time. The 0.78 represents the conversion from $n_{\text{dry}}$ to $n_{N_2}$. $k$ is determined by comparing radiosonde measurements with the lidar signals. $k$ can vary significantly depending on the efficiencies of the measured signals. The molecular extinction terms are determined using radiosonde measurements as well and the aerosol extinction terms are considered negligible in most cases. Other operators involved in the campaign were in charge of the analysis for water vapour measurements and were provided by them for Section 4.2.

# Chapter 3

# Instrumentation and Operations

In the following chapters the CANDAC Rayleigh-Mie-Raman Lidar, Arctic High Spectral Resolution Lidar, Millimetre Cloud Radar are used for ground based measurements along with the OMI and CALIOP satellite instruments which are described in the following sections. In the following chapter there is a description of technical and software improvements made to the CRL. Also, a comparison of the inversion techniques discussed in Section 2.2 is undertaken to determine the appropriate inversion technique used for the aerosol analysis by the CRL.

## 3.1  Ground-based Instruments

### 3.1.1  CANDAC Rayleigh-Mie-Raman Lidar

The CANDAC Rayleigh-Mie-Raman Lidar (CRL) is a lidar system that collects and measures elastic and Raman scattering (See Section 2.1.1) in eight different wavelength dependent channels. Figure 3.1 shows a schematic of the CRL's transmitter and receiver.

The transmitter for the CRL consists of two ND:YAG lasers that operate with a repetition rate of 10 Hz. One lasers transmits at a wavelength of 532 nm which is frequency-doubled from 1064 nm and the other transmits at 355 nm which is frequency-tripled from 1064 nm. The 532 nm laser also has an injection seeder used for stabilizing the frequency of the radiation for the purpose of atmospheric temperature measurements. Both lasers are approximately co-aligned and exit the container coaxially (See Section 2.1.5). There are two steering mirrors that align each laser with the telescopes field of view as labelled in Figure 3.1b as A (532 nm laser) and B (355 nm laser). Each steering mirror position can be adjusted on two axes. Mirror B is used to steer both lasers but the lasers are not perfectly
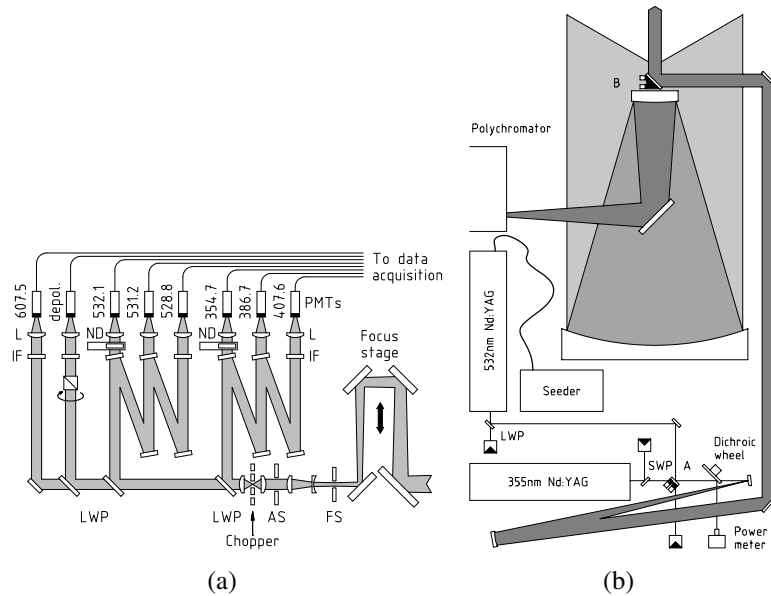
Figure 3.1: A schematic diagram of the CRL's a) polychromator and b) transmitter. The polychromator consists of a Delay Stage, Field Stop (FS), Aperture Stop (AS), Long wave passes (LWP), Neutral Density filters (ND), and Interference Filters (IF) (*Nott et al.*, 2010).

co-aligned so mirror A is used to adjust the 532 nm laser. If the laser and telescope axes are misaligned errors in the retrieval and loss of signal counts can occur.

The receiver of the CRL has a telescope with a 1 metre primary mirror that collects backscattered radiation to the polychromator. The field stop, FS, adjusts the field of view for the telescope between 0.3 mrad and 2 mrad for the purpose of reducing background counts and decreasing the height of the incomplete overlap region (See Section 2.1). The aperture stop, AS, controls the overall amount of radiation allowed through to the detectors. The telescope collects background (solar), ultraviolet, and visible radiation and the polychromator redirects/rejects certain wavelengths using various sets of filters. The backscattered radiation is split at the first long wave pass filter, LWP. This filter lets backscattered visible radiation pass through while ultraviolet is redirected. Interference filters, IF, redirect the backscattered radiation to the corresponding channels according to wavelength in a filter cascade. Each channel has a PMT that the radiation is focussed upon using lenses, L, after the interference filters. The recording system can measure in photon counting and analog modes for the elastic channels and only photon counting for the other channels. It is important to limit the photon count rates in the detectors for the purpose of keeping the photon counts linear. At photon count rates above 25 MHz, the photon counting system

begins to deviate from linear counting.

There are a total of eight different detected channels in the polychromator for the CRL. There are two elastic scattering channels, 532 nm and 355 nm. There are two purely rotational-Raman shifted channels from the 532 nm laser at 531 nm and 529 nm. Another two channels detect vibrational-Raman shifts due to $N_2$ at 607 nm and 387 nm and there is a vibrational-Raman shifted channel for $H_2O$ detection at 408 nm. There is also a recently installed depolarization channel at 532 nm. Pertinent specifications of the CRL are in Table 3.1.

Table 3.1: CRL System Specifications

| Transmitter | |
| --- | --- |
| Laser #1 | |
| Model | Continuum Surelite III-10 |
| Wavelength | 532.08 nm |
| Pulse Energy | 380 mJ |
| Pulse Repetition Rate | 10 Hz |
| Laser #3 | |
| Model | Continuum Surelite III-10 |
| Wavelength | 354.72 nm |
| Pulse Energy | 240 mJ |
| Pulse Repetition Rate | 10 Hz |
| Receiver | |
| Telescope | Dal-Kirkham |
| Primary Mirror Diameter | 1 metre |
| Field of View | $0.3 - 2$ mrad |
| Data Acquisition | |
| Elastic Channels | 532.08 nm and 354.72 nm |
| Rotational Raman Channels | 528.60 nm and 531.00 nm |
| Vibrational Rotational Raman Channels ($N_2$) | 607.46 nm and 386.69 nm |
| Vibrational Rotational Raman Channel ($H_2O$) | 407.57 nm |
| Depolarization Channel | 532.08 nm |

A feature of the CRL is that it can be remotely operated. A suite of computer programs is used to remotely control the system in the Arctic. During an intensive measurement campaign it would be difficult to have an operator on site at Eureka to control the system. The computer programs make it possible to run the system without anyone on site. This also lets the operator run the system at almost any location with an internet connection.

## 3.1.2   Arctic High Spectral Resolution Lidar

The Arctic High Spectral Resolution Lidar (AHSRL) is a lidar also located at ØPAL, and measures elastic scattered light and separates the signal into contributions from particles and molecules. They are separated by taking advantage of the Doppler shifted photons due to thermal motion of molecules and particles. Molecular velocities in most cases are at least a factor of 10 higher than particle velocities which creates a larger frequency distribution of signal counts caused by molecules. The AHSRL splits the collected light with a beam splitter to a channel for aerosol and molecular counts and another channel for just molecular counts. For the molecular counts, the AHSRL uses an iodine absorption filter to separate the particle contribution of the signal thereby retrieving a pure molecular signal (*Eloranta*, 2005).

There are a couple of advantages to using this technique compared to a Raman lidar technique. The molecular scattering due to Doppler shifts has a larger scattering cross section than Raman-shifted scattering cross sections (Section 2.1). A small field of view, 45 $\mu$rad and fast repetition rate (4000 Hz) decreases the amount of the incoming scattered radiation within the telescopes view which decreases the near field signal counts allowing for photon counting (*Eloranta*, 2005). Also, the AHSRL does not have a calibration region needed for the calculation of $\beta_{aer}(z, \lambda_0)$ because it measures the total aerosol and molecular signal contributions. A disadvantage to this technique is that it only measures elastic backscatter and depolarization. Another disadvantage is due to the compact design of the AHSRL, some of the transmitted laser light is directed into the receiving system which has to be subtracted during the signal processing which can be difficult to accomplish. The AHSRL technique also involves using very narrow bandwidth filters, which can be difficult to implement (*Eloranta*, 2005).

## 3.1.3   Millimetre Cloud Radar

The Millimeter Cloud Radar (MMCR) is a type of radar that measures radar reflectivity, mean vertical velocities and Doppler Spectrum at a wavelength of 8.6 mm which is sensitive to cloud particle sizes. From radar reflectivity measurements, the volume backscatter cross section can be calculated, which is proportional to the sixth power of the diameter of the particle measured (*Liou*, 2002). Combining data from lidar and MMCR, the ratio of the

volume backscatter cross sections at different wavelengths can be calculated, also known as the colour ratio (*Bourdages et al.*, 2009). The calculated colour ratios can be related to particle sizes using a Mie scattering model.

## 3.2 Satellite-based Instruments

Two satellite instruments are used for the analyses in the following chapters, OMI and CALIOP. The Cloud-Aerosol Lidar with Orthogonal Polarization (CALIOP) is a downward pointing lidar that emits 532 nm and 1064 nm laser radiation and is mounted on Cloud-Aerosol Lidar and Infrared Pathfinder Satellite Observation (CALIPSO). The lidar can measure the volume backscatter cross section, depolarization, and colour ratio using both wavelengths. The Ozone Monitoring Instrument (OMI) is a nadir viewing ultraviolet-visible spectrophotometer on board the Aura satellite. OMI uses backscattered solar radiation in the visible and ultraviolet spectrum to measure several constituents in the atmosphere such as $O_3$, $NO_2$, $SO_2$, BrO, OClO. In this thesis it will be the $SO_2$ columns that are of interest.

## 3.3 Particle Trajectory Models

It is important to understand what a lidar is measuring and particle trajectory models are useful tools for that purpose. Two trajectory models are used in this thesis, Hybrid Single Particle Lagrangian Integrated Trajectory Model (HYSPLIT) and FLEXPART. HYSPLIT is a model that can compute the forward and back trajectories for multiple air masses. The forward trajectory analysis computes dispersion of particles from a source and the backward trajectory analysis determines the possible sources of particles that travelled to a particular location. It uses a Global Data Assimilation System from the National Weather Service's National Centres for Environmental Prediction for trajectory analyses. HYSPLIT also has the convenience of being an internet-based program for use by everyone.

FLEXPART is a Lagrangian particle model that can compute backward and forward trajectories similar to HYSPLIT. FLEXPART acquires meteorological information from sets of forecasts and analyses from the European Centre for Medium-Range Weather Forecasts model (*Stohl et al.*, 2005). The difference between FLEXPART and HYSPLIT is that FLEXPART has parametrizations for mixing and convection (*Draxler and Hess*, 2004).

The FLEXPART analyses shown in the following chapters are footprints. Footprint analyses show the residence times of particles released in the back trajectory that are within 0.5 km from the surface for a particular time period, which is used as an indicator for possible locations where particulates could have been acquired. The HYSPLIT measurements shown are single particle back trajectories which show the horizontal and vertical trajectories the single air parcel travels. The trajectories will help to determine possible mechanisms for the uplift of aerosol and water vapour in Eureka.

## 3.4   Instrument Commissioning and Characterization

### 3.4.1   Lidar Maintenance and Commissioning

In the winter of 2010, the CRL initiated its first measurement campaign which spanned the months January to April. To prepare for the campaign Dr. Graeme Nott and I travelled to Eureka for the purpose of maintenance and characterization of the lidar. The trip was taken during the early weeks of July 2009, at this time of year the temperature is warmest for the region which improves conditions for working outdoors. There were several tasks undertaken during the two week trip to Eureka. As flash lamps age, the power that is achieved by the laser diminishes and therefore have a finite lifetime, so the flash lamps for both lasers were replaced during this time. The seeder for the 532 nm laser was also replaced during the trip. This was due to it not being able to lock the laser at a specific wavelength as well as it should have been able to. It was also discovered during the trip that one of the Marx Bank was not working properly, so it had to be replaced in the visible laser.

### 3.4.2   Laser Alignment

#### 3.4.2.1   Introduction

In preparation for the winter campaign I wrote an automatic beam steering program. It was important to implement this program for the CRL for several reasons:

slow data transfer rate to client-side

repetitiveness of alignment procedure

increased accuracy

increased speed

The method used to align a telescope axis and beam axis with each other is to use backscattered photon counts from a high altitude region, where the position which gives the maximum photon counts is the aligned position. A high altitude region is used to make sure the altitude region is outside the incomplete overlap region. This method works if atmospheric conditions do not vary during the alignment process. However, if a cloud enters the alignment region the backscatter at that altitude will increase significantly affecting the results of the alignment. If there are clouds below the region of interest, the photon counts above the cloud will be diminished due to extinction in the cloud. The amount that it is diminished by can vary due to the cloud changing on short time scales.

There are two different methods of using the steering mirrors to align the beam axis with the telescope axis, the Gaussian and polynomial alignment techniques. The names of the techniques refer to how the fit is produced after the data photon counts are retrieved for each altitude region. There are two techniques used for the alignment because in some cases it is best to have a quick alignment (polynomial alignment) over a robust alignment (Gaussian alignment) or vice versa.

Figure 3.2 shows a graphic of how the field of view for the telescope is tracked by the beam steering program for a single mirror. The method for moving the mirror starts off by scanning across the field of view in one direction with measurements being taken at discrete intervals and altitudes. After the program decides to stop travelling in one direction it will reverse and travel back to the original position to repeat the process for the other direction. The Gaussian technique reverses when the beam has exited the field of view for the altitude region and the polynomial technique reverses when the photon counts are half of the current maximum photon counts measured during the alignment process.

### 3.4.2.2  Gaussian Alignment

When the lidar needs a robust alignment, the Gaussian technique is used. When the program has finished tracking the beam across the field of view (See Section 3.4.2.1), the user has two options for the program to take. It can either stop there and attempt to fit the data or it can do a second scan of the regions with the highest slope in the signal with respect
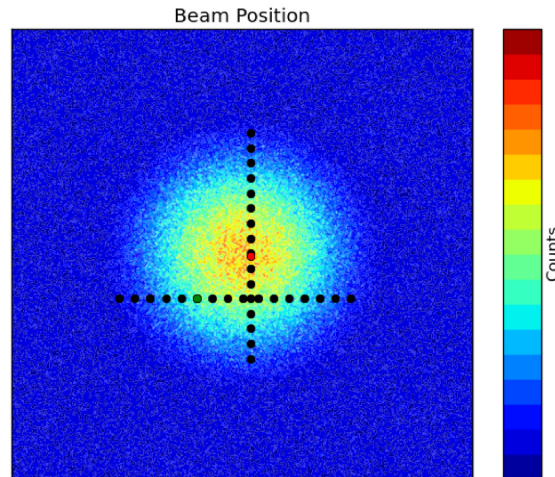
Figure 3.2: Graphic representing simulated signal counts collected by a telescope having the laser at different positions within in its field of view (FOV). The black dots represent the track the beam steering program travelled for each axis (horizontal and vertical). The green dot is the starting position and the red dot is the final position.

to position. The technique for the Gaussian fit uses the positions of highest slope in determining its initial guess at the centre position. The second scan will provide more points for the initial guess at the centre position as described in the next paragraph. After the second scan is complete or the initial scan is complete, the program will attempt to fit the data.

The fit for the Gaussian technique determines the locations that have maximum change in signal on each side of the signal distribution with respect to the actuator position. The fitting program assumes a symmetric Gaussian distribution for the photon counts with respect to position and finds an initial centre value by using the position in the middle of the positions with the highest slope. The fitting program will then use a least squares fit for a Gaussian shaped peak to optimize the centre position. A sample measurement of one of the actuators is shown in Figure 3.3.

### 3.4.2.3   Polynomial Alignment

When a fast paced alignment is needed the polynomial technique is used. For this purpose, the polynomial technique reverses direction when the photon counts are half of the current maximum photon counts for the altitude region. Once the data collection process has finished for the polynomial technique, a fit is done on the set of photon counts using a
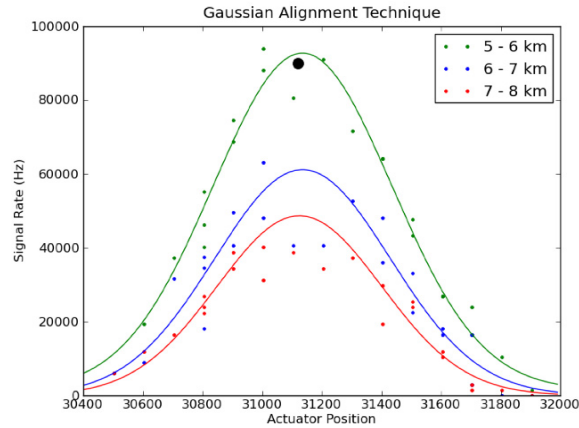
Figure 3.3: Gaussian alignment technique output for three different altitude regions in the legend. The dots represent the data collected during the alignment and the corresponding lines are the Gaussian fits for each altitude region. The black dot is the centre position chosen.

quadratic least squares fit. The reason for not doing a Gaussian fit is because the shape of curve created by the data resembles a quadratic so a polynomial fit is used instead. Figure 3.4 shows an example of a set of data for the polynomial fit along with the final position.

### 3.4.2.4 Comparison of the Techniques

There are advantages and disadvantages to both techniques beam steering methods. The Gaussian technique is a more robust technique than the polynomial technique. As long that the original position is within the FOV, the Gaussian technique will find the centre of the distribution. The polynomial technique needs to have a large amount of signal to start off with or it may exit the field of view of the telescope. For cases where the original position is not within the field of view of the telescope, for the altitude region of interest, a manual alignment will have to be done where the operator moves the actuators until there are photon counts in the altitude region. At this point the Gaussian alignment technique can be used to find the exact position.

The polynomial alignment techniques advantage over the Gaussian alignment techniques is that it is much faster. The polynomial alignment technique is approximately twice as fast as the Gaussian alignment and this is because it does not track as far from the original position. The Gaussian alignment on average takes approximately 20 minutes to align while the polynomial alignment takes 10 minutes on average. An issue with the
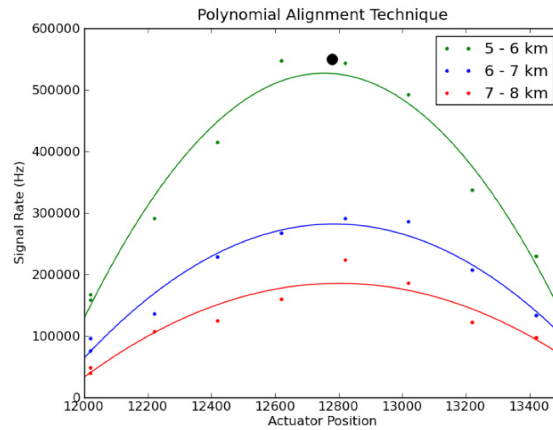
Figure 3.4: Polynomial altitude technique output for three different altitude regions in the legend. The dots represent the data collected during the alignment and the corresponding lines are the polynomial fits for each altitude region. The black dot is the centre position chosen.

Gaussian alignment technique is that it fails at altitudes with low photon counts. In most cases the Gaussian alignment technique fails at altitudes greater than 8 km. This occurs because the fit can not find the regions of largest slope during the initial fitting process if the signal is too low.

During the winter campaign, the alignment of laser's was monitored for each measurement and the results show that the position of optimal alignment has changed significantly in March but was steady before and after that as shown in Figure 3.5. The time that the alignment did change significantly was likely due to maintenance of the UV laser during that time. Before March 2010, there was only a fluctuation of approximately 0.02 mrad in the angular pointing of each actuator which is small compared to the minimum FOV of 0.3 mrad which is used during alignment. The smallest field of view for the telescope to get the most accurate alignment possible. This shows that there is very little day to day drift in the alignment, except for when there are physical changes to the lidar. It is best to use the Gaussian technique if there is a change in the physical lidar system or if the lidar has not been used for a long period of time in case there was a drift in the alignment. For day to day alignments during a campaign, it is fine to use the polynomial technique to save time.
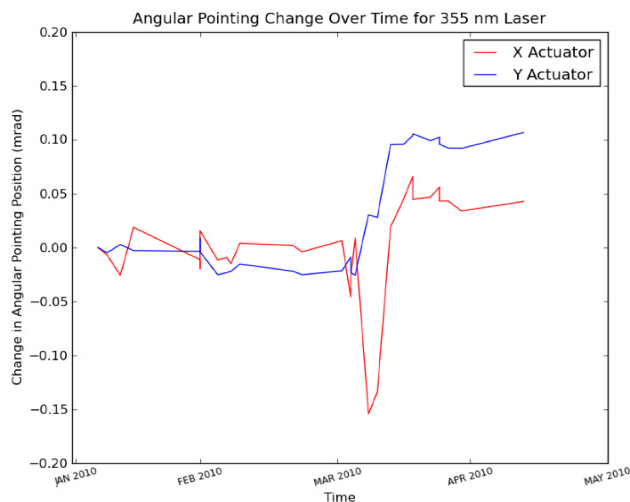
Figure 3.5: Change in alignment of UV angular pointing direction during the winter 2010 measurement campaign for both axes

## 3.5 System Performance

Tracking the performance and operations of a lidar is important to understand how the pieces of the instrument vary with time. Knowing this will be helpful in analyses of measurements that could contain changes in the lidar system. For example, changes in the lidar system could change the overlap region and it could also affect the calibration constants used for temperature and water vapour analyses by changing the power of the measured signals. Keeping track of the performance and operations will be helpful in determining possible changes to the above items and how to remedy those changes.

### 3.5.1 Operations Data

During each measurement in the winter 2010 campaign the CRL's measurement settings were archived and used for the purpose of tracking its physical condition over time. The following parameters were monitored: totals shots, flash lamp shots, power measurements, operator of software, aperture stop size, field stop size, delay stage position, PMT voltages, and discriminator settings.

As the instrument ages, several pieces of hardware may need to be replaced such as optics and flash lamps. Keeping track of the changes with power of the lasers over time can help determine when there could be an issue with a piece of equipment. Figure 3.6
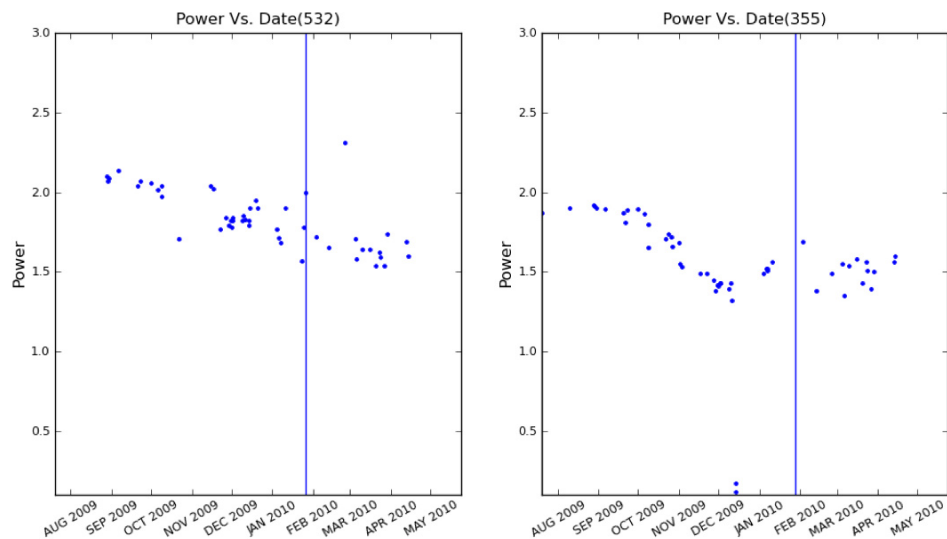
Figure 3.6: Power Measurements at the beginning of each measurement with time for the UV and VIS lasers. The power measurements are split up into two segments for each laser because of when the flash lamps in the laser were replaced.

can keep track of when a significant change in the system occurred, for example a vertical bar indicates a change to a new set of flash lamps. A variation of this plot is the power of the lasers with increasing flash lamp shots, and this shows how the power changes with increasing shots on the lasers to give a different perspective of the variations with the power. When comparing the power with the flash lamp shots it is easier to compare one set of flash lamps to another because one set of flash lamps may not be used at the same rate as another. It is also important to track the flash lamp shots over time because as the flash lamps age they change the thermal characteristics of the laser cavity which can change physical system properties.

In Figure 3.6 there is number of areas where there are significant changes in the laser power. In the second segment there was a gradual drop in power which would be due to the flash lamps ageing. There is a single measurement in the second segment of the 532 nm laser plot that has power at 2.5 W but this was only due to the seeder accidentally being turned off.

For the 355 nm laser there were quite a few regions where there were drastic changes in the power as well. During December of 2009 there was a drastic drop in power for the 355 nm laser which was caused by the Marx Bank breaking and needing to be replaced. Another feature seen in the second segment after the flash lamps were replaced is that there
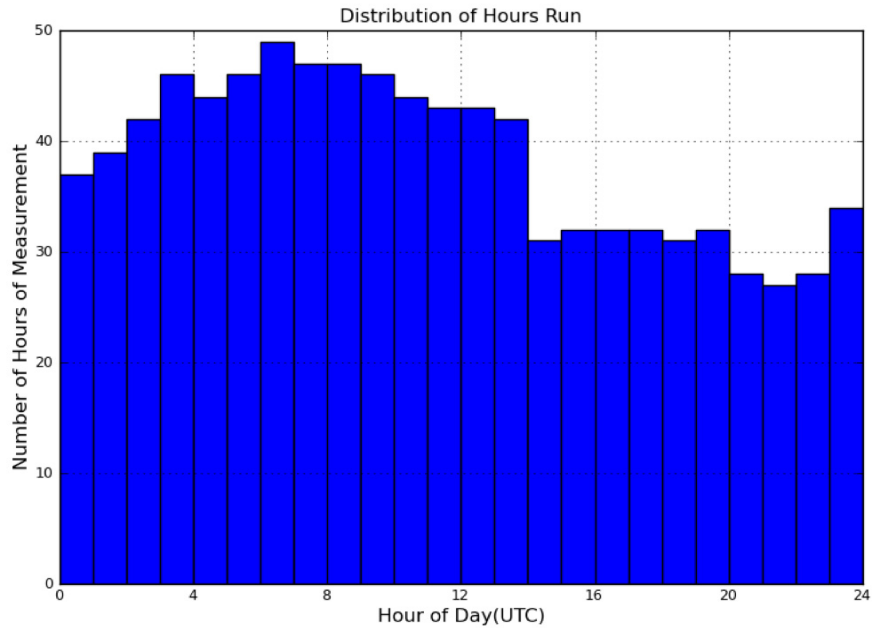
Figure 3.7: Distribution of hours run for CRL during Winter 2010 measurement campaign

power did not increase with the new flash lamps for either the 532 nm or 355 nm lasers. A possible cause for this could be that the decrease in power in the previous segment was not due to the flash lamps ageing. A possible reason for the drop in power could actually be due to burn marks on optics in side the lasers or between the lasers and power meter.

Figure 3.7 shows the distribution of hours run during a measurement. The purpose of this plot is to show if there is biasing of the data by measuring during only certain times of the day. The distribution of hours run is fairly flat, suggesting that the potential for this is small.

## 3.6   Aerosol and Cloud Inversion Technique Comparison

In this section a comparison of results from the Coffin, Klett, and ratio inversions using the 532 nm elastic and 607 nm Raman channels from CRL measurements are shown. The Raman inversion will not be discussed due to it using larger altitude resolutions (See Section 2.2.2) than the other three techniques. All three inversions calculate $\beta_{aer}(z, \lambda_0)$, $\alpha_{aer}(z, \lambda_0)$ is not shown since it is only a modified product of $\beta_{aer}(z, \lambda_0)$ by use of the aerosol lidar ratio. The purpose of this comparison was to determine which inversion technique is most

appropriate for this system. For the following measurements, the Klett inversions lidar ratio was tuned so it would match the calculation of $\beta_{aer}(z, \lambda_0)$ for the ratio and Coffin inversions. The Coffin inversion is only slightly affected by the changes in the lidar ratio as compared to the Klett inversion (See Section 2.2.3), therefore lidar ratios from the Klett inversion are used to adjust the Coffin, which is further tuned by varying the Ångstrom exponent, $k$.

### 3.6.1 Case I: Low Aerosol Concentration

Figure 3.8 is a measurement from January 21, 2010 for the three different inversions. There are two distinct layers of aerosol in this measurement, one between 3 km and 5 km and another that reaches the surface extending to approximately 2 km. Within the lowest layer of aerosol is a stronger band of aerosol at 1 km.
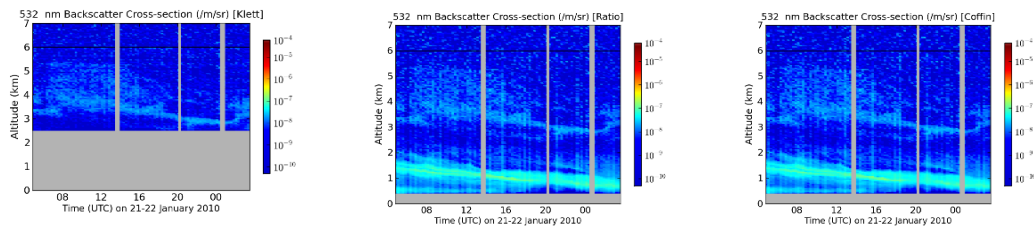


Figure 3.8: January 21, 2010 contour measurement of a) Klett inversion time series b) ratio inversion time series c) Coffin inversion time series

The Klett inversion did not detect anything reasonable below 2.5 km due to the incomplete overlap region which is why the plot is cut off at that altitude. The incomplete overlap region decreased the photon counts in the 532 nm channel which would also correspond to a decrease in $\beta_{aer}(z, \lambda_0)$ for the Klett inversion. The ratio inversion and the Coffin inversion detected the lowest aerosol layer down to approximately 400 metres and do not detect anything below that altitude due to differential overlap between the 532 nm and 607 nm channels. The differential overlap region created the same effect for the ratio and Coffin inversions as the incomplete overlap region did for the Klett inversion. For this measurement there was not a significant difference between the Coffin and ratio inversions.

Figure 3.9 shows a set of profiles for the same measurement but between the altitudes of 5 km and 20 km. The profiles shown are for the Klett, Coffin, and ratio inversions which all show a stratospheric layer of aerosol. There was no significant difference between values of $\beta_{aer}(z, \lambda_0)$ for the three techniques. The Klett inversion showed a slightly smoother profile
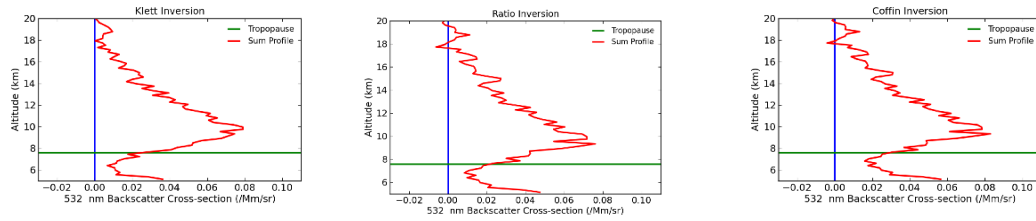
Figure 3.9: January 21, 2010 summed profile measurement of a) Klett inversion b) ratio inversion c) Coffin inversion

for the calculation of $\beta_{\text{aer}}(z, \lambda_0)$ while the ratio and Coffin inversions both had more noise because those techniques use two signals instead of one.

## 3.6.2   Case II: Low Optical Depth Cloud
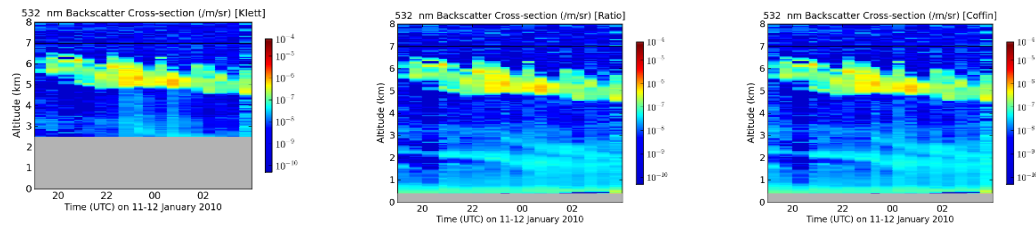


Figure 3.10: January 11, 2010 contour measurement of a) Klett inversion time series b) ratio inversion time series c) Coffin inversion time series

Figure 3.10 is a measurement from January 11, 2010 of a low optical depth cloud between 5 km and 7 km. The three inversions measure similar $\beta_{\text{aer}}(z, \lambda_0)$ values within the cloud. As in the previous measurement, the Klett inversion only retrieves measurements down to approximately 2.5 km while the Coffin and ratio inversions measure down to 400 metres. The Coffin and ratio inversions also measure similar values of $\beta_{\text{aer}}(z, \lambda_0)$ below the cloud showing a clear region between 4 km and 5 km and aerosol below 4 km. The Klett inversion showed a slight increase in $\beta_{\text{aer}}(z, \lambda_0)$ below the cloud between 23:00 UTC and 01:30 UTC and between 2.5 km and 5 km, which could be caused by slight changes in the optical properties of the cloud, therefore changing the lidar ratio of the cloud during that time frame of the measurement.

### 3.6.3  Case III: High Optical Depth Cloud

In Figure 3.11, there is a measurement from February $03-04$, 2010 of a high optically depth cloud. The cloud arrived at 21:00 UTC on February 03, 2010 which descended over time to approximately 1 km at the end of the measurement. There was very little aerosol throughout the troposphere during this measurement.
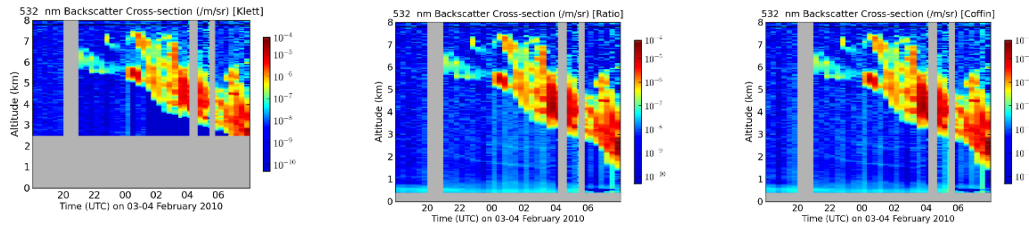


Figure 3.11: February 03-04, 2010 contour measurement of a) Klett inversion time series b) ratio inversion time series c) Coffin inversion time series

Figure 3.11 shows how the Klett inversions constant lidar ratio underestimated $\beta_{\text{aer}}(z, \lambda_0)$ below the cloud after 01:30 UTC as indicated by the dark blue region. The ratio and Coffin inversions retrieve the same $\beta_{\text{aer}}(z, \lambda_0)$ throughout the cloud but the ratio inversion has a slight enhancement below the cloud due to differential cloud extinction from the two different measured lidar signals. In this case, the differential extinction causes an increase in $\beta_{\text{aer}}(z, \lambda_0)$ within the cloud which also causes an increase in $\beta_{\text{aer}}(z, \lambda_0)$ below the cloud. The reason for this is that the differential extinction will cause the ratio of the backscattered radiation at the 532 nm and 607 nm wavelengths to be different above and below the cloud for clear regions. In this case the calibration region (See Section 2.2) was chosen to be above the cloud, so the analysis will show a change in the clear region below the cloud. The Coffin inversion does not show this effect because it accounts for differential extinction via the Ångstrom exponent, $k$ (See Section 2.2.3). The Ångstrom exponent only needs to be slightly adjusted to account for the differential cloud extinction by increasing it from 0 which is its default value for clouds to 0.2.

Figure 3.12 shows a comparison of $\beta_{\text{aer}}(z, \lambda_0)$ for the ratio and Coffin inversions, which is averaged between 1.75 km and 2.25 km for the entire measurement, which shows the same results as in Figure 3.11. At approximately 01:00 UTC on February 04, 2010 the ratio inversion averaged $\beta_{\text{aer}}(z, \lambda_0)$ increased systematically until 04:00 UTC, which is where the cloud contaminated the altitude region.
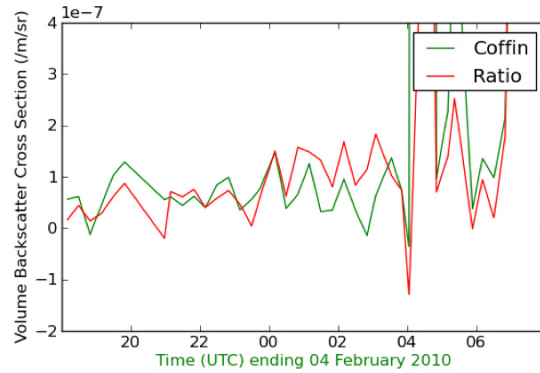
Figure 3.12: $\beta_{\text{aer}}(z, \lambda_0)$ Comparison of ratio and Coffin Inversion Time Series for February $03-04$, 2010

## 3.6.4   Discussion

For the measurements shown, the Coffin and ratio inversions both calculate similar values for $\beta_{\text{aer}}(z, \lambda_0)$ at all altitudes. The only time that the Coffin and ratio inversions vary is in high optical depths where differential extinction can have a significant effect on the calculated retrievals as in Case III. The Klett inversion calculates the same values for $\beta_{\text{aer}}(z, \lambda_0)$ in most cases except when near the surface. At the moment a correction for the incomplete overlap region is used, but it only corrects for values down to approximately 2.5 km in most cases.

The assumption of a constant lidar ratio and Ångstrom exponent is not optimal in all situations. In Case III, the Klett inversion and Coffin inversions were separated into two sections because the lidar ratio and Ångstrom exponent changed throughout the cloud in the measurement. For the Klett inversion, there was still issues with the lidar ratio assumption and it only worked up until 01:30 UTC due to changes in cloud particle properties. For the Coffin inversion, the same lidar ratios are used as in the Klett inversion and then the Ångstrom exponent is adjusted for each section. For Case III, the calculation of $\beta_{\text{aer}}(z, \lambda_0)$ was reasonable but there was vertical striping below the cloud due to small changes in either the Ångstrom exponent or lidar ratio that could not be corrected. The ratio inversion shows a systematic increase in $\beta_{\text{aer}}(z, \lambda_0)$ as shown in Figure 3.11 and Figure 3.12 due to differential extinction which it is not being accounted for in this technique.

In situations where the optical depth is low during the measurement and at a high altitude, it is optimal to use the Klett inversion because there is less noise when calculating

$\beta_{\mathrm{aer}}(z, \lambda_0)$ from a single signal. For cases where it is important for the signal to have absolute calibration with a molecular signal to retrieve the most accurate values for $\beta_{\mathrm{aer}}(z, \lambda_0)$, the ratio or Coffin inversions should be used. When the optical depth is high there can be a significant amount of differential extinction which can affect the ratio inversion. The optimal technique in high optical depth cases is the Coffin inversion as shown by the results of Case III. During the campaign, Case III was the only measurement that needed to be corrected for differential extinction. Due to the difficulty in setting up the Coffin inversion, most cases throughout this thesis will use the ratio inversion.

# CHAPTER 4

# WINTER 2010 MEASUREMENT CAMPAIGN

## 4.1 Introduction

During the winter months of 2010, the CRL obtained quasi-continuous measurements for its first measurement campaign. Data was collected 5 days a week and 24 hours per day for the months of January, February, March and April except during periods of downtime when repairs were needed or when weather prevented the hatch from being opened.

Figure 4.1 shows the times at which the CRL was measuring during the campaign. The CRL would not measure if there was low cloud extinguishing the signal or large amounts of precipitation. There was a total of approximately 900 hours of measurements in the campaign predominately done in the months of January, February, and March. Later into the season, downtime from upgrades to the system and deteriorating weather conditions decreased the number and length of measurements possible. The campaign ended in April due to the solar sunrise. The Raman scattered channels are overwhelmed by solar radiation during daylight hours. During the measurement campaign I participated in taking measurements with three colleagues and I was responsible for analysing the aerosol analysis for both the 532 nm and 355 nm elastic channels.

There were a variety of measurements during the winter campaign that contained both aerosol and cloud features. A number of the aerosol features coincide with features of the water vapour measurements. It will be shown by HYSPLIT and FLEXPART trajectories that these aerosol and water vapour features both likely originated from varying mid latitude locations. Measurements of aerosols from the CRL and several other instruments showed

aerosol in the lower stratosphere that diminished slowly over time during the campaign. It is believed that the aerosols are from the Sarychev eruption that occurred on June 12, 2009 (*Levin et al.*, 2010). These topics will be discussed further in the following chapter.
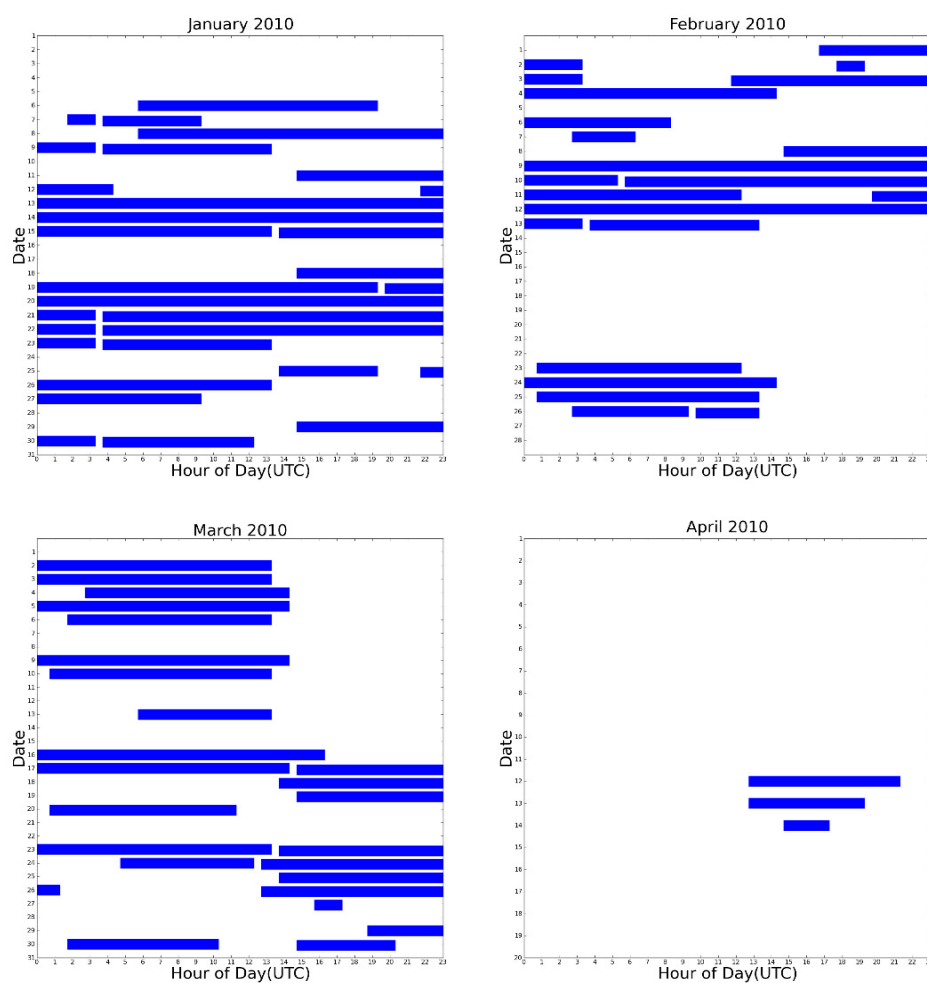


Figure 4.1: 2010 measurement campaign distribution of operations throughout the Winter in terms of hours run by the Operators. Each individual sub plot shows the distributions of hours the CRL was run for the months of January, February, March, and April 2010.

## 4.2 Aerosol and Water Vapour Measurements



(a)                                                                    (b)
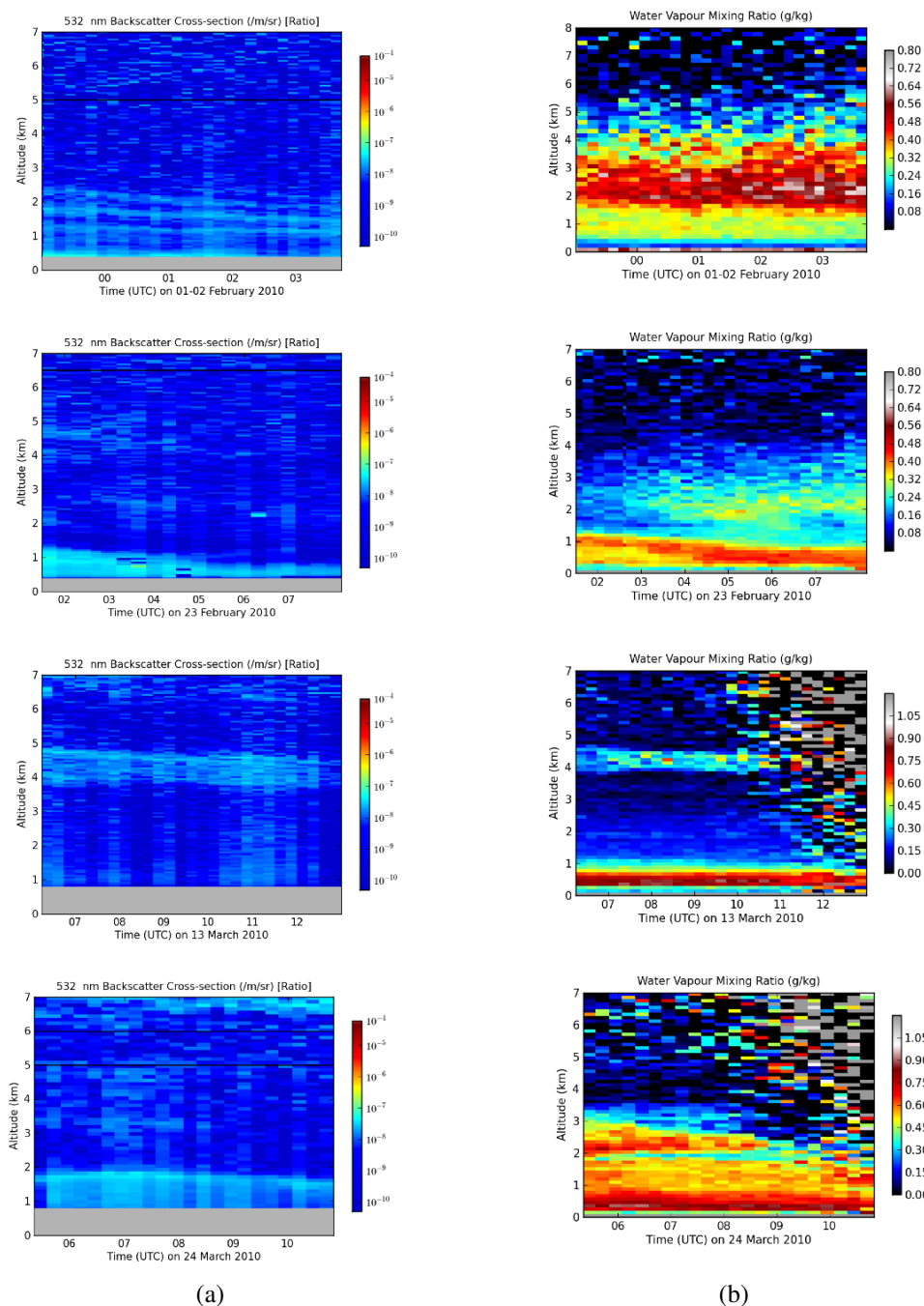
Figure 4.2: Winter 2010 Measurements of Aerosol and Water Vapour layers a) Aerosol Backscatter Cross Section and b) Water Vapour Mixing Ratio Intensities (Credit: J. Doyle). These measurements show one or two layers of aerosol which also contain high water vapour mixing ratios. These measurements also contain layers that have no aerosols and low water vapour mixing ratios.

During the winter 2010 campaign, there were several instances of measurements in the aerosol and water vapour channels that showed layering in the troposphere. The layering structure in the measurements often coincided with aerosol and water vapour features, suggesting the layers originated from different locations. This section will describe a few of these measurements and show back-trajectories indicating where the air masses originated and how they were formed. Several HYSPLIT trajectories were simulated at different starting locations in each layer and the plots shown in the following section are representative simulations for each layer. FLEXPART footprint simulations are also shown for each layer.

### 4.2.1   Case I: Correlated Aerosol and Water Vapour Layers

There were several measurements that had high water vapour ($> 0.2$ g/kg) in layers collocated with high aerosol concentrations ($> 5 \times 10^{-8}$ /m/sr) or moist aerosols. Due to the small number of cases seen in the aerosol measurements where there was influence of differential extinction (See Section 3.6), it is assumed that differential extinction is insignificant for the water vapour retrieval as well. High water vapour in the Arctic is still low compared to mid-latitudes, total column precipitable water during the winter season in the Arctic is approximately 2.5 mm while the global average is 25 mm (*Serreze and Barry*, 2005). Figure 4.2 shows a few measurements during the campaign that have these features. There are one or more layers that exhibit these features from each measurement. Several moist aerosol layers are in lower altitudes near the surface and there are a few in the upper troposphere.

Figure 4.3 provides a measurement from January 21, 2010 of the $\beta_{\mathrm{aer}}(z, \lambda_0)$ and water vapour mixing ratio ranging from the surface to an altitude of 7 km. The $\beta_{\mathrm{aer}}(z, \lambda_0)$ time series was described previously in Section 3.6.1. The water vapour mixing ratio and the $\beta_{\mathrm{aer}}(z, \lambda_0)$ time series shows there are two moist layers in this measurement. The aerosol-free region ($< 10^{-8}$ /m/sr) between the two layers of aerosol also corresponds to the region in the water vapour mixing ratio plot that has low water vapour ($< 0.1$ g/kg) which can be considered dry clean air. HYSPLIT and FLEXPART analyses from Figure 4.4 and Figure 4.5 shows back trajectories for the January 21, 2010 measurement.

Back trajectories for the 0 km to 2 km layer of moist aerosol from HYSPLIT and FLEX-PART show possible origins of aerosol from Northern Eurasia. Northern Eurasia is likely the location for the aerosols due to anthropogenic pollution sources in the region. FLEX-PART footprint simulations also show a possible location for acquisition of water vapour

Figure 4.3: January 21, 2010 time series measurement of a) Aerosol Backscatter Cross Section and b) Water Vapour Mixing Ratio Intensities (Credit: J. Doyle).
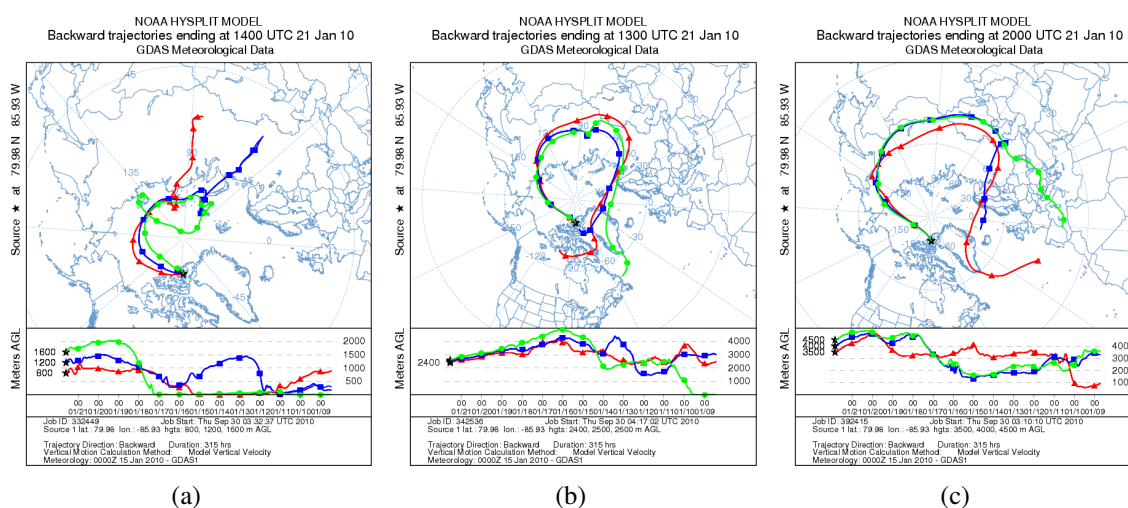


Figure 4.4: HYSPLIT Analysis for January 21, 2010. HYSPLIT trajectories are shown for a) 0-2 km, b) 2-3 km, c) and 3-5 km. The HYSPLIT backward trajectories are for 13 day simulations.

being the Atlantic Ocean. Several sets of HYSPLIT trajectories were simulated for this region but only a few showed trajectories reaching as far as Northern Greenland, indicating no water vapour would be retrieved. This could be because the HYSPLIT trajectories are only 13 day simulations while the FLEXPART are 15 day simulations. It could also be due to the fact that HYSPLIT is only producing single trajectories while FLEXPART results are from thousands of trajectories.

The layer of moist aerosol between 3 and 5 km shows a set of trajectories which pass through Northern Eurasia and some trajectories leading to the Atlantic Ocean, according to HYSPLIT simulations. FLEXPART footprint simulations match with HYSPLIT simulations showing large residence times located over Northern Africa, Eurasia, and the Atlantic
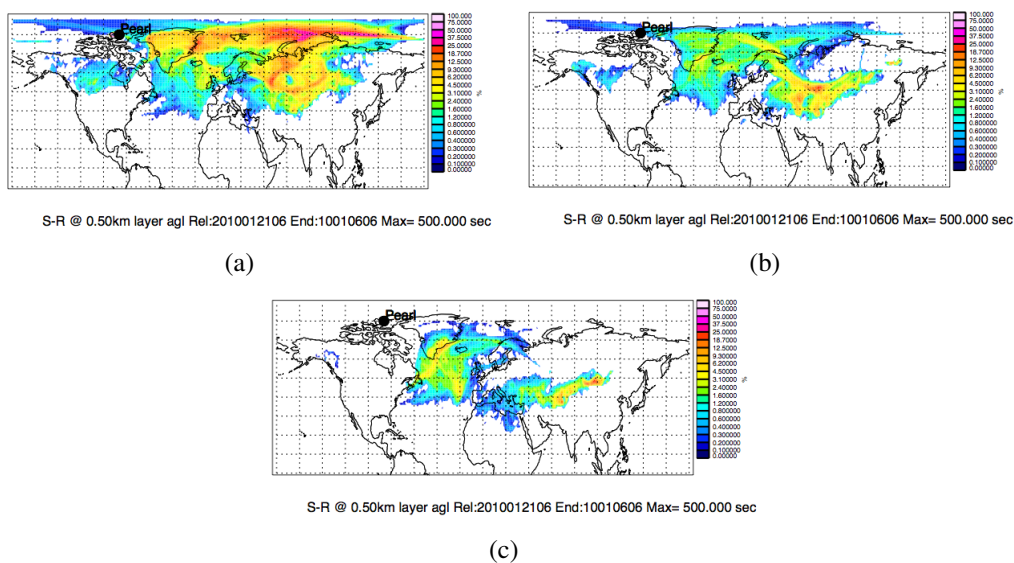
Figure 4.5: FLEXPART Footprint Analysis for January 21, 2010. Footprint analyses are shown for a) 0-2 km, b) 2-3 km, c) and 3-5 km. The footprint simulations are 15 day backward simulations. (Credit: Richard Damoah)

Ocean. Water vapour would have been attained from the Atlantic Ocean and aerosols would have either been dust from Africa or pollution from Eurasia. The HYSPLIT trajectories over the Atlantic Ocean show there is rapid ascent from the surface of the ocean. This rapid ascent could be a possible method for acquisition of water vapour from the Ocean for this air mass.

According to HYSPLIT and FLEXPART, the layer of dry air between at 2 km and 3 km has trajectories that are similar to the layer between 3 and 5 km. In most HYSPLIT particle trajectories it circled back to the Arctic, but some trajectories lead to the Atlantic which is also shown by the small residence times from FLEXPART footprints over the Atlantic Ocean. FLEXPART footprint simulations have lower residence times which indicates less time being spent near the surface which could be the reason why this layer is void of aerosol and water vapour while the layer above is not. The residence times over land are fairly large though, this could be due to the layer altitude range being too large and encompassing part of the aerosol layer above 3 km. The layer may also have too small of an altitude range for the model to interpret properly.

## 4.2.2 Case II: Anti-Correlation of Aerosol and Water Vapour Layers

There have also been a number of atmospheric events that had high $\beta_{aer}(z, \lambda_0)$ in areas of low water vapour mixing ratio (dry aerosols). Figure 4.6 shows a couple of measurements that have dry aerosol layers throughout the measurement campaign. Some cases do have small amounts of water vapour in the layer but it was diminished compared to the amounts of water vapour in surrounding air masses. The dry aerosol regions occur at varying altitudes throughout the sets of measurements.



(a)                    (b)
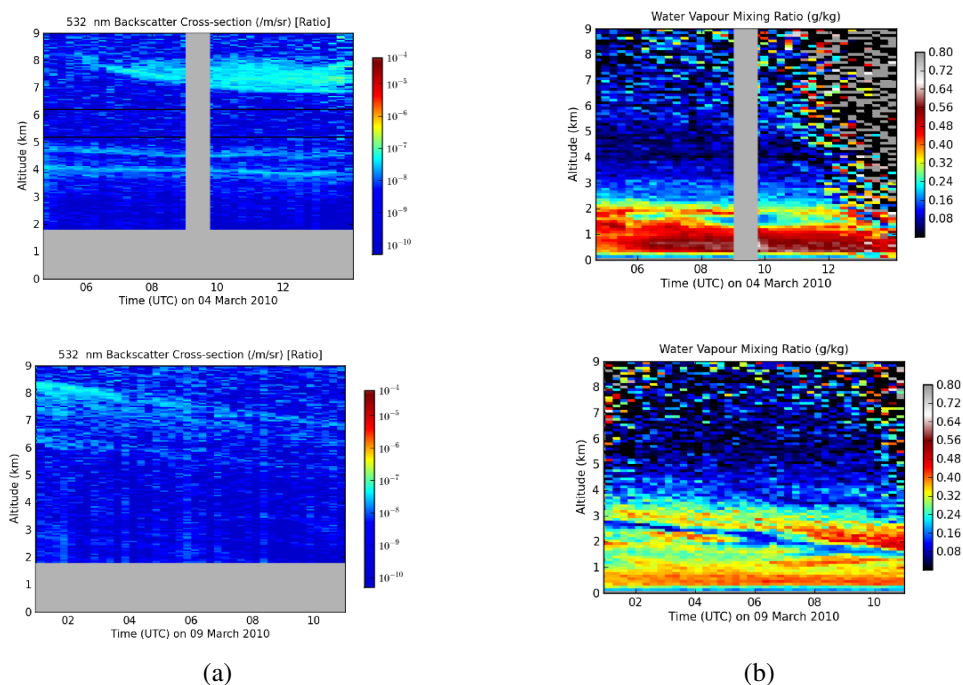
Figure 4.6: Winter 2010 Measurements of Aerosol and Water Vapour layers which are not co-located a) Aerosol Backscatter Cross Section and b) Water Vapour Mixing Ratio Intensities (Credit: J. Doyle)

Figure 4.7 shows another measurement with a dry aerosol layer from March 06, 2010. During this measurement there is an aerosol layer between 3 to 5 km at the beginning of the measurement that decreased in altitude slowly until it exited the CRL measurement region at approximately 09:00 UTC. After the aerosol layer left the measurement region there was an increase in the background aerosol throughout the troposphere.

The water vapour mixing ratio was low in the region of high $\beta_{aer}(z, \lambda_0)$ between 3 km and 5 km at the beginning of the measurement (dry aerosol layer). Between 2 km and 3 km there was an area with a high water vapour mixing ratio and no aerosol (moist clean

layer). Below this layer between 0 km and 2 km there was another moist clean layer but with diminished water vapour compared to the previous layer. Above the region with the aerosol there was another moist clean layer that reached up to 5.5 km. Throughout the measurement the layers all decreased in altitude.
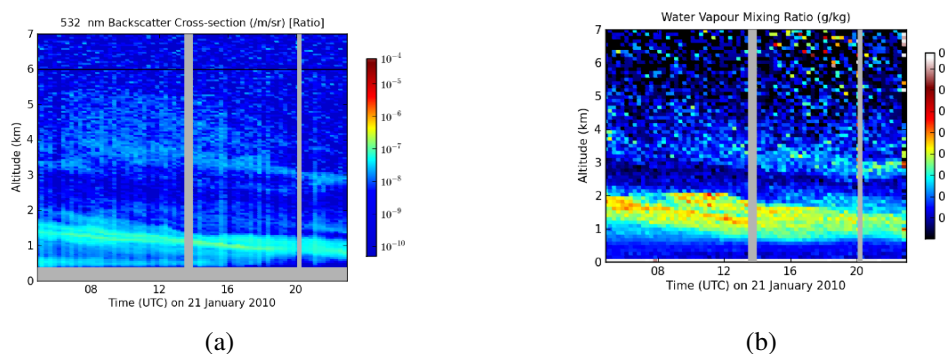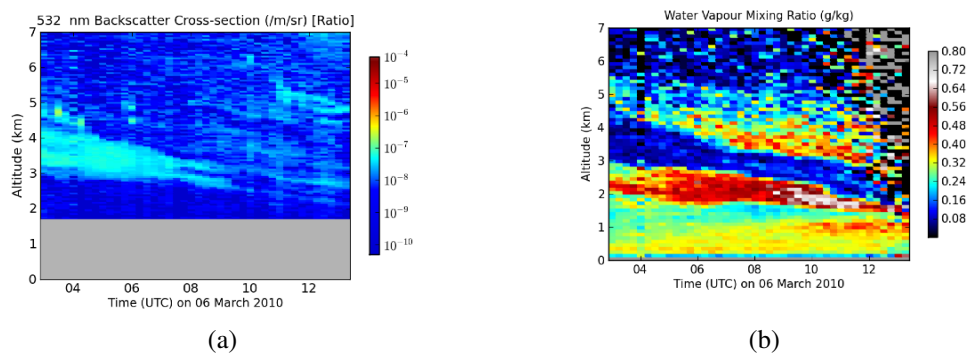


Figure 4.7: March 06, 2010 Time Series Measurement of a) Aerosol Backscatter Cross Section and b) Water Vapour Mixing Ratio (Credit: J. Doyle) Intensities which contains multiple layers of water vapour with no aerosols and a low water vapour mixing ratio layer with a large aerosol intrusion.

Figure 4.8 shows HYSPLIT particle back trajectories and Figure 4.9 shows FLEXPART footprint simulations for the four regions mentioned. The moist clean layer between 2 and 3 km has HYSPLIT back trajectories and FLEXPART footprints which suggest that the Pacific Ocean was a possible acquisition location for water vapour. Rapid ascent of water vapour is shown in HYSPLIT trajectories over the Pacific Ocean uplifting air from the surface of the ocean as in the case on January 21, 2010. According to HSYPLIT, the region with diminished water vapour between 0 km and 2 km has trajectories that circle over the Arctic Ocean that have been descending during the simulation. FLEXPART footprints show very small residence times near Eureka which matches with HYSPLIT results. The water vapour at this moist layer could have been acquired before the simulated trajectories end.

HYSPLIT suggests that the dry aerosol layer has trajectories passing over Eurasia and Canada. FLEXPART footprints for the aerosol layer show similar trajectories indicating sources of anthropogenic pollution or desert dust from either Eurasia or USA. FLEXPART and HYSPLIT both show that the trajectories could have possible origins from the Pacific and Atlantic Ocean. FLEXPART has lower residence times near Ocean surfaces than compared to the residence times near the surface of land masses, which indicates there is a

smaller possibility of attaining water vapour.



Figure 4.8: HYSPLIT Analyses for March 06, 2010 using HYSPLIT at a) 0-2 km, b) 2-3 km, c) 3-4 km, d) 4-5.5 km. The HYSPLIT backward trajectories are for 13 day simulations.

The moist layer between 4 km and 5.5 km has trajectories from HYSPLIT that shows water vapour could have been acquired by rapid ascent over the Atlantic Ocean at the end of the simulation or during travel over the Pacific Ocean. FLEXPART shows similar results: the water vapour could have been acquired at either the Atlantic or Pacific Oceans with larger residence times near the surface of the Pacific Ocean. The previous dry aerosol layer had similar footprint locations but showed the largest residence times over landmasses in USA and Eurasia while this layer showed larger residence times over the Pacific Ocean

indicating the two layers are represented correctly in the simulation. There were also large residence times spent over Eurasia for the moist layer as well but this could be due to errors in the altitude range chosen for the simulation of this layer.



S-R @ 0.50km layer agl Rel:2010030603 End:10021903 Max= 500.000 sec

(a)

S-R @ 0.50km layer agl Rel:2010030603 End:10021903 Max= 500.000 sec

(b)

S-R @ 0.50km layer agl Rel:2010030603 End:10021903 Max= 500.000 sec

(c)

S-R @ 0.50km layer agl Rel:2010030607 End:10021906 Max= 500.000 sec

(d)
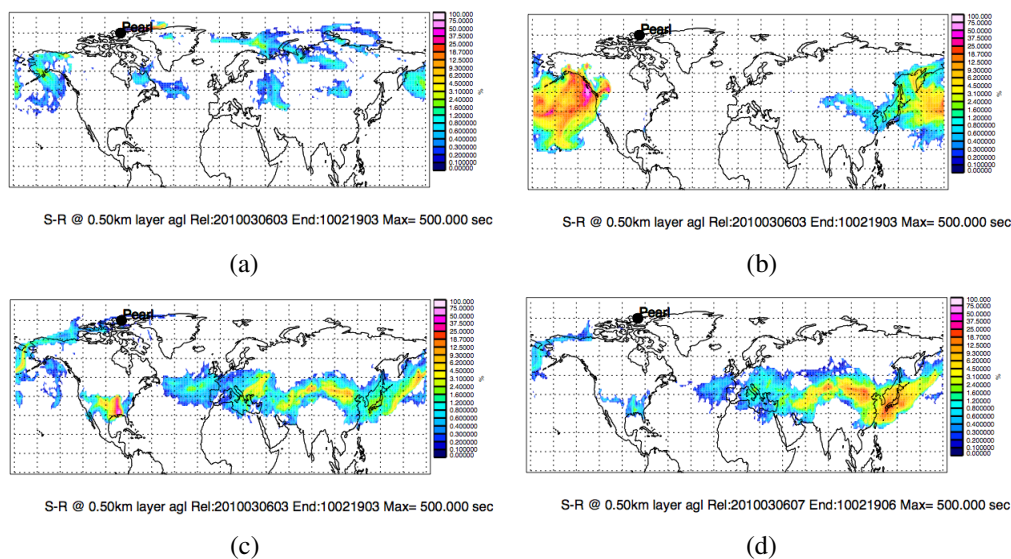
Figure 4.9: FLEXPART Analyses for March 06, 2010 using FLEXPART at a) 0-2 km, b) 2-3 km, c) 3-4 km, d) 4-5.5 km. The footprint simulations are 15 day backward simulations. (Credit: Richard Damoah)

## 4.2.3 Case III: Correlation and Anti-Correlation of Aerosol and Water Vapour Layers

Some measurements also contained regions with moist and dry aerosol layers. Figure 4.10 shows a measurement from March 05, 2010 which shows these features. March 05, 2010 had several strands of aerosols throughout the troposphere during the measurement. The two aerosol features that are discussed is a dry aerosol layer that entered at 08:00 UTC between 5 km and 6 km and the second feature is a moist aerosol layer near the surface to approximately 3 km for the entire measurement. Between the two aerosol layers there were another two layers, one between 2 and 3 km that is dry and another which is moist above it between 3 and 5 km, which descended during the measurement down to between 3 km and 4 km.
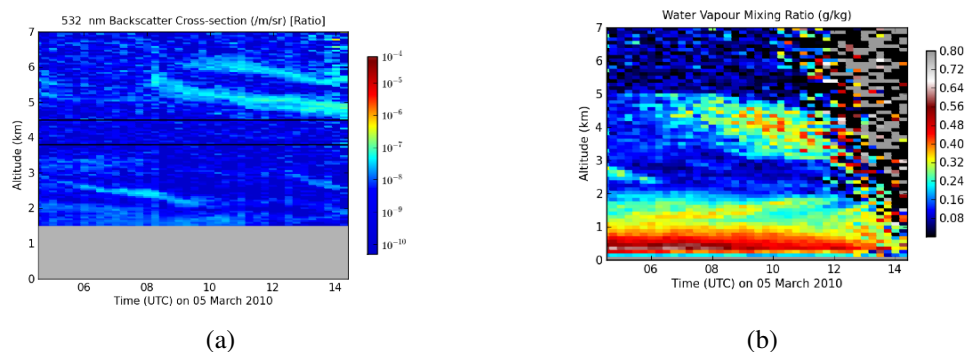
Figure 4.10: March 05, 2010 Time Series Measurement of a) Aerosol Backscatter Cross Section and b) Water Vapour Mixing Ratio Intensities (Credit: J. Doyle)

The dry and moist aerosol layers from this measurement are most likely from different locations due to the changes in the water vapour mixing ratios between them. Figure 4.11 and Figure 4.12 shows back trajectories calculated for the four different layers discussed above using HYSPLIT and FLEXPART. The HYSPLIT trajectories for the moist aerosol layer near the surface indicate the layer has been descending in the Arctic for the entire simulation, which does not suggest a possible location for the origin of the water vapour. Unlike HYSPLIT, FLEXPART has small residence times over Northern Eurasia and over the Pacific and Atlantic Oceans, indicating these as possible locations of water vapour retrieval.

The dry clear region between 2 km and 3 km shows inconclusive results for the HYS-PLIT simulations. The trajectories from HYSPLIT showed that it could have originated from several different locations in the Pacific Ocean, Canada and across Eurasia. FLEX-PART however only shows footprints over the Pacific Ocean with low residence times. The moist clean layer between 4 and 5 km has HYSPLIT trajectories originating in the Pacific Ocean south of Alaska and matching footprint simulations in the Pacific Ocean from FLEXPART. The dry clean layer between 2 and 3 km has similar FLEXPART footprints to the moist clean layer above, but the residence times are smaller indicating a smaller opportunity to attain water vapour, which could be the reason why the layer is dry.
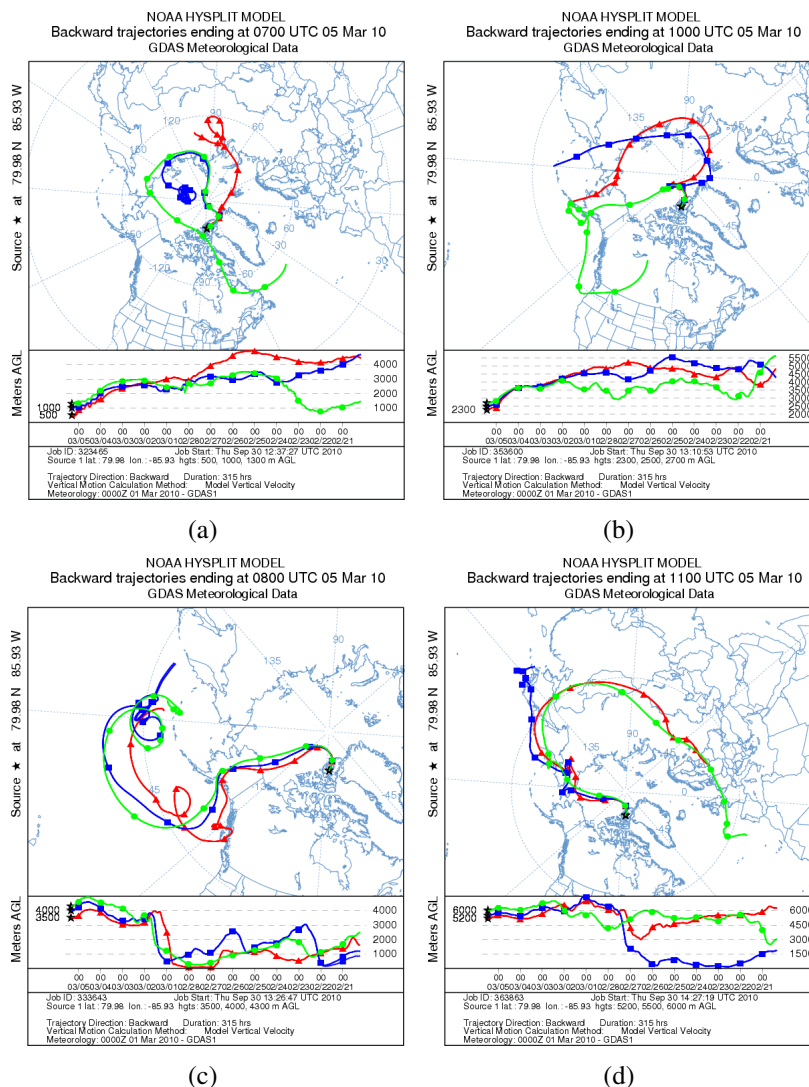
Figure 4.11: HYSPLIT Analyses for March 05, 2010 using HYSPLIT single back trajectories from layers at a) 0-2km, b) 2-3 km, c) 3-5 km, d) 5-6 km. The HYSPLIT backward trajectories are for 13 day simulations.

The dry aerosol layer above 5 km has HYSPLIT trajectories travelling through the Pacific Ocean to Northern Eurasia and Northern Africa and FLEXPART footprint simulations for the layer show large residence times over the same locations. The aerosol was most likely dust from the Sahara desert or anthropogenic pollution from Eurasia. The lack of water vapour in the layer could be explained by the relatively small amount of area covered in the footprint simulations over the Pacific Ocean compared to the coverage over Eurasia and Africa. The dry aerosol layer above 5 km and the moist clean layer between 3 and 5 km show regions of rapid ascent which in the HYSPLIT simulations could be a mechanism

for uplift of water vapour and aerosol in those layers.
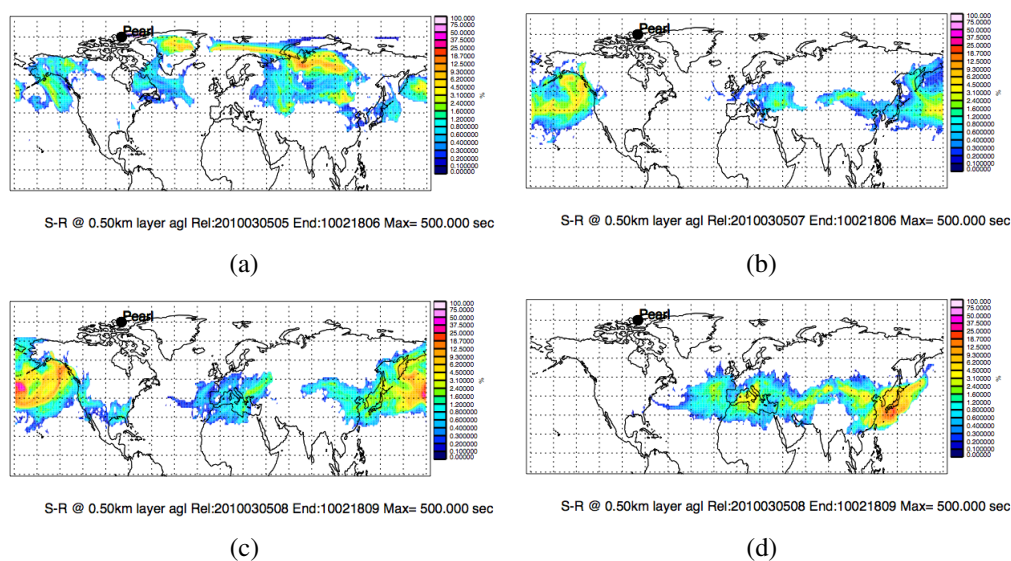


Figure 4.12: FLEXPART Analyses for March 05, 2010 using FLEXPART trajectories from layers at a) 0-2 km, b) 2-3 km, c) 3-5 km, d) 5-6 km. The footprint simulations are 15 day backward simulations. (Credit: Richard Damoah)

## 4.2.4   Discussion

The three measurements described in the previous section all showed a significant number of layers of air masses in the troposphere as shown by $\beta_{aer}(z, \lambda_0)$ and water vapour mixing ratio measurements. The HYSPLIT trajectory and FLEXPART footprint analyses show that the aerosol intrusions originated from significantly different locations from measurement to measurement. The measurements showed that aerosols have originated from Eurasia, Africa and North America. The FLEXPART results indicated the aerosols origin was Eurasia in most layers which would be caused by anthropogenic pollution. The water vapour for the moist aerosol layers was acquired from both the Atlantic and Pacific Oceans in the three cases examined. In most cases FLEXPART accurately determined the possible regions of aerosol and water vapour acquisition. There were a couple of layers in the measurements that had questionable trajectories but this could have been caused by the altitude range chosen for those layers being too close to layers making it difficult for the model to distinguish them.

Moist clean air masses usually attained water vapour from the Pacific Ocean. Air masses that were clean and dry usually had similar trajectories with air masses above or

below them in altitude, but with much smaller residence times near the surface indicating less time to pick up aerosols or water vapour. In layers that had high water vapour mixing ratio or high aerosol concentrations, trajectories usually showed the aerosol or water vapour being acquired when the air mass was near the surface. The cases that had slight amounts of aerosol or water vapour in the layers usually showed trajectories that did not go near surface level.

From HYSPLIT simulations and CRL measurements it was shown that when the air masses entered the Arctic there was a slow decrease in altitude which would be due to the Arctic being a net radiatively cooling environment. The ascent of air usually occurred outside of the Arctic for this reason. Seven day FLEXPART footprint analyses were also produced and they showed little or no residence times near the surface (not shown) which implies ascent occurred earlier, outside of the Arctic.
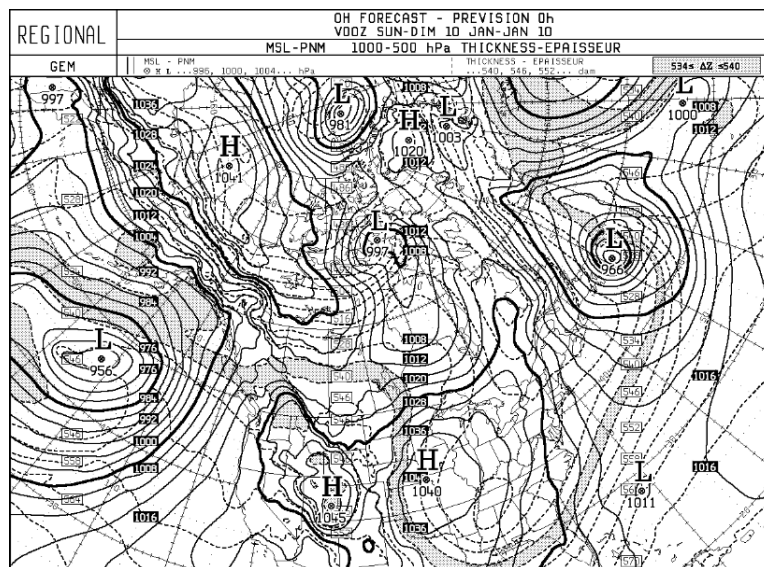


Figure 4.13: Meteorological surface pressure chart for North America on January 10, 2010 at 00:00 UTC. (Image Credit: Environment Canada Weather Office)

One of the possible mechanisms for the uplift of air from lower altitudes near the surface could be due to conveyor belt motion due to low pressures systems (*Grenci and Nese*, 2001) in the vicinity of the trajectories. A number of trajectories shown by HYSPLIT indicated there was rapid ascent for the trajectories shown in Figures 4.9b/c, Figure 4.10b/c/d and Figure 4.11c/d. The trajectories passed through an area of low pressure where there could be either warm or cold conveyor belt motion according to modelled mid-latitude cyclones. Other trajectories show a slow increase in altitude over a number of days. Figure 4.13

shows a meteorological surface pressure chart for January 10, 2010 at 00:00 UTC which matches the time of the rapid ascent shown in Figure 4.9b/c. Trajectories according to HYSPLIT are south of Greenland at this time and are east of the centre of the low pressure system which is where the conveyor belt motion would occur. All trajectories showed the conveyor belt circulation occurring at mid-latitudinal locations.

## 4.3   Sarychev Volcanic Eruption

### 4.3.1   Introduction

The Sarychev Volcano, which is located on Matua Island erupted on June 12, 2009. Matua Island is part of a chain of islands known as the Kuril Islands ($48°N, 153°E$) that are located North East of Japan as seen in Figure 4.14. The Sarychev volcanic activity had a total of nine separate eruptions that lasted until June 15, 2009 (*Levin et al.*, 2010). According to several different reports, the eruption sent ash up to altitudes of 10 km - 16 km (*Mattis et al.*, 2010 and *Levin et al.*, 2010). Figure 4.15 shows an image retrieved by the International Space Station of one of the early ash plumes seen on June 12, 2009.



Figure 4.14: Location of Kuril Islands with respect to Japan and Russia.

Several instruments measured volcanic aerosols, $SO_2$ and other chemical species that travelled to Eureka approximately 2 weeks after the eruption. There were almost continuous stratospheric aerosol measurements by the AHSRL, CRL and Sun photometer until the end of March 2010 where the stratospheric aerosols reached concentrations that were considered background levels.
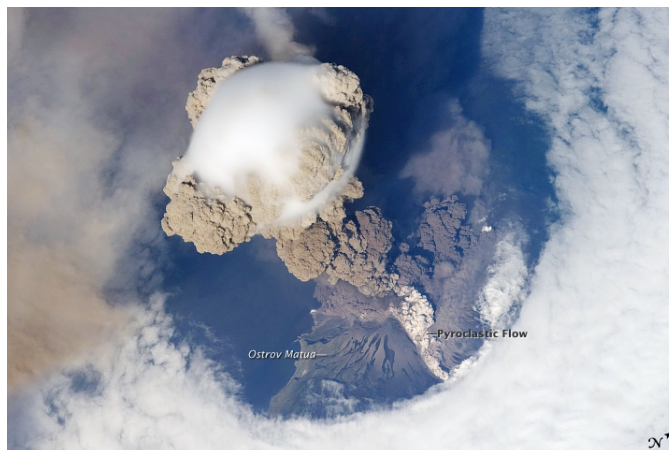
Figure 4.15: Sarychev eruption plume as seen by NASA Earth Observatory on June 12, 2009 during one of the first explosions. The plume in question is composed of brown ash and steam/condensed water which is rising with almost no horizontal motion.(image credit: NASA). The air over the island which is cloud-free due to a circulation created by the plume inhibiting cloud formation in that region.

## 4.3.2   Satellite Measurements

Before the eruption plume reached Eureka on June 24, 2009 as measured by the AHSRL, the plume was tracked by satellite measurements from OMI and CALIOP. OMI measured column measurements of $SO_2$ in the atmosphere, in this case from the surface up to 15 km in altitude.

Daily OMI measurements were composed from the beginning of the eruption showing the initial spread of the $SO_2$ plume up to the time it reached Eureka on July 01 and 02, 2009 as shown in Figure 4.16. On June 13, the plume splits up into two directions, one going east and one west from Matua Island. The plume that originally moved west travelled north of Japan and stayed in that location until June 19 at which time it started to move over north-eastern Russia. After that the $SO_2$ plume moved towards the North Pole and dissipated by June 24, 2009.

The $SO_2$ plume that originally moved east on June 13 crossed the Pacific Ocean and reached Alaska on June 15. The $SO_2$ moved across Alaska and into Canada covering a large area of the country. Starting June 23, the plume slowly dissipated and began to move North until a small filament passed over Greenland which turned around and reached Eureka on July 01. On July 02 the filament of the plume was still over Eureka and left Eureka on July 03 at which time the plume dissipated further with only a small amount of
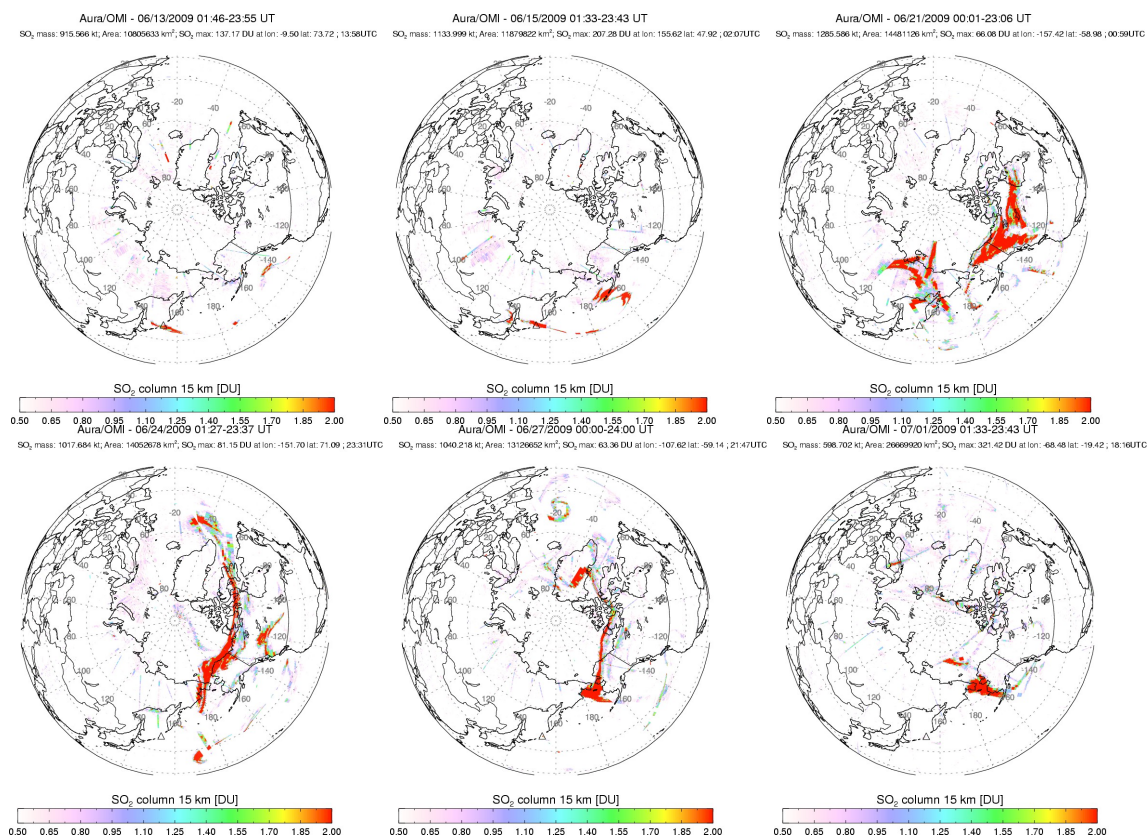
Figure 4.16: OMI Satellite Measurements from June 13, 2009 to July 01, 2009. Composed to daily composite images from the tracks of the OMI satellite for each day in the Northern Hemisphere(image credit: Simon Carn)

SO$_2$ left over Alaska. Preliminary measurements with a UV-VIS spectrophotometer which measured SO$_2$ at Eureka showed an increase in SO$_2$ over Eureka during the same period. The SO$_2$ plume had almost completely dissipated by July 07, by this time it is expected that the SO$_2$ was converted to sulphate because the amount of time that passed since the eruption was only a bit under an e-folding time the 35 days for SO$_2$ in the stratosphere (*Bluth et al.*, 1997).

Measurements from CALIOP over Eureka on June 25 show stratospheric aerosols which were likely from the Sarychev eruption as shown in Figure 4.17. There was also stratospheric aerosol throughout the track of CALIOP showing how the aerosol spread throughout the Arctic by this time. The dates at which the aerosol arrived over Eureka are significantly different according to each instrument. A reason for this could be that OMI only measures SO$_2$ so aerosol that was either converted from SO$_2$ by chemical reactions or was originally ash from the eruption could have reached Eureka earlier and OMI would not

have been able to measure it. OMI may not have been sensitive enough either if the amount of $SO_2$ was too small.
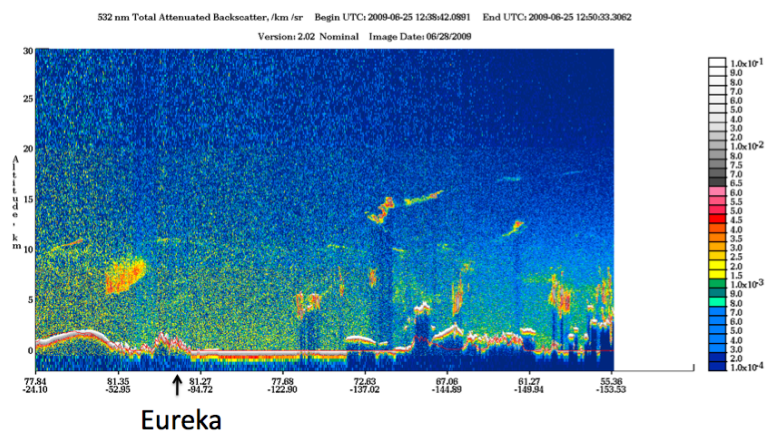


(a)
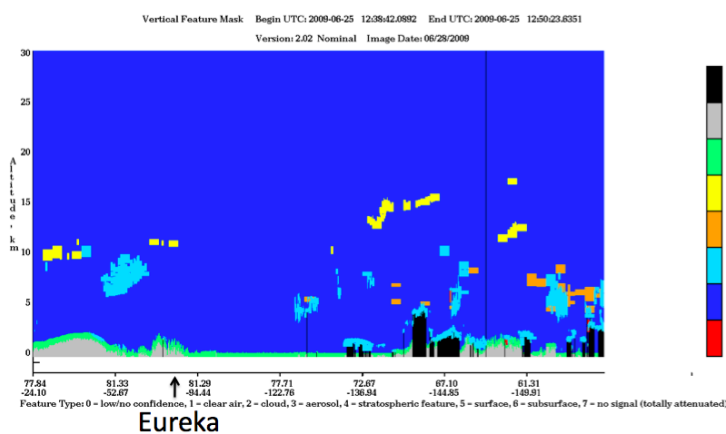


(b)
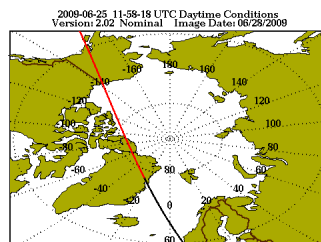


(c)

Figure 4.17: CALIPSO satellite measurements that cross over Eureka, Nunavut on June 25, 2009. Small amounts of stratospheric aerosol are measured by the space borne instrument above areas near Eureka. The following images show a) the aerosol volume backscatter cross section measured by the CALIOP instrument, b) the type of particle measured in the aerosol volume backscatter cross section images, c) and the track covered from the beginning to the end of the plot showing a near overpass of Eureka, Nunavut which is labelled in the figures.

## 4.3.3   Initial Measurements

The first measurement of the volcanic aerosol retrieved at Eureka was by the AHSRL between the days of June 24 and June 26, 2009 as shown in Figure 4.18 which match the CALIOP measurements in Figure 4.17. AHSRL measurements shown in the following sections are calculated by using a vertical resolution of 35 metres and a temporal resolution of 3 minutes. The aerosol, which is likely from the Sarychev eruption is split up into two regions during the measurement. The first region would be between approximately 6:00 and 12:00 UTC on June 24 and between 6 km and 8 km, which is located in the troposphere. The second region in the measurement, which begins at 00:00 UTC on June 25 and continues until the end of the measurement, has an altitude range of 8 km and 11 km, which is a mixture of tropospheric and stratospheric aerosols.
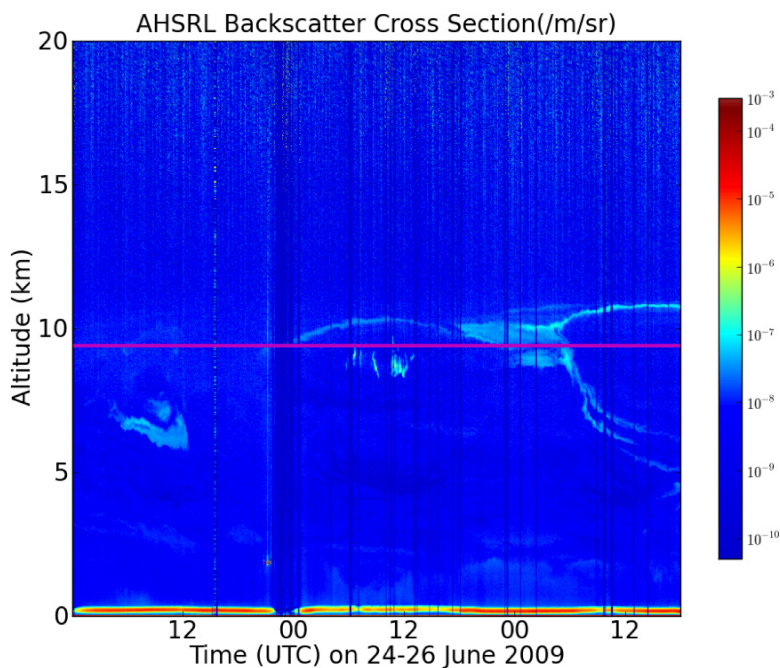


Figure 4.18: AHSRL measurement time series of $\beta_{\mathrm{aer}}(z, \lambda_0)$ from June 24-26, 2009 showing the first measurement of aerosols from the Sarychev eruption. The magenta line represents the tropopause during the measurement.

There was a small amount of aerosol in the lower stratosphere between 10 km and 11 km which was likely from the Sarychev eruption. The largest aerosol concentration over Eureka due to the Sarychev eruption was measured on July 1, 2009, which can be seen in Figure 4.19. There was volcanic aerosol between the altitudes of 10 and 14 km starting

on July 01 at 06:00 UTC and this measurement coincides with the date the OMI measurements showed $SO_2$ over Eureka. After this measurement the AHSRL measurements showed varying amounts of aerosol until approximately July 09, 2009. At this time the AHSRL started measuring aerosol consistently in the stratosphere which likely means the aerosol was horizontally mixed in the stratosphere. The AHSRL was measuring $\beta_{aer}(z, \lambda_0)$ until August 19, 2009 which is when the AHSRL laser failed.
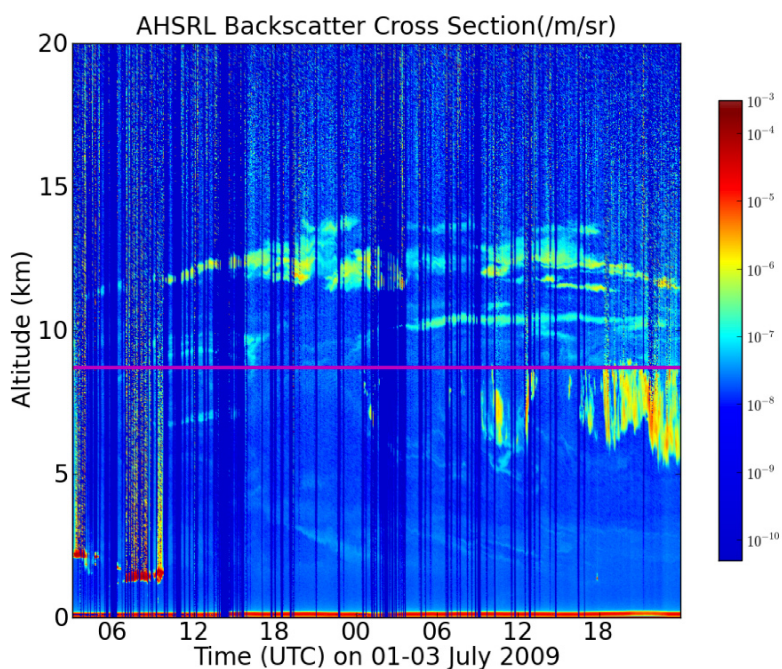


Figure 4.19: AHSRL measurement time series of $\beta_{aer}(z, \lambda_0)$ from July 01-03, 2009 showing the largest $\beta_{aer}(z, \lambda_0)$ values seen in the stratosphere due to the Sarychev eruption. This measurements corresponds with the first measurement of $SO_2$ over Eureka by OMI. The magenta line represents the tropopause during the measurement.
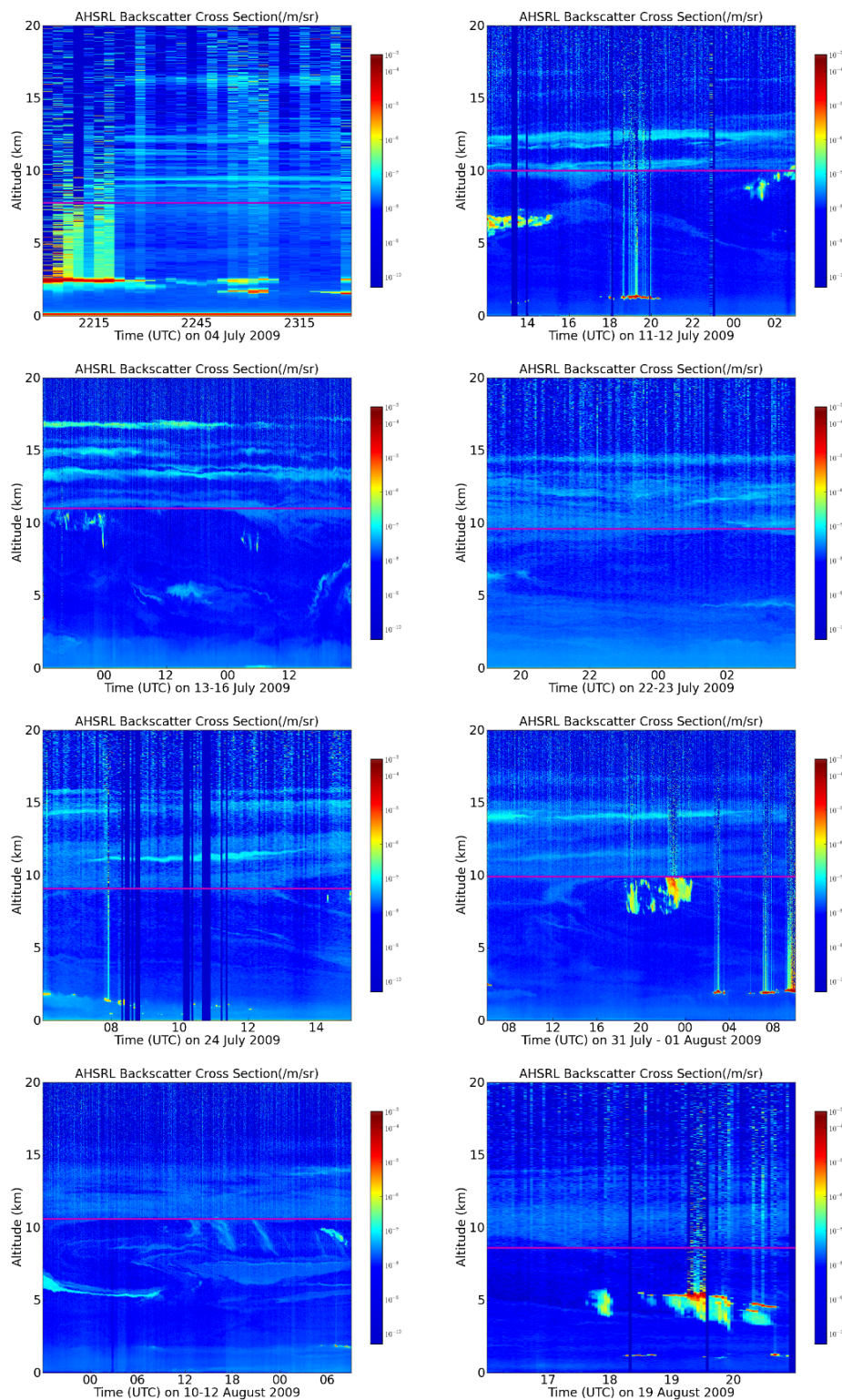
Figure 4.20: AHSRL measurements time series of $\beta_{aer}(z, \lambda_0)$ from the beginning of July, 2009 to the middle of August 2009 showing stratospheric aerosol layers up to 17 km in early measurements. Later into this set of measurements the aerosol vertically mixes and only reaches up to approximately 15 km in altitude on August 19, 2009. The magenta line represents the tropopause during the measurement.

Figure 4.20 shows several measurements from the AHSRL occurring between July 04, 2009 and August 19, 2009. The measurements from July of 2009 show lots of structure in the stratospheric measurements having several layers of aerosol up to altitudes of 17 km. Later measurements in July 2009 show diminished structure and a decrease in altitude of the aerosol. Measurements in August of 2009 show a large decrease in structure of the aerosol in the stratosphere due to vertical mixing of the aerosol layers. At this time the number of layers of aerosol have decreased to two prominent layers that have almost merged together to create an even distribution of aerosol that reaches an altitude of approximately 15 km according to Figure 4.20.

### 4.3.4  CRL Measurements

On August 19, 2009, the AHSRL laser failed which stopped data retrieval but on August 29, 2009, the CRL started collecting data periodically to test the automatic alignment program. There was a total of six measurements during the months of August, September and October that could be used for analysis of the Sarychev eruption as shown in Figure 4.21.
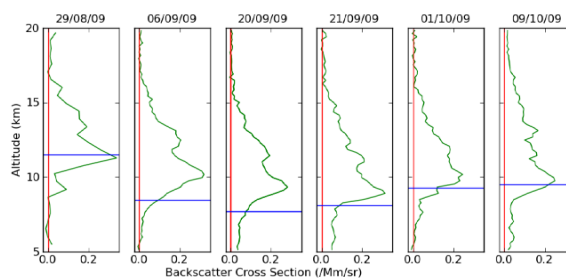


Figure 4.21: CRL Fall Measurements for summed profiles in the lower stratosphere of $\beta_{aer}(z, \lambda_0)$ covering dates in August, September, and October of 2009. The blue line represents the tropopause altitude according to radiosonde temperature profiles

Figure 4.21 shows measurements that had high $\beta_{aer}(z, \lambda_0)$ in the lower stratosphere. The measurements shown in the figure are summed profiles of the entire measurement taken on each particular day to reduce noise in the lidar measurements at stratospheric altitudes. The vertical resolution of the profiles are 200 metres to reduce noise as well. The blue horizontal line at varying altitudes represents the height of the tropopause during that measurement. The tropopause height was determined using temperature profiles from radiosondes. The measurements by the CRL show little structure as compared to measurements by the AHSRL in July. The CRL measurements up to September 06, 2009 showed two layer structure

as seen in August of 2009 by the AHSRL. After that measurement the second layer mixed into the lower layer of aerosol in future measurements. The Klett inversion had to be used for Figure 4.21 because the nitrogen Raman channel was saturated with background photon counts due to incoming solar radiation during that time of year.
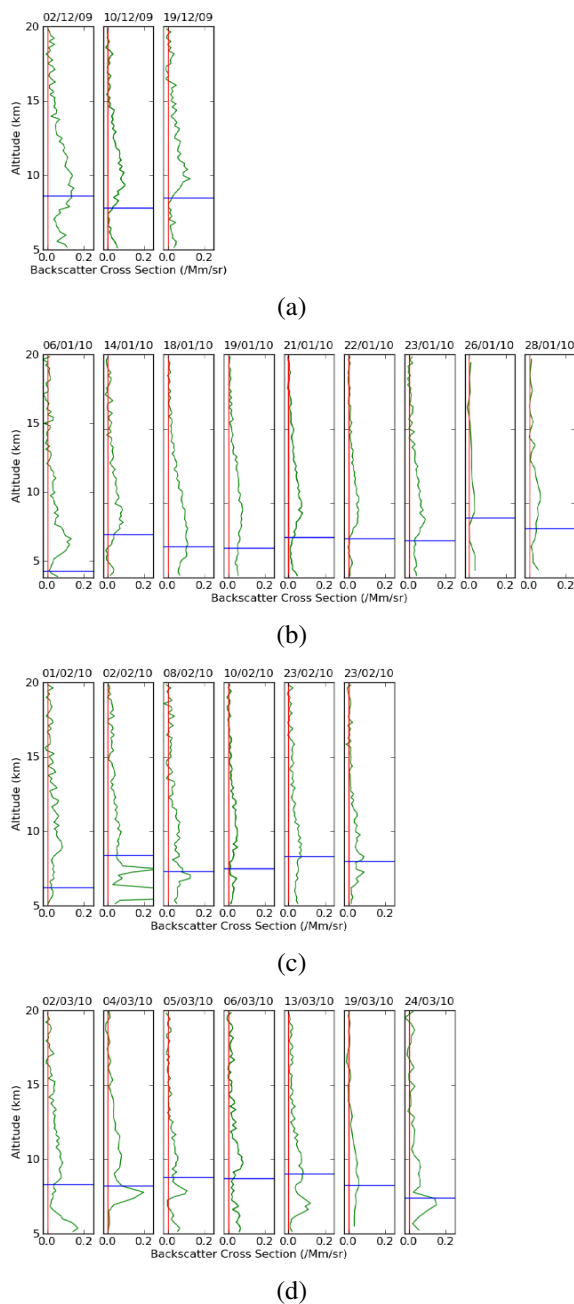


Figure 4.22: CRL Winter 2010 measurement summed profiles in the lower stratosphere for $\beta_{\mathrm{aer}}(z, \lambda_0)$ with dates indicating the date the measurement started. The blue line represents the tropopause altitude according to radiosonde temperature profiles

During the month of November there were no measurements that could be used for analysis from the CRL or the AHSRL. During the month of December there were three measurements from the CRL that could be used, which were originally obtained for preparation of the winter 2010 measurement campaign. These measurements along with campaign measurements shown in Figure 4.22 show decreased $\beta_{\text{aer}}(z, \lambda_0)$ in the stratosphere when compared to values taken in the previous months due to the volcanic aerosol diminishing over time. There were several instances in the CRL profiles that showed high $\beta_{\text{aer}}(z, \lambda_0)$ below the tropopause but these are only due to detection of clouds or tropospheric aerosols that are not from the Sarychev eruption. In February 2010 $\beta_{\text{aer}}(z, \lambda_0)$ reached aerosol concentrations that were similar to values before the eruption.

The measurements shown in Figure 4.22 are absolutely calibrated using the Ratio inversion, which is a more confident retrieval technique than using a single wavelength inversion. The measurements are calibrated at approximately 20 km or higher which is featureless and clear of aerosols and there are no signs of the $\beta_{\text{aer}}(z, \lambda_0)$ going to values less than zero at any altitude, giving more confidence in the retrievals.

### 4.3.5    Stratospheric Aerosol during 2009/2010

The amount of aerosol in the stratosphere above Eureka was tracked over time by using a combination of AHSRL, CRL, CALIOP, and sun photometer measurements. This was done by calculating the integrated $\beta_{\text{aer}}(z, \lambda_0)$ for the lower stratosphere for each measurement by each instrument before and after the Sarychev eruption. The altitude range used for the calculation started from the tropopause height up to 18 km, which was above the highest altitude that aerosol was seen for all measurements. Figure 4.23 is a plot of the integrated $\beta_{\text{aer}}(z, \lambda_0)$ over time starting from February 2009 (pre-eruption) to March 2010 (10 months after the eruption).

The sun photometer measurements were originally in units of aerosol optical depth for the entire atmosphere. An average background optical depth for the aerosol in the troposphere was determined using measurements prior to the plume's arrival assuming small daily variations in the tropospheric aerosol. The average background optical depth was then subtracted from the total optical depth to get the stratospheric optical depth. The stratospheric optical depth was then converted to integrated $\beta_{\text{aer}}(z, \lambda_0)$ by dividing the stratospheric optical depth by a lidar ratio for sulphate aerosols of 71 sr (*Cattrall et al.*, 2005).

According to Figure 4.23, the integrated backscatter cross section from the AHSRL and sun photometer reasonably match, indicating a correct choice for the lidar ratio.

The measurements between February and June 2009 represent background conditions for the stratosphere before the Sarychev eruption with an integrated backscatter of approximately 0.0003 sr$^{-1}$. The background conditions go back as far as February 2009 to show that the Redoubt eruption from the end of March 2009 did not inject aerosols in the stratosphere over Eureka.
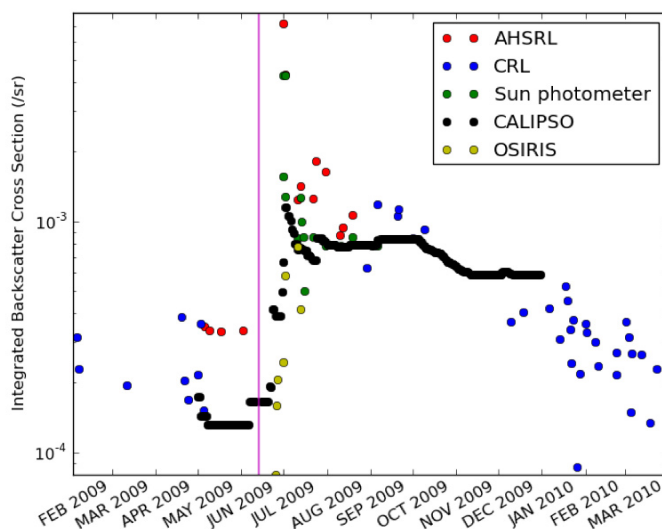


Figure 4.23: Integrated $\beta_{aer}(z, \lambda_0)$ for stratospheric aerosol measurements from February of 2009 to March of 2010 using AHSRL, CRL, and converted sun photometer measurements. The altitude range chosen for the AHSRL and CRL integrated $\beta_{aer}(z, \lambda_0)$ was between the tropopause and 16 km. Using the tropopause as the minimum makes sure that there is no stratospheric aerosol left out in the altitude range chosen.

The beginning of July are the first stratospheric aerosol measurements for the eruption which showed a large increase in the integrated $\beta_{aer}(z, \lambda_0)$ to values as high as 0.005 sr$^{-1}$ to 0.007 sr$^{-1}$. After approximately a week the integrated $\beta_{aer}(z, \lambda_0)$ diminished to values between 0.001 sr$^{-1}$ and 0.0015 sr$^{-1}$ which decreased slowly with time as shown in Figure 4.23. The larger integrated $\beta_{aer}(z, \lambda_0)$ were from before the aerosol horizontally mixed in the stratosphere.

The AHSRL, CRL, CALIOP, and sun photometer measurements correspond well during the transition from AHSRL to CRL measurements in August of 2009, where all instruments measure approximately 0.001 sr$^{-1}$ for the integrated $\beta_{aer}(z, \lambda_0)$. The decrease of the

integrated $\beta_{\mathrm{aer}}(z, \lambda_0)$ continued until the end of February, 2010 which is when it returned to background conditions as seen before the eruption. The likely reason for the decrease of the integrated $\beta_{\mathrm{aer}}(z, \lambda_0)$ with time is because of aerosols being exchanged between the stratosphere and troposphere (*Duck and Whiteway*, 2005 and *Holton et al.*, 1995 and *Dreshler*, 2008). According to the profile measurements by the CRL in Figure 4.21 and Figure 4.22, the volcanic aerosol starts near the tropopause for all measurements and shows that most of the aerosol is located in the first couple of kilometres above the tropopause.

Figure 4.24 shows the height of the tropopause compared to the altitude of maximum aerosol concentration (hereafter referred to as 'plume altitude') above the tropopause after the aerosols reached Eureka as measured by the AHSRL and CRL. The altitudes for the plume altitude were chosen by visual inspection of each individual profile from the AHSRL and CRL. At the beginning of the eruption when there were multiple layers of aerosol, multiple plume altitudes were chosen for each measurement due to the number of different layers of aerosol in the stratosphere. In July 2009 some of the layers were up to an altitude of approximately 18 km. The number of layers decreased to two layers by August 2009 and in September 2009 there was only one uniform layer of aerosol in the stratosphere. The altitude of the aerosol layer after the vertical mixing was complete is close to the tropopause altitude. The plume altitude of the aerosol when there were multiple aerosol layers also show that the lowest aerosol layer was near the tropopause as well. The aerosol therefore ranged from approximately 10 km (tropopause height) to 18 km in July 2009, which is a large vertical span. The dynamical process causing the plume altitude to be close to the tropopause is unknown and is still being investigated. Figure 4.24 also shows the span of the aerosol over time as indicated by the grey shaded region. This shows that the top of the aerosol layer was on average around 16 km for the set of measurements.

After the aerosol is homogeneously mixed vertically, it is hard to determine if there is any trend seen for the plume altitude unlike discussed in *Bitar et al.* (2010). In *Bitar et al.* (2010) the plume altitude from the Kasatochi eruption dropped at the same rate as the tropopause height. The tropopause decreases with height as the temperatures drop in the atmosphere due to radiative cooling during the transition to the winter season but there is no distinct pattern seen in the CRL and AHSRL plume altitudes. After the vertical mixing of the multiple layers of aerosol was complete at the end of August 2009 there were only a few measurements that were possible to use between the months of September and

December, which makes it difficult to conceive a pattern. During February the tropopause began to increase in height because of solar sunrise which increased the temperatures in the atmosphere during the transition to the summer season, which makes it more difficult to determine a pattern between the plume altitude and the tropopause heights. In most cases the aerosol was fairly close to the tropopause. The plume altitude was located within a kilometre of the tropopause, as shown in Figure 4.24 and Figures 4.21 and Figure 4.22. In the measurements from February and March 2010, the plume altitude was usually a couple of kilometres away from the tropopause. This could be due to the fact that the aerosol had returned to background conditions for the stratosphere.
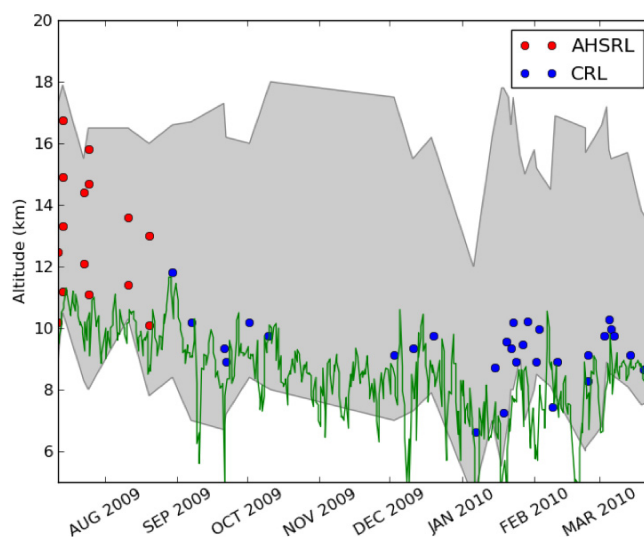


Figure 4.24: Comparison of tropopause altitude to plume altitude from July 2009 to March 2010. This was computed by using a mixture of AHSRL (red points) and CRL (blue points) data over the corresponding months and using radiosonde measurements for the tropopause altitude (green line). The grey shaded region is where the altitude range the aerosol encompassed during the measurements.

## 4.4 Summary

Three cases of water vapour and aerosol intrusions in the troposphere were examined using HYSPLIT and FLEXPART simulations. Water vapour in most cases were acquired from the Atlantic and Pacific Oceans. Aerosols usually were acquired from Eurasia with one case showing possible acquisition in North America (USA). Dry clean layers usually had

back trajectories similar to layers located above or below them. This could have been due to mixtures of layers by the model due to the altitude ranges chosen for those layers. The significant difference between the two would be the smaller residence times spent near the surface for the dry clear region as compared to the other air masses nearby.

Uplift of water vapour and aerosol, according to HYSPLIT was achieved by either slow ascent over several days or rapid ascent over several hours. Rapid ascent of air masses from the surface are due to conveyor belt circulation in low pressure systems at the location of uplift. This was shown by the comparison of meteorological charts and HYSPLIT simulations ascent regions. In most cases the rapid ascent occurred outside the Arctic in mid-latitude locations.

Aerosol measurements from several ground and satellite based instruments tracked the Sarychev aerosol plume that erupted between June 2009 and March 2010. Before the eruption, the CRL, AHSRL, and CALIOP measurements showed small amounts of background aerosol in the lower stratosphere which had an integrated backscatter cross section of approximately 0.0003 sr$^{-1}$. At the end of June 2009, the integrated $\beta_{aer}(z, \lambda_0)$ began to increase in the lower stratosphere due to aerosols entering the region and maximized the integrated $\beta_{aer}(z, \lambda_0)$ on July 1 and July 2 of 2009, which coincided with the arrival of SO$_2$ over Eureka. In mid July, the aerosols horizontally mixed in the stratosphere and began to decrease slowly over time during the following months due to processes of stratospheric/tropospheric exchange. By the end of February, 2010 the aerosol concentrations were back to background conditions as measured before the eruption.

In July, 2009 the aerosol had a lot of vertical structure showing several layers of aerosol ranging from the tropopause to 18 km in altitude. As time passed the aerosol mixed vertically, decreasing the vertical structure until the aerosol was a single layer with a plume altitude near the tropopause. The plume altitude consistently stayed near the tropopause until the winter months of 2010 where it began to increase, which was likely due to the transition back to background conditions in the stratosphere.

# CHAPTER 5

## PARTICLE ANALYSIS

This chapter describes calculations of the lidar ratio and colour ratio for aerosols and clouds. Both of these quantities can give insight on the size and type of scatterer in the measurement region. The lidar ratio calculations can be used as input into the Klett and Coffin inversions. The colour ratio can be further used to estimate particle effective radii.

## 5.1 Lidar Ratio Methodology

The lidar ratio or extinction-to-backscatter ratio is needed to calculate the $\alpha_{\mathrm{aer}}(z, \lambda_0)$ or $\beta_{\mathrm{aer}}(z, \lambda_0)$ to use the Klett and Coffin inversions. As stated in Section 2.1.6 the lidar ratio is dependent on several properties of the scatterer such as its altitude, size, shape, and chemical composition. The lidar ratio needs to be calculated using the $\alpha_{\mathrm{aer}}(z, \lambda_0)$ and $\beta_{\mathrm{aer}}(z, \lambda_0)$ from independent sources to get accurate values as shown in Equation 2.13. It is important to have the correct lidar ratio so the most accurate value of $\alpha_{\mathrm{aer}}(z, \lambda_0)$ can be used for calculations of aerosol and cloud optical depths. These values can be used in radiative transfer modelling to determine the aerosol climate effects (*Chen et al.*, 2002 and *Pappalardo et al.*, 2004).

Besides using the lidar ratio for the calculation of $\alpha_{\mathrm{aer}}(z, \lambda_0)$ or $\beta_{\mathrm{aer}}(z, \lambda_0)$ in the Klett and Coffin inversions it can also be used to determine particle properties. The lidar ratio can be used to help determine the type of particle. Particles with large lidar ratios indicate small and/or absorbing aerosols while smaller lidar ratios indicate the larger and/or less absorbing particles. The lidar ratio can also be helpful in determining origins of particles. If the particle type can be determined from the lidar ratio, then the number of sources for the particles can be narrowed down (*Franke et al.*, 2001).

From the CRL measurements, the lidar ratio can be calculated for both the 532 nm and 355 nm wavelengths. The two inversions used to calculate $\alpha_{\text{aer}}(z, \lambda_0)$ and $\beta_{\text{aer}}(z, \lambda_0)$ are the Raman and ratio inversion. The first independent source, the Raman inversion, is used to calculate the $\alpha_{\text{aer}}(z, \lambda_0)$ because it does not use the lidar ratio in the calculation of its value for the aerosol extinction coefficient. The second independent source, the ratio inversion, is used to calculate the $\beta_{\text{aer}}(z, \lambda_0)$ in the lidar ratio. Similar to the Raman inversion, the ratio inversion has no assumption for the lidar ratio unlike the Coffin or Klett inversions.

## 5.2   Colour Ratio Methodology

The CRL transmits at two different wavelengths, 355 nm and 532 nm, for the purpose of retrieving $\beta_{\text{aer}}(z, \lambda_0)$ at two different sets of scattering wavelengths. Using the set of $\beta_{\text{aer}}(z, \lambda_0)$ calculations, the size of aerosol or cloud particles can be estimated through use of a scattering model. Estimates of particle sizes are important for use in radiative transfer models.

The colour ratio is a ratio of a set of $\beta_{\text{aer}}(z, \lambda_0)$ at two different wavelengths,

$$C_{\text{ratio}} = \frac{\beta_{\text{aer}}(z, \lambda_1)}{\beta_{\text{aer}}(z, \lambda_2)}, \tag{5.1}$$

where $C_{\text{ratio}}$ is the colour ratio, and $\beta_{\text{aer}}(z, \lambda_1)$ and $\beta_{\text{aer}}(z, \lambda_2)$ are the volume backscatter cross sections at each wavelength. The colour ratio creates a quantity that does not contain a particle number term and is therefore related to only the particles physical quantities,

$$C_{\text{ratio}} = \frac{\beta_{\text{aer}}(z, \lambda_1)}{\beta_{\text{aer}}(z, \lambda_2)} = \frac{n \frac{d\bar{\sigma}_{\text{sca}}(\pi, \lambda_1)}{d\Omega}}{n \frac{d\bar{\sigma}_{\text{sca}}(\pi, \lambda_2)}{d\Omega}} = \frac{\frac{d\bar{\sigma}_{\text{sca}}(\pi, \lambda_1)}{d\Omega}}{\frac{d\bar{\sigma}_{\text{sca}}(\pi, \lambda_2)}{d\Omega}}, \tag{5.2}$$

where $\frac{d\bar{\sigma}_{\text{sca}}(\pi, \lambda_1)}{d\Omega}$ and $\frac{d\bar{\sigma}_{\text{sca}}(\pi, \lambda_2)}{d\Omega}$ are the average differential scattering cross sections due to a distribution of particles of varying sizes. CALIOP uses the colour ratio technique to distinguish between different types of particles, such as clouds or aerosols to help determine the appropriate lidar ratio to calculate optical properties, for that scatterer (*Liu et al.*, 2007). Mie scattering theory can also be used to calculate scattering efficiencies for different types of particles by using their refractive index and effective radii (*Mishchenko et al.*, 2002). Equation 2.2 shows how the particle scattering cross section is related to the scattering efficiency of a particle and the same is applied for the backscattering efficiencies and

differential scattering cross sections,

$$\bar{Q}_{\rm sc}(\pi,\lambda) = \frac{d\bar{\sigma}_{\rm sc}(\pi,\lambda)}{d\Omega}\frac{1}{\pi r_{\rm eff}^2} \tag{5.3}$$

where $\bar{Q}_{\rm sc}(\pi,\lambda)$ is the average backscattering efficiency due to a size distribution of particles with an effective radius, $r_{\rm eff}$. Rearranging for the differential cross section and taking the ratio of two differential cross sections at different wavelengths gives a direct relation for the colour ratio and the ratio of backscattering efficiencies calculated from Mie theory,

$$C_{\rm ratio} = \frac{\beta_{\rm aer}(z,\lambda_1)}{\beta_{\rm aer}(z,\lambda_2)} = \frac{\frac{d\bar{\sigma}_{\rm sca}(\pi,\lambda_1)}{d\Omega}}{\frac{d\bar{\sigma}_{\rm sca}(\pi,\lambda_2)}{d\Omega}} = \frac{\bar{Q}_{\rm sc}(\pi,\lambda_1)}{\bar{Q}_{\rm sc}(\pi,\lambda_2)}. \tag{5.4}$$

Using this relation the effective radii of particles can be estimated from the ratio of the backscattering efficiencies. Results for the colour ratio were calculated using the ratio inversion at 355 nm and 532 nm. The MMCR (8.6 mm) is used as well to compare to the 532 nm channel of the CRL creating a second colour ratio.

## 5.3   Mie Scattering Simulations

Mie Scattering code written by *Mishchenko et al.* (2002) was used to simulate scattering efficiencies for ice and aerosol distributions for the purpose of retrieving effective radii of particles measured. The shape of particles assumed for the simulation is spherical due to the difficulty in determining actual particle shapes. For ice particles, gamma and power law distributions were used for the calculations with distributions that had effective variances of 0.1 and 0.3. The size range chosen for the Mie simulations were between 1 and 300 microns. Figure 5.1 shows a plot with four types of distributions, two gamma and two power law, each with variances of 0.1 and 0.3. Due to the large particle sizes, the fact that ice are scattered in the Mie/geometric optic scattering regime, and the close proximity of the 532 nm and 355 nm wavelengths, the colour ratio does not vary significantly away from 1. At most it is approximately 20% away from 1 for the simulations. The oscillating pattern makes it difficult to retrieve particle radii for ice nuclei since a value for the colour ratio was often at several different size ranges. Mie simulations from *Bourdages et al.* (2009) show significantly different results with several orders of magnitude change in the colour ratio for the same particle radii change using the MMCR wavelength (8.6 mm) and 532

nm.



Figure 5.1: Mie scattering code calculations comparing colour ratio of 532 nm and 355 nm with the effective radius of ice particles between 1 and 300 microns.

The differences in the two colour ratios are due to the differences in the wavelengths. The 532 nm and 355 nm wavelengths are relatively close to each other so the difference in the scattering efficiency of the two wavelengths will be much smaller compared to the MMCR (8.6 mm) and 532 nm. The 8.6 mm-532 nm colour ratio increases with decreasing altitude while the 532-355 nm colour ratio only has a slight change near the bottom of the cloud due to different scattering efficiencies at each wavelength. Cloud particle sizes measured by the MMCR are located in the Rayleigh scattering regime which gives a large variation in the scattering efficiency with small changes in the size (See Section 2.1.1). This also explains why the colour ratio for the MMCR set of wavelengths is much smaller since the scattering efficiency is much lower in the Rayleigh scattering regime than the Mie scattering regime. The CRL wavelengths however have clouds in the Mie scattering regime where the scattering efficiency does not vary as much with changes in ice cloud particle size.

Mie simulations used for aerosols have significantly different results than for ice particles. The size range chosen was between 0.01 microns and 10 microns because aerosols are smaller than ice particles. Instead of a gamma or power law distribution, a log-normal distribution was chosen for the aerosols which has been shown to be one of the most accurate
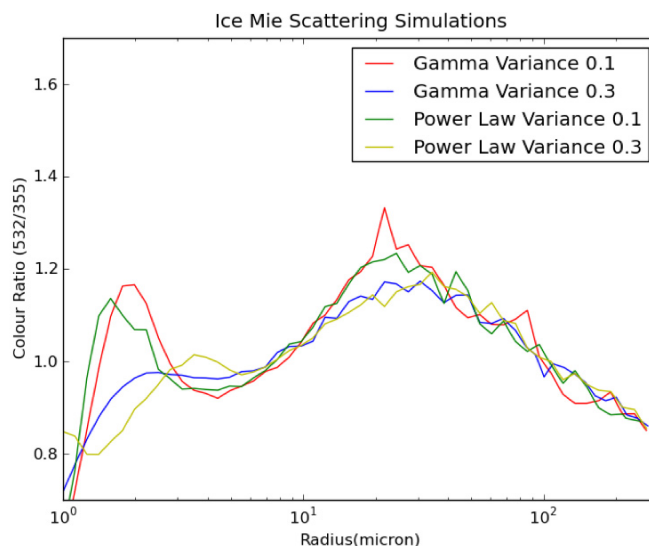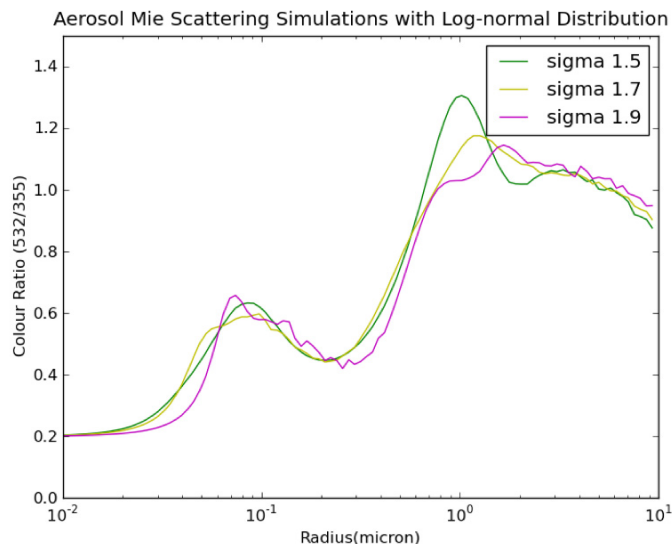
Figure 5.2: Mie scattering code calculations comparing colour ratio of 532 nm and 355 nm with the effective radius of aerosol particles between 0.01 and 10 microns.

fit for aerosol distributions (*O'Neill et al.*, 2000). The Mie simulations are only calculated for the CRL colour ratio wavelengths because the MMCR is not able to detect particles as small as aerosols. Figure 5.2 shows the Mie results for different shaped log-normal distributions and the results show two different values of colour ratio for two sets of effective radii ranges. Colour ratios with values between 0.2 and 0.6 are in a size range of 0.05 and 0.5 microns.

Mie simulations were also used to compare lidar ratio to the size of the ice particles for the 532 nm and 355 nm wavelengths. The simulations were done using a gamma distribution with a variance of 0.2 as in the colour ratio Mie calculations for ice particles. The assumption of spherical particles is also used for the ice particle simulations. Figure 5.3 shows the simulations for both wavelengths which are very similar to each other but offset by a few microns. For particles less than 1 micron, the lidar ratio increases to over 80 sr while particles greater than that size are between 20 sr and 30 sr. *Mishchenko et al.*, 2002 showed similar results with backscatter to extinction ratios where spherical particles were also assumed.
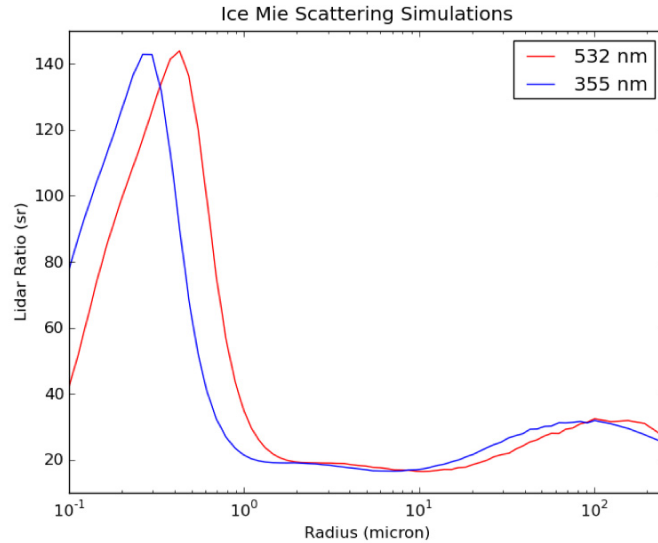
Figure 5.3: Mie scattering code calculations for lidar ratio with the effective radius for ice particles between 0.1 and 250 microns.

## 5.4 Lidar Ratio Results

The following section will discuss calculated lidar ratios for ice clouds and aerosols during the winter 2010 campaign from the CRL. During the campaign there have been several occurrences of ice clouds in Eureka. Due to the extremely cold conditions in Eureka at this time of year there are usually no water clouds at these latitudes.

Figure 5.4 shows a measurement of the $\beta_{\text{aer}}(z, \lambda_0)$ from January 06, 2010 of an ice cloud ranging from 1 km to 5 km for the 532 nm and 355 nm wavelengths of the CRL. The plot is cut off at 2.5 km because it is in the incomplete overlap region for the Raman inversion. The cloud has an optical depth of approximately 1 during this section of the measurement. Figure 5.4 also shows time series calculations for the lidar ratio, for the 532 nm and 355 nm wavelengths. Throughout most of the cloud in both wavelengths the lidar ratio is between 10 sr and 30 sr. The edges of the cloud show an increase of the lidar ratio up to values of 80 sr or higher.
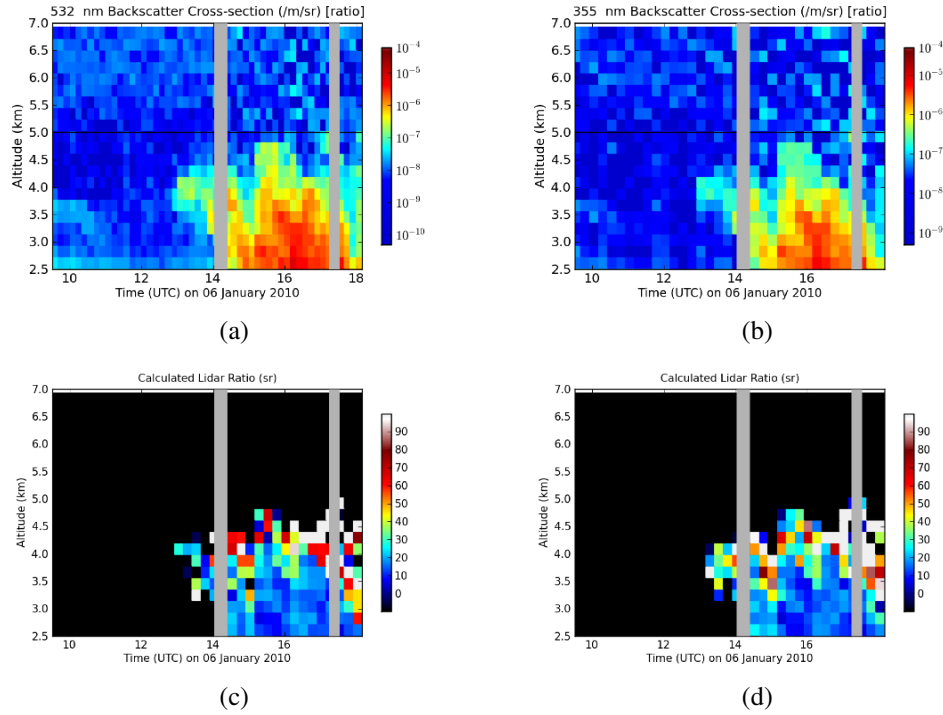
Figure 5.4: $\beta_{\mathrm{aer}}(z, \lambda_0)$ retrievals at a) 532 nm and b) 355 nm and lidar ratio calculations for January 06, 2010 at c) 532 nm d) 355 nm

Figure 5.5 shows the lidar ratio calculations from summed profiles of the same measurement in Figure 5.4. The profiles of the lidar ratio show that for both sets of wavelengths, the lidar ratio increases near the top of the cloud. This could be due to changes in the particle properties within the cloud. Throughout the centre of the cloud the lidar ratios are both approximately 15 sr. There is not a significant difference between the two wavelengths except for the top of the cloud. The top of the cloud shows an increase of the lidar ratio to approximately 40 sr for 532 nm and 60 sr for 355 nm similar to the lidar ratios calculated in Figure 5.4.

Figure 5.6 shows several other measurements during the winter 2010 campaign which have been used for lidar ratio calculations. All measurements are cut off at 2.5 km for both wavelengths where above 2.5 km is an overlap corrected region for the Raman inversion using the clear air method described in Section 2.1.5. Due to changes of the overlap region in the bottom 2.5 km for each measurement, the calculations are ignored until an improved overlap correction can be produced. Most measurements show lidar ratio calculations ranging from 10 sr to 30 sr for the measurement campaign at both wavelengths. Also, as in the measurement from January 06, 2010, the top of the clouds have regions where the lidar
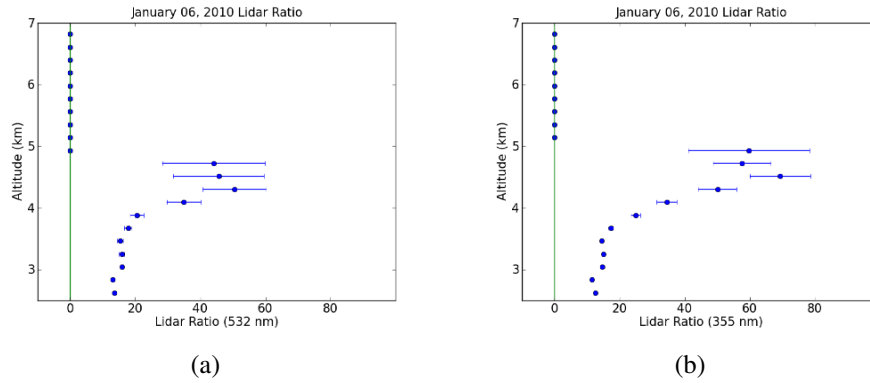
Figure 5.5: $\beta_{aer}(z, \lambda_0)$ calculations along with lidar ratio calculations for January 06, 2010 at a) 532 nm b) 355 nm profiles. Profiles are calculated from measurements between 14:00 UTC on January 06, 2010 to 18:10 UTC on January 06, 2010.

ratio increases to values higher than 30 sr for both 355 nm and 532 nm. This is also seen at regions near other the edges of the cloud for the cases in Figure 5.6.

Other measurements show lidar ratios calculated using a Raman lidar transmitting at 355 nm for cirrus clouds which have lidar ratios of approximately 100 sr near the top of clouds (*Petty et al.*, 2006) which is a matching feature with some calculated lidar ratio measurements from the CRL. This may be explained by properties of the cloud particles being different near the top of the cloud than at other regions, such as changes in the size of the particles. Figure 5.3 shows that for small ice particles the lidar ratio can increase significantly for particles that are less than 1 micron in radii. This is most likely not the case for why the lidar ratio is increasing significantly because it increases near the bottom edges of clouds as well. A possible cause for this could be the derivative in the Raman inversion technique. The derivative uses two points in the adjacent vertical bins to determine the slope which is not necessarily correct for regions near the edge of a cloud due to sudden changes in the backscatter. In most cases the extinction would be overestimated due to this problem, thereby increasing the lidar ratio.

Other Raman lidar systems using the same technique to calculate the lidar ratio for cirrus clouds retrieve higher lidar ratios. For the 355 nm wavelength, the value of the lidar ratio according to another Raman lidar for cirrus cloud particles is between 30 sr and 40 sr (*Giannakaki et al.*, 2007 and *Reichardt*, 1998). For the 532 nm wavelength, the lidar ratio for cirrus cloud particles have been calculated to be between 30 sr and 35 sr (*Chen et al.*, 2002), but this calculation used a different method than what has been done for the CRL

measurements. Also, *Ansmann et al.* (1992) had lidar ratio values between 6 sr and 20 sr.



Figure 5.6: Lidar ratio calculations for measurements during the winter 2010 measurement campaign a) 532 nm b) 355 nm

Some of the references in the previous paragraph stated that there are multiple scattering corrections implemented in the measurements. *Chen et al.* (2002) reported their calculated
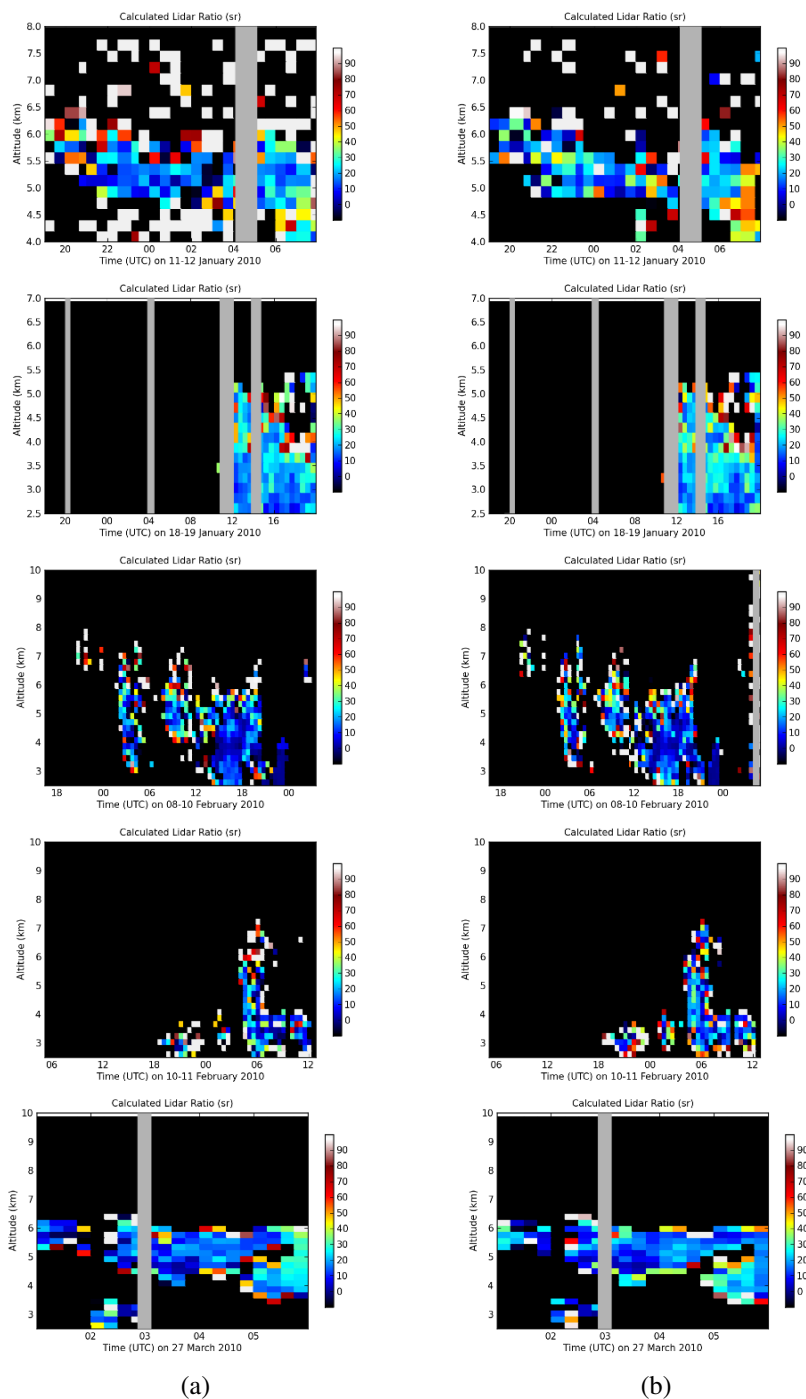
lidar ratios were originally between 28 sr and 33 sr and that clouds with optical depths of 1 or higher needed multiple scattering correction. Also, *Giannakaki et al.* (2007) stated that for the 355 nm wavelength, the lidar ratio for cirrus cloud particle in their case was approximately 26 sr before a correction for multiple scattering was applied but in this reference, optical depths as low as 0.2 had the correction applied. For most ice cloud measurements from the CRL, the optical depths were between 0.5 and 1. The uncorrected value in these references match with the CRL's higher ranged calculations of the lidar ratio.

The different lidar ratio values in some of the references could also be caused by the ice clouds being in different geographical locations. A measurement of a single ice cloud in the Arctic by *Lampert et al.* (2009) measured an ice cloud with an average lidar ratio of 21 sr using an airborne lidar system. A comparison of ice cloud particle size and location shown by *Boudala et al.* (2002) indicated that at the same temperatures, mid latitude cirrus cloud ice particles are larger than higher latitude ice particles. The change in size could have an effect on the calculated lidar ratio in each geographical region. According to Figure 5.3, larger ice particles have a slight increase in the lidar ratio to values over 30 sr compared to smaller particles which are approximately 20 sr.

During the winter 2010 measurement campaign the number of aerosol intrusions were small in the troposphere. This limited the number of possible measurements used for lidar ratio calculations. The aerosol that did intrude over Eureka was only small filaments that had backscatter that was too low to have $\alpha_{aer}(z, \lambda_0)$ calculated using the Raman inversion. Therefore there were no aerosol measurements to use for the lidar ratio calculation.

## 5.5   Colour Ratio Results

There were several measurements during the campaign that could be used for colour ratio calculations of ice clouds and a few could be used for aerosol colour ratio calculations. In the colour ratio calculations shown, there is a cut off altitude of 1 km because of differential overlap. A correction for the differential overlap is being developed, but is not ready to be applied to measurements.

Figure 5.7 shows a series of plots that show $\beta_{aer}(z, \lambda_0)$ for 532 nm, 355 nm, 8.6 mm, and the colour ratio for 532-355 nm and 8.6 mm-532 nm for the same measurement in Figure 5.4. In Figure 5.7, the 532-355 nm wavelength colour ratio shows no significant change from the value of 1 for the ice cloud beginning at 13:00 UTC. Figure 5.8a shows similar
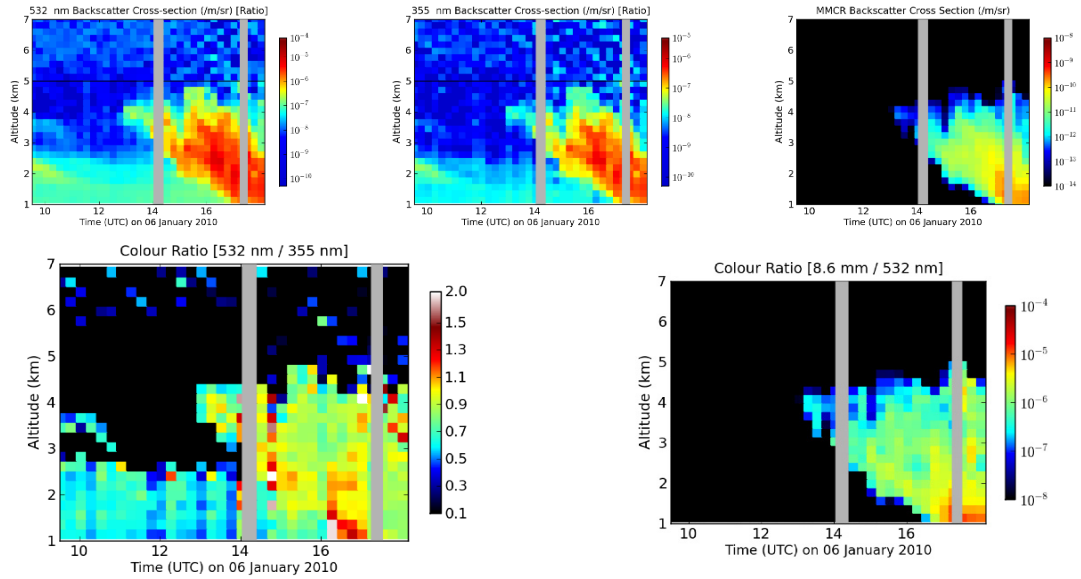
Figure 5.7: $\beta_{aer}(z, \lambda_0)$ calculation for a) 532 nm b) 355 nm c) 8.6 mm and colour ratio calculations for 532-355 nm and 8.6 mm-532 nm for January 06, 2010.

results for the summed profile from 16:30 UTC to 18:10 UTC on January 06, 2010. The summed profile for the cloud has a colour ratio that is approximately 1 throughout the cloud except near the top where there is a decrease of the colour ratio to approximately 0.5. This is likely due to aerosols above the cloud from the Sarychev eruption since the tropopause was extremely low in altitude according to radiosondes during that measurement. The second colour ratio in Figure 5.7 is using the second set of wavelengths, 8.6 mm-532 nm. This colour ratio shows an increase with decreasing altitude for the ice cloud and it has values that are much smaller than the 532-355 nm colour ratio, in the range of $10^{-7}$ to $10^{-4}$.

Figure 5.8b shows the summed profile from 09:30 UTC to 13:00 UTC on January 06, 2010. At this time there is only aerosol in the measurement between 1 km and 3 km. The colour ratio is approximately 0.6 at this time which matches with the values seen on the time-series measurement in Figure 5.7 for the same times. This shows that the 532 nm-355 nm colour ratio can distinguish between aerosols and ice cloud particles. The 8.6 mm-532 nm colour ratio however does not detect anything for the aerosol because the MMCR can not detect particles that small.

The cloud colour ratios reasonably follow the Mie scattering solution but as discussed in Section 5.3 there is not a way to determine the actual size of the particles for the 532 nm-355 nm colour ratio. The 8.6 mm-532 nm colour ratio retrieves particle sizes similar
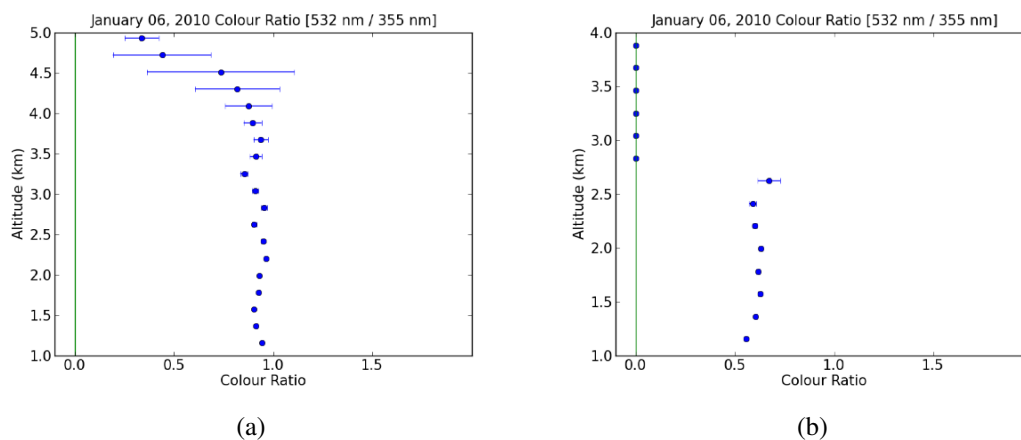
Figure 5.8: Colour ratio calculation for profile measured between a) 16:30 UTC and 18:10 UTC and b) 09:30 UTC and 13:00 UTC on January 06, 2010 using 532 nm-355 nm

to values from *Bourdages et al.* (2009) in the range of 10 microns to 100 microns. This colour ratio also shows that the particle size increases with decreasing altitude. The aerosol colour ratio calculated at the beginning of the measurement of approximately 0.6 falls in the smaller size range in Figure 5.2 indicating particles between 0.05 and 0.5 microns in radius.

## 5.5.1   *Cloud Measurements*

Figure 5.9 shows other measurements from the winter 2010 campaign that also have colour ratio calculations for the 532-355 nm wavelengths. They show relatively similar results as discussed above except for a few measurements. On January 18, 2010, February 08, 2010, February 10, 2010, and March 26, 2010 the 532-355 nm colour ratio calculated showed a significant increase in the colour ratio throughout parts of certain ice clouds. This would indicate that there is a change in particle size throughout the clouds in these measurements. Figure 5.10 shows colour ratio measurements using 8.6 mm-532 nm for the same measurements in Figure 5.9. The colour ratios all increase as you go to the bottom of the cloud, as did the measurement from January 06, 2010.
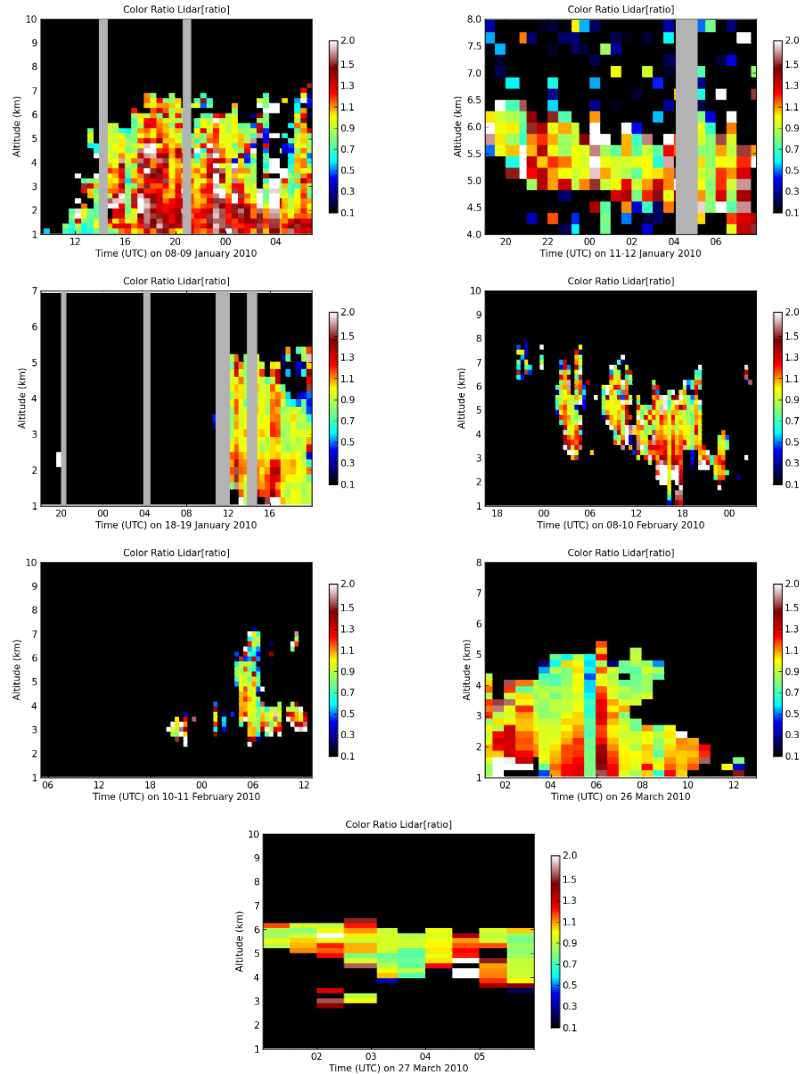
Figure 5.9: Colour Ratio Calculations for Ice Clouds During the Winter 2010 Measurement Campaign using 532 nm and 355 nm $\beta_{\mathrm{aer}}(z, \lambda_0)$ calculated from CRL measurements using the ratio inversion.

Other instruments that calculate colour ratio using lidars calculate similar values for the colour ratio using the 532-355 nm ratio. Most other systems only have cirrus cloud colour ratios using 1064-532 nm (*Liu et al.*, 2002 and *Tao et al.*, 2008) at mid latitudes. The wavelengths will likely produce similar colour ratios due to the proximity of each wavelength in the colour ratio and the proximity of the wavelength sets, 1064-532 nm and 532-355 nm. CALIOP measurements retrieve colour ratios between between 0.8 and 1.2 using the 532 nm and 1064 nm wavelengths (*Liu et al.*, 2002). Calculations from another ground based lidar show similar colour ratios for cirrus clouds as well. The lidar uses the

same set of wavelengths as CALIOP getting results between 0.8 and 1.0 for cirrus cloud measurements (*Tao et al.*, 2008).
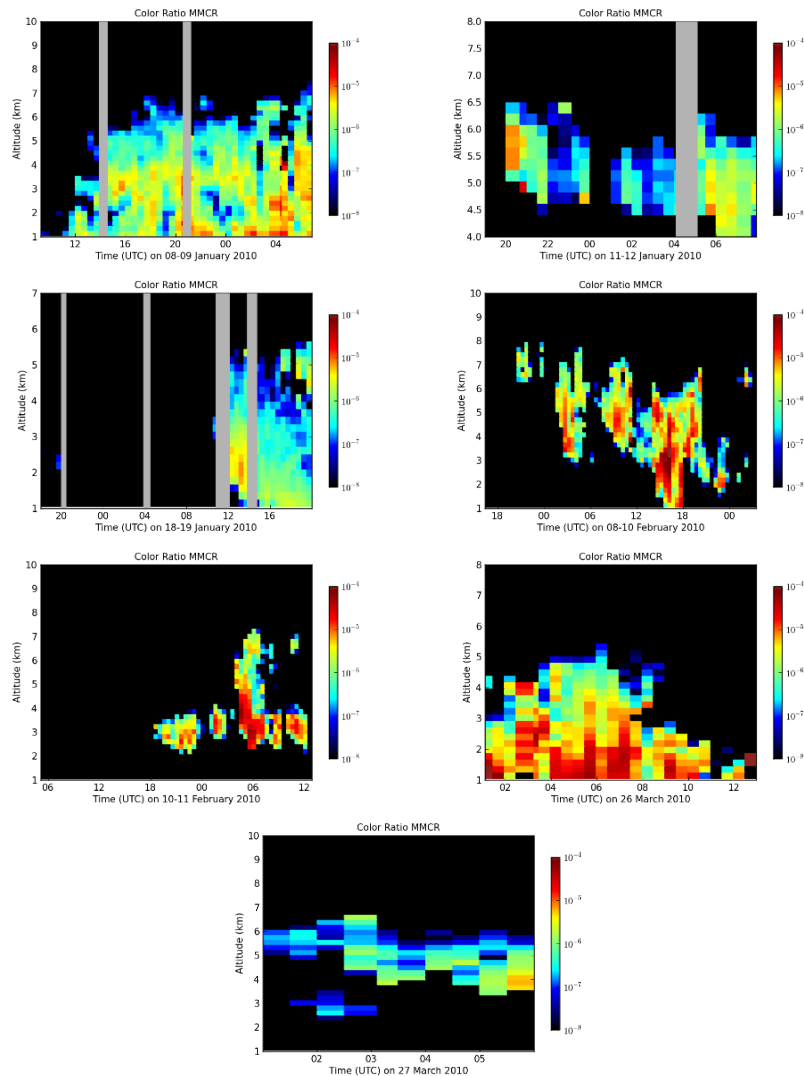


Figure 5.10: Colour Ratio Calculations for Ice Clouds During the Winter 2010 Measurement Campaign 532 nm and 8.6 mm $\beta_{\mathrm{aer}}(z, \lambda_0)$ calculated from CRL and MMCR measurements.

The CRL colour ratio does calculate values above 1.2 unlike the other referenced instruments indicating there could still be a small difference between the colour ratios produced from the 1064-532 nm and 532-355 nm ratios. The colour ratios with higher values are usually in regions near the edges of clouds which have a lower signal to noise ratio giving greater uncertainty to those values. The profile colour ratio measurements usually show a lower maximum colour ratio than the time-series measurements which is likely due to this

reason.

Mie scattering simulations show similar results as in the measurement from January 06, 2010. The 532 nm-355 nm colour ratio is difficult to compare to the simulations due to the small variation in colour ratio for each measurement. The measurements that showed an increase in colour ratio near the bottom of the cloud was compared to the 8.6 mm-532 nm sizes but did not reasonably match. The reason for this is mostly likely due to the assumption of spherical particles in the Mie simulation. Due to the 532 nm-355 nm colour ratio calculation varying by small amounts, the affect of using spherical particles likely has a larger effect on the simulation as compared to the 8.6 mm-532 nm Mie simulation, which varies by orders of magnitude.

### 5.5.2   Aerosol Measurements

The aerosol colour ratio had the same issue as the aerosol lidar ratio calculations making it difficult to retrieve aerosol colour ratio calculations in the troposphere. However calculations were possible for measurements of the Sarychev eruption aerosol in the lower stratosphere as shown in Figure 5.11 and two measurements in the troposphere from January 06, 2010 as shown in Figure 5.4/5.5 and March 04, 2010 in Figure 5.12.

Figure 5.11 has summed profile measurements of colour ratio beginning in December of 2009 up until the end of March 2010. There were measurements of the Sarychev eruption before December but the ratio inversion was not possible due to the measurements only occurring during daylight hours in Eureka. This would leave the Klett inversion as the technique used to calculate $\beta_{aer}(z, \lambda_0)$ but due to issues with the determination of the aerosol lidar ratio for the volcanic aerosol, this technique was not used. Time-series measurements of the aerosol colour ratio were not possible due to the small amount of aerosol backscatter and the aerosol being at high latitudes where there was a low signal to noise ratio.

The Sarychev aerosol colour ratio was constant at a value of approximately 0.35 throughout the campaign. This is a significant drop from the values calculated for cirrus cloud particles as seen in the measurement from January 06, 2010. There is still a difference between those two aerosol measurements as well indicating a difference in size. Aerosol colour ratio measurements from other instruments such as LITE for the same wavelength pair as the CRL calculate values of approximately 0.56 (*Vaughan et al.*, 2007), but the type

of aerosol was not described in the reference. Aerosol measurements for CALIPSO calculate colour ratios at 1064 nm-532 nm which are in the range of 0.4 - 0.5 (*Liu et al.*, 2002). The aerosol colour ratio calculations from the Sarychev eruption and the January 06, 2010 measurement fall within the small size range according to the Mie scattering simulations.
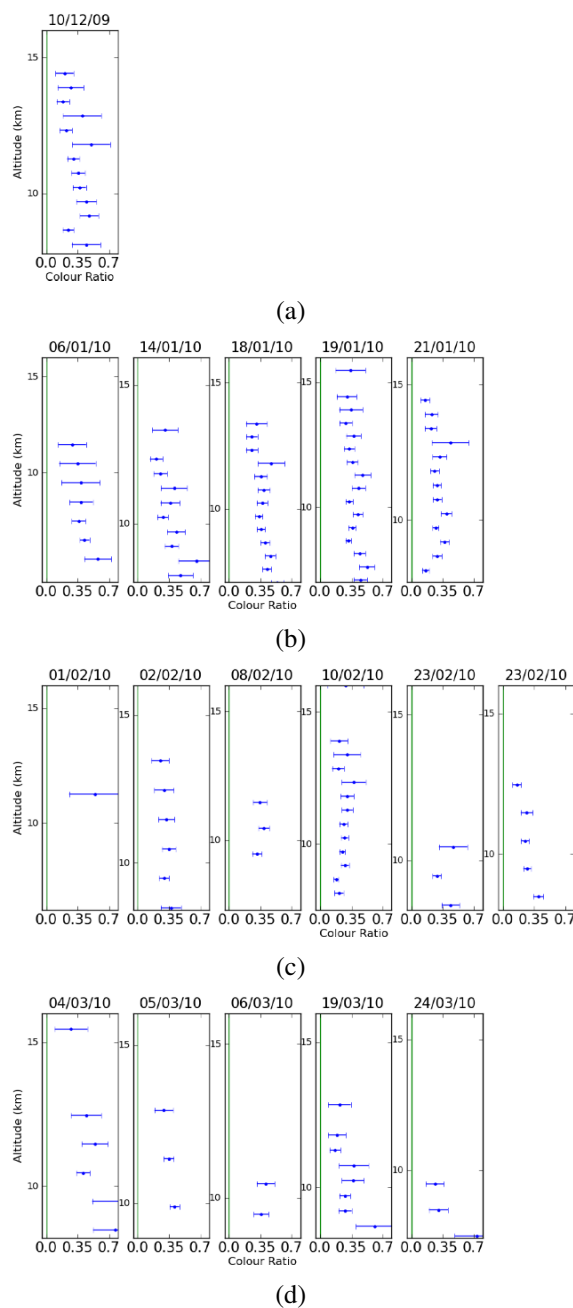


Figure 5.11: Sarychev Colour Ratio Calculations for the Months of a) December 2009, b) January 2010, c) February 2010, and d) March 2010 from CRL winter 2010 Measurement Campaign. The altitude range varies for each measurement by ranging from the tropopause to 16 km.

A single measurement from March 04, 2010 has an aerosol layer between 7 km and 9 km in the troposphere from 06:00 to 14:00 UTC. Figure 5.12 shows a time series and profile of colour ratio for the measurement, which shows a value of approximately 1.0 for the aerosol layer. For this layer, the colour ratio is significantly higher than the Sarychev aerosol which indicates there could be a difference in size for the particles. According to *Omar and Babakaeva* (2004), colour ratios for 1064 nm-532 nm were around 1 or higher for aerosols considered to be larger as compared to aerosols with colour ratios less than 1. This corresponds with the Mie scattering simulations in Figure 5.2 for aerosols that would be in the larger size range of greater than 1 micron in radius.



(a)                                        (b)
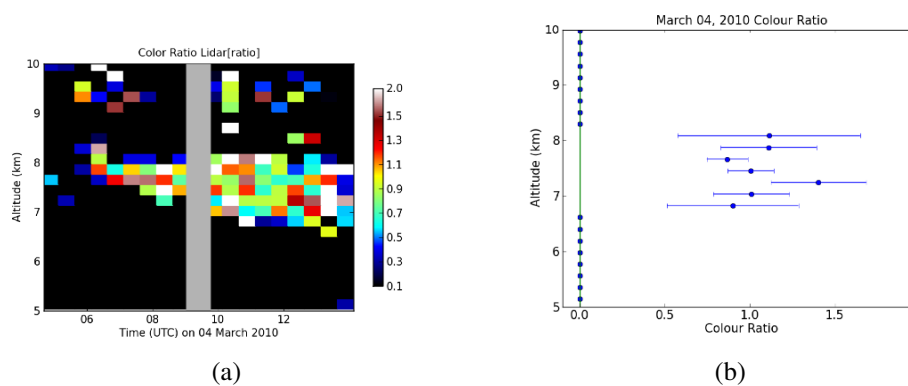
Figure 5.12: Colour Ratio Calculations for an aerosol layer on March 04, 2010 a) contour plot for the entire measurement ranging from 5 km to 10 km. b) profile during the same time and altitude range.

## 5.6 Summary

Lidar and colour ratios were calculated using different measurements from the CRL and MMCR for both ice and aerosol particles. Lidar ratios could only be calculated for ice clouds from the winter 2010 measurements due to the lack of aerosols and low signal to noise ratio in aerosol layers which the Raman inversion could not overcome. For ice clouds, lidar ratios were calculated to be in the range of 10 to 30 sr for both 532 nm and 355 nm where the high end values matches with measurements from other instruments measuring cirrus clouds at mid-latitude locations. The inconsistency between the CRL and other Raman lidars could be due to the clouds being in different environments (Arctic and mid latitude). One case of an ice cloud measurement in the Arctic showed agreement with

the CRL measurements where it retrieved a value of 21 sr for the lidar ratio.

Colour ratios were calculated for two sets of wavelengths, 532 nm-355 nm and 8.6 mm-532 nm. For the first set of wavelengths they were in the range of 0.8 to 1.5 while for the second set they covered values between $10^{-7}$ to $10^{-5}$. Some measurements showed colour ratio calculations from the CRL measurements (532-355 nm) matching features with the MMCR (8.6 mm-532 nm) colour ratio. Colour ratios were also calculated for the 532 nm-355 nm wavelengths for aerosols which showed a range of values between 0.35 and 1. The colour ratios from the CRL for ice and aerosol match with results from other ground based and satellite based instruments which had similar wavelengths.

A Mie scattering model was used to calculate conversions for CRL colour ratios (532 nm-355 nm) to effective radii. The results were inconclusive for ice particles due to the small variations in the colour ratio with changes in radius. For aerosols it was determined that the colour ratio could at least distinguish between fine and course mode aerosol which was shown in the Sarychev volcanic measurements and the aerosol measurement from March 04, 2010.

# CHAPTER 6

# CONCLUSION

Two new techniques, the Coffin and Ratio inversions, were evaluated for the calculation of $\alpha_{aer}(z, \lambda_0)$ and $\beta_{aer}(z, \lambda_0)$ and compared to results of the Klett inversion. The Coffin and the Ratio inversion in most cases were similar but the Ratio inversion was the simpler and easier to use technique. The Coffin inversion could account for more specific changes in the measured profile but it was difficult to properly set up for each measurement due to changes in particle properties during a measurement. The Klett inversion was still superior for higher altitude measurements due to it only using one signal, instead of having the combined noise of two signals in the other techniques. There still has to be work done with respect to a differential overlap and overlap corrections so measurements can be retrieved at the lowest possible altitudes for all aerosol measurement techniques.

Two alignment techniques were also introduced, the Gaussian and polynomial techniques. The Gaussian technique is best used in situations where there are significant changes the lidar, such as changes in the aperture stop and focus stage. If there were no significant changes to the system during a measurement campaign it is best to use the polynomial technique, which is much faster than the Gaussian technique. Each technique did have issues aligning an axis for the visible steering mirror due to the anti-symmetric curve created in the alignment procedure. More work needs to be done before this can be fully automated.

The CRL accomplished its first measurement campaign with no significant problems. The campaign had over 900 hours of data collection from January 2010 to April 2010. During the campaign there were several measurements which showed distinct air mass layering throughout the troposphere, which was seen in aerosol and water vapour measurements. Back trajectories showed that each air mass originated from various mid latitudinal

locations acquiring water vapour and aerosol before arriving in Eureka. This also showed that large amounts of water vapour in the Arctic originates from mid-latitudes.

Another interesting set of measurements from the winter 2010 measurement campaign was due to the Sarychev Volcanic eruption in June of 2009. Lidar measurements from the AHSRL and CRL tracked the stratospheric aerosol since it arrived in Eureka in July of 2009 until March of 2010 which is when $\beta_{aer}(z, \lambda_0)$ was at background conditions. Integrated $\beta_{aer}(z, \lambda_0)$ measurements using both lidar and sun photometer data were used to track the change in the aerosol concentration over time. $\beta_{aer}(z, \lambda_0)$ measurements were also used to track the descent of the plume altitude after it arrived in Eureka up until March of 2010. OMI measurements proved that the aerosol and $SO_2$ measured on July 01, 2009 were from the Kuril Islands which is where the eruption occurred.

Measurements of both the colour ratio and lidar ratio were completed for most measurements where optically thin clouds were measured by the CRL. The lidar ratio was successfully measured in six measurements retrieving values between 10 and 30 sr in most cases. The lidar ratio was calculated using the 532 nm and 355 nm wavelengths and did not show a significant difference between the values calculated for each wavelength. This value reasonably matches with measurements done by other lidar systems (*Giannakaki et al.*, 2007 and *Reichardt*, 1998 and *Chen et al.*, 2002). The colour ratio for clouds was measured for several measurements during the campaign using the ratio of 532-355 nm and 8.6 mm-532 nm from the CRL and MMCR measurements. A colour ratio of approximately 0.8 -1.5 was calculated for clouds using the 532-355 nm ratio which matches well with other lidar measurements (*Tao et al.*, 2008 and *Liu et al.*, 2002).

Lidar ratio measurements of aerosols were not possible with the low number of aerosol measurements during the campaign and the low signal to noise ratio in the aerosol measurements that were measured. Colour ratio calculations were possible for the measurements of the stratospheric aerosols due to the Sarychev eruption. Values of approximately 0.35 were retrieved for most of the campaign which compared well with other aerosol colour ratio measurements (*Vaughan et al.*, 2007 and *Liu et al.*, 2002). A Mie scattering model was used to convert the colour ratio calculations to effective radii by use of a Mie scattering model. Colour ratio calculations could be converted to separate course mode and fine mode aerosols, but ice clouds colour ratios could not be converted to a size from the CRL wavelengths due to oscillating changes of the colour ratio with change in effective radius.

# BIBLIOGRAPHY

Albrecht, B., Aerosols, Cloud Microphysics, and Fractional Cloudiness, *Science*, *245*, 1227–1230, 1989.

Ansmann, A., and D. Muller, Lidar and atmospheric aerosol particles, in *Lidar: Range Resolved Optical Remote Sensing of the Atmosphere*, vol. 1 of *Opt. Sci.*, pp. 105–141, 2005.

Ansmann, A., et al., Measurement of atmospheric aerosol extinction profiles with a Raman lidar, *Opt. Lett.*, *15*, 746–748, 1990.

Ansmann, A., et al., Combined Raman Elastic-backscatter LIDAR for Vertical Profiling of Moisture, Aerosol Extinction, Backscatter, and LIDAR Ratio, *Appl. Phys. B*, *55*, 18–28, 1992.

Avey, L., et al., Evaluation of the aerosol indirect effect using satellite, tracer transport model, and aircraft data from the International Consortium for Atmospheric Research on Transport and Transformation, *J. Geophys. Res.*, *112*, 1–10, 2008.

Bitar, L., et al., Lidar observations of Kasatochi volcano aerosols in the troposphere and stratosphere, *J. Geophys. Res.*, *115*, 1–10, 2010.

Bluth, G., et al., Stratospheric Loading of Sulfur from Explosive Volcanic Eruptions, *J. Geol.*, *105*, 671–683, 1997.

Bohren, and Huffman, *Absorption and Scattering of Light by Small Particles*, John Wiley and Sons, New York, 1983.

Boudala, F. S., et al., A GCM Parameterization of Ice Particle Mean Effective Sizes for High Latitude Cirrus Clouds and Its Comparison with Mid-Latitude Parameterization, *Twelfth ARM Science Team Meeting Proceedings*, 2002.

Bourdages, L., et al., Physical properties of High Arctic tropospheric particles during winter, *Atmos. Chem. Phys.*, *9*, 6881–6897, 2009.

Cattrall, C., et al., Variability of aerosol and spectral lidar and backscatter and extinction ratios of key aerosol types derived from selected Aerosol robotic network locations, *J. Geophys. Res.*, *110*, 1–13, 2005.

Chen, W., et al., Lidar ratio and depolarization ratio for cirrus clouds, *Appl. Opt.*, *41*, 6470–6476, 2002.

Coffey, M., Observations of the impact of volcanic activity on stratospheric chemistry, *J. Geophys. Res.*, *101*, 6767–6780, 1996.

Coffin, M., Lidar Inversion Algorithms for Terrestrial and Martian Atmospheres, Master's thesis, Dalhousie University, 2006.

Collis, R., Lidar, *Appl. Opt.*, *9*, 1782–1788, 1970.

Comiso, J., et al., Accelerated decline in the Arctic sea ice cover, *Geophys. Res. Lett.*, *35*, 1–6, 2008.

Curry, J., et al., Overview of arctic cloud and radiation characteristics, *J. Clim.*, *9*, 1731–1764, 1996.

Draxler, R., and G. Hess, Description of HYSPLIT 4 modeling system, *Air Resources Laboratory Report*, 2004.

Dreshler, T., A review of global stratospheric aerosol: Measurements, importance, life cycle, and local stratospheric aerosol, *Atmos. Res.*, *90*, 223–232, 2008.

Duck, T., and J. Whiteway, The spectrum of waves and turbulence at the tropopause, *Geophys. Res. Lett.*, *32*, 1–4, 2005.

Eloranta, E. E., High spectral resolution lidar, in *Lidar: Range Resolved Optical Remote Sensing of the Atmosphere*, vol. 1 of *Opt. Sci.*, pp. 143–163, 2005.

Franke, K., et al., One−year observations of particle lidar ratio over the tropical Indian Ocean with Raman lidar, *Geophys. Res. Lett.*, *28*, 4559–4562, 2001.

Giannakaki, E., et al., Optical and geometrical characteristics of cirrus clouds over a mid-latitude lidar station, *Atmos. Chem. and Phys.*, *7*, 9284–9317, 2007.

Grenci, L., and J. Nese, *A world of weather: fundamentals of meteorology*, Kendall and Hunt Publishing Company, USA, 2001.

Holton, J., et al., Stratosphere-Troposphere Exchange, *Rev. Geophys.*, *33*, 403–439, 1995.

IPCC, Climate Change 2007: The Physical Science Basis, *Intergovernmental Panel on Climate Change (IPCC)*, 2007.

Johannessen, O., et al., Arctic climate change: observed and modelled temperature and sea-ice variability, *Tellus*, *56*, 328–341, 2004.

Klett, J. D., Stable analytical inversion solution for processing lidar returns, *Appl. Opt.*, *20*, 211–220, 1981.

Kovalev, V. A., and W. E. Eichinger, *Elastic Lidar Theory, Practise and Analysis Methods*, John Wiley & Sons, Inc., New Jersey, 2004.

Lampert, A., et al., Airborne Observations of a Subvisible Midlevel Arctic Ice Cloud: Microphysical and Radiative Characterization, *Atmos. Chem. Phys.*, *9*, 595–634, 2009.

Levin, B., et al., Russian Land Expanded after Recent Events in Sakhalin Oblast, *Herald of the Russian Academy of Sciences*, *90*, 42–46, 2010.

Liou, K. N., *An Introduction to Atmospheric Radiation*, University of California, USA, 2002.

Liu, Z., et al., Scene Classification for the CALIPSO Lidar, in *21st International Laser Radar Conference*, 2002.

Liu, Z., et al., CALIPSO lidar observations of the optical properties of Saharan dust: A case study of long-range transport, *J. Geophys. Res.*, *113*, 1–20, 2007.

Mattis, I., et al., Volcanic aerosol layers observed with multiwavelength Raman lidar over central Europe in 20082009, *J. Geophys. Res.*, *115*, 1–9, 2010.

McGill, M. J., Lidar - Remote Sensing, in *Encyclopedia of Optical Engineering*, vol. 2, pp. 1103–1113, Marcel Decker Inc., 2003.

Mishchenko, M., et al., *Scattering, Absorption, and Emission of Light by Small Particles*, Cambridge University Press, USA, 2002.

Nott, G., et al., A remotely-operated lidar for aerosol, temperature, and water vapor proling in the High Arctic, *J. Atmos. Ocean Tech.*, 2010.

Omar, A., and T. Babakaeva, Aerosol Optical Properties Derived from Lidar Observations Using Cluster Analysis, in *Geoscience and Remote Sensing Symposium*, 2004.

O'Neill, N., et al., The lognormal distribution as a reference for reporting aerosol optical depth statistics; Empirical tests using multi-year, multi-site AERONET sunphotometer data, *Geophys. Res. Lett.*, *27*, 3333–3336, 2000.

Pappalardo, G., et al., Aerosol lidar intercomparison in the framework of the EARLINET project. 3. Raman lidar algorithm for aerosol extinction, backscatter, and lidar ratio, *Appl. Opt.*, *43*, 5370–5385, 2004.

Petty, D., et al., Cirrus Extinction and Lidar Ratio Derived from Raman Lidar Measurements at the Atmospheric Radiation Measurement Program Southern Site, in *ARM Science Team Meeting Proceedings*, 2006.

Reichardt, J., Optical and Geometrical Properties of Northern Midlatitude Cirrus Clouds Observed with a UV Raman Lidar, *Phys. Chem. Earth*, *24*, 255–260, 1998.

Sakai, T., et al., Case study of Raman lidar measurements of Asian dust events in 2000 and 2001 at Nagoya and Tsukuba, Japan, *Atmos. Env.*, *36*, 5479–5489, 2001.

Sasano, Y., et al., Geometric form factor in the laser radar equation: an experimental determination, *Appl. Opt.*, *18*, 3908–3910, 1979.

Sasano, Y., et al., Error caused by using a constant extinction/backscattering ratio in the lidar solution, *Appl. Opt.*, *24*, 3929–3932, 1985.

Serreze, M., and R. Barry, *The Arctic climate system*, Cambridge University Press, UK, 2005.

Stohl, A., et al., Technical note: The Lagrangian particle dispersion model FLEXPART version 6.2, *Atmos. Chem. and Phys.*, *5*, 4739–4799, 2005.

Tao, Z., et al., Measurement of cirrus cloud backscatter color ratio with a two-wavelength lidar, *Appl. Opt.*, *47*, 1478–1485, 2008.

Twomey, S., The influence of pollution on the short wave albedo of clouds, *J, Atmos. Sci.*, *34*, 1149–1152, 1977.

Vaughan, M., et al., Multi-Wavelength Analysis of a Lofted Aerosol Layer Measured By LITE, in *22nd International Laser Radar Conference*, 2007.

Wandinger, U., Raman lidar, in *Lidar: Range Resolved Optical Remote Sensing of the Atmosphere*, vol. 1 of *Opt. Sci.*, pp. 241–271, 2005a.

Wandinger, U., Introduction to lidar, in *Lidar: Range Resolved Optical Remote Sensing of the Atmosphere*, vol. 1 of *Opt. Sci.*, pp. 1–18, 2005b.

Wandinger, U., and A. Ansmann, Experimental determination of the lidar overlap profile with Raman lidar, *Appl. Opt.*, *41*, 511–514, 2002.

Whiteman, D. N., Examination of the traditional Raman lidar technique. ii. Evaluating the ratios for water vapor and aerosols, *Appl. Opt.*, *42*, 2593–2608, 2003.